Jordan Journal of Mechanical and Industrial Engineering (JJMIE)

JJMIE is a high-quality scientific journal devoted to fields of Mechanical and Industrial Engineering. It is published by Hashemite University in corporation with the Jordanian Scientific Research Support Fund.

SUBMISSION ADDRESS:

Prof. Ahmed Al-Ghandoor, Editor-in-Chief
Jordan Journal of Mechanical & Industrial Engineering,
Hashemite University,
PO Box 330127, Zarqa, 13133 , Jordan
E-mail: jjmie@hu.edu.jo

Hashemite Kingdom of Jordan

Hashemite University

Jordan Journal of Mechanical and Industrial Engineering

JJMIE

An International Peer-Reviewed Scientific Journal

Financed by Scientific Research Support Fund

http://jjmie.hu.edu.jo/

ISSN 1995-6665

Jordan Journal of Mechanical and Industrial Engineering (JJMIE)

JJMIE is a high-quality scientific journal devoted to fields of Mechanical and Industrial Engineering. It is published by The Jordanian Ministry of Higher Education and Scientific Research in corporation with Hashemite University.

Introduction: The Editorial Board is very committed to build the Journal as one of the leading international journals in mechanical and industrial engineering sciences in the next few years. With the support of the Ministry of Higher Education and Scientific Research and Jordanian Universities, it is expected that a heavy resource to be channeled into the Journal to establish its international reputation. The Journal's reputation will be enhanced from arrangements with several organizers of international conferences in publishing selected best papers of the conference proceedings.

Aims and Scope: *Jordan Journal of Mechanical and Industrial Engineering* (JJMIE) is a refereed international journal to be of interest and use to all those concerned with research in various fields of, or closely related to, mechanical and industrial engineering disciplines. *Jordan Journal of Mechanical and Industrial Engineering* aims to provide a highly readable and valuable addition to the literature which will serve as an indispensable reference tool for years to come. The coverage of the journal includes all new theoretical and experimental findings in the fields of mechanical and industrial engineering or any closely related fields (Materials, Manufacturing, Management, Design, Thermal and Fluid, Energy, Control, Mechatronics, and Biomedical). The journal also encourages the submission of critical review articles covering advances in recent research of such fields as well as technical notes.

Guide for Authors

Manuscript Submission:
High-quality submissions to this new journal are welcome now and manuscripts may be either submitted online or email.

Online: For online and email submission upload one copy of the full paper including graphics and all figures at the online submission site, accessed via http://jjmie.hu.edu.jo. The manuscript must be written in MS Word 2010 Format. All correspondence, including notification of the Editor's decision and requests for revision, takes place by e-mail and via the Author's homepage, removing the need for a hard-copy paper trail.

Submission address and contact:
Prof. Ahmed Al-Ghandoor
Editor-in-Chief
Jordan Journal of Mechanical & Industrial Engineering,
Hashemite University,
PO Box 330127, Zarqa, 13115, Jordan
E-mail: jjmie@hu.edu.jo

Types of contributions*:* Original research papers and Technical reports

Corresponding author: Clearly indicate who is responsible for correspondence at all stages of refereeing and publication, including post-publication. Ensure that telephone and fax numbers (with country and area code) are provided in addition to the e-mail address and the complete postal address. Full postal addresses must be given for all co-authors.

Original material: Submission of an article implies that the work described has not been published previously (except in the form of an abstract or as part of a published lecture or academic thesis), that it is not under consideration for publication elsewhere, that its publication is approved by all authors and that, if accepted, it will not be published elsewhere in the same form, in English or in any other language, without the written consent of the Publisher. Authors found to be deliberately contravening the submission guidelines on originality and exclusivity shall not be considered for future publication in this journal.

Withdrawing: If the author chooses to withdraw his article after it has been assessed, he shall reimburse JJMIE with the cost of reviewing the paper.

Manuscript Preparation:

General: Editors reserve the right to adjust style to certain standards of uniformity. Original manuscripts are discarded after publication unless the Publisher is asked to return original material after use. Please use MS Word 2010 for the text of your manuscript.

Structure: Follow this order when typing manuscripts: Title, Authors, Authors title, Affiliations, Abstract, Keywords, Introduction, Main text, Conclusions, Acknowledgements, Appendix, References, Figure Captions, Figures and then Tables. Please supply figures imported into the text AND also separately as original graphics files. Collate acknowledgements in a separate section at the end of the article and do not include them on the title page, as a footnote to the title or otherwise.

Text Layout: Use 1.5 line spacing and wide (3 cm) margins. Ensure that each new paragraph is clearly indicated. Present tables and figure legends on separate pages at the end of the manuscript. If possible, consult a recent issue of the journal to become familiar with layout and conventions. All footnotes (except for table and corresponding author footnotes) should be identified with superscript Arabic numbers. To conserve space, authors are requested to mark the less important parts of the paper (such as records of experimental results) for printing in smaller type. For long papers (more than 4000 words) sections which could be deleted without destroying either the sense or the continuity of the paper should be indicated as a guide for the editor. Nomenclature should conform to that most frequently used in the scientific field concerned. Number all pages consecutively; use 12 or 10 pt font size and standard fonts.

Corresponding author: Clearly indicate who is responsible for correspondence at all stages of refereeing and publication, including post-publication. The corresponding author should be identified with an asterisk and footnote. Ensure that telephone and fax numbers (with country and area code) are provided in addition to the e-mail address and the complete postal address. Full postal addresses must be given for all co-authors. Please consult a recent journal paper for style if possible.

Abstract: A self-contained abstract outlining in a single paragraph the aims, scope and conclusions of the paper must be supplied.

Keywords: Immediately after the abstract, provide a maximum of six keywords (avoid, for example, 'and', 'of'). Be sparing with abbreviations: only abbreviations firmly established in the field may be eligible.

Symbols: All Greek letters and unusual symbols should be identified by name in the margin, the first time they are used.

Units: Follow internationally accepted rules and conventions: use the international system of units (SI). If other quantities are mentioned, give their equivalent in SI.

Maths: Number consecutively any equations that have to be displayed separately from the text (if referred to explicitly in the text).

References: All publications cited in the text should be presented in a list of references following the text of the manuscript.

Text: Indicate references by number(s) in square brackets in line with the text. The actual authors can be referred to, but the reference number(s) must always be given.

List: Number the references (numbers in square brackets) in the list in the order in which they appear in the text.

Examples:
Reference to a journal publication:
[1] M.S. Mohsen, B.A. Akash, "Evaluation of domestic solar water heating system in Jordan using analytic hierarchy process". Energy Conversion & Management, Vol. 38 (1997) No. 9, 1815-1822.

Reference to a book:
[2] Strunk Jr W, White EB. The elements of style. 3rd ed. New York: Macmillan; 1979.

Reference to a conference proceeding:
[3] B. Akash, S. Odeh, S. Nijmeh, "Modeling of solar-assisted double-tube evaporator heat pump system under local climate conditions". 5th Jordanian International Mechanical Engineering Conference, Amman, Jordan, 2004.

Reference to a chapter in an edited book:
[4] Mettam GR, Adams LB. How to prepare an electronic version of your article. In: Jones BS, Smith RZ, editors. Introduction to the electronic age, New York: E-Publishing Inc; 1999, p. 281-304

Free Online Color : If, together with your accepted article, you submit usable color and black/white figures then the journal will ensure that these figures will appear in color on the journal website electronic version.

Tables: Tables should be numbered consecutively and given suitable captions and each table should begin on a new page. No vertical rules should be used. Tables should not unnecessarily duplicate results presented elsewhere in the manuscript (for example, in graphs). Footnotes to tables should be typed below the table and should be referred to by superscript lowercase letters.

Notification: Authors will be notified of the acceptance of their paper by the editor. The Publisher will also send a notification of receipt of the paper in production.

Copyright: All authors must sign the Transfer of Copyright agreement before the article can be published. This transfer agreement enables Jordan Journal of Mechanical and Industrial Engineering to protect the copyrighted material for the authors, but does not relinquish the authors' proprietary rights. The copyright transfer covers the exclusive rights to reproduce and distribute the article, including reprints, photographic reproductions, microfilm or any other reproductions of similar nature and translations.

Proof Reading: One set of page proofs in MS Word 2010 format will be sent by e-mail to the corresponding author, to be checked for typesetting/editing. The corrections should be returned within **48 hours**. No changes in, or additions to, the accepted (and subsequently edited) manuscript will be allowed at this stage. Proofreading is solely the author's responsibility. Any queries should be answered in full. Please correct factual errors only, or errors introduced by typesetting. Please note that once your paper has been proofed we publish the identical paper online as in print.

Author Benefits:

No page charges: Publication in this journal is free of charge.

Free offprints: One journal issues of which the article appears will be supplied free of charge to the corresponding author and additional offprint for each co-author. Corresponding authors will be given the choice to buy extra offprints before printing of the article.

JJMIE

Volume 10 Number 4, December.2016
ISSN 1995-6665

Jordan Journal of Mechanical and Industrial Engineering

JJMIE

Volume 10 Number 4, December.2016
ISSN 1995-6665
Pages 231-237

Jordan Journal of Mechanical and Industrial Engineering

Synthesis and Characterization of Epoxy Matrix Composites Reinforced with Various Ratios of TiC

Malek Ali *

Department of Mechanical Engineering, Faculty of Engineering, University of Tabuk, Saudi Arabia.

Received Jan, 8, 2016 *Accepted July, 21, 2016*

Abstract

Epoxy matrix composites reinforced with various ratios of Titanium Carbide (TiC) have been synthesized and characterized successfully. Different ratio of (TiC) powder (0 wt%, 5 wt%, 10 wt%, 15wt%, 20wt%, and 25 wt%) has been used as reinforcements in epoxy matrix. The results obtained show improvement in both mechanical and tribological behavior of the composites. Hardness value, impact strength, tensile strength and wear rate was improved by the addition suitable titanium carbide powder ratio. Hardness and tensile strength values show increment with addition of 15 wt% of titanium carbide powder. Impact strength was found to be increased with increasing ratio to 20 wt% of titanium carbide. The wear behavior was investigated using a pin-on-disc wear testing machine with different sliding distance, wear rate improved greatly at 10 wt% of titanium carbide powder. Optical microscope images (OM) were taken for micro-pores that present on the specimens and for specimens after wear test with 2000m sliding distance. The mechanical properties such as hardness, tensile strength, impact, and wear resistance are observed to be increased considerably compared to the matrix composite.

Keywords: *Epoxy Matrix, Composites, Various Ratios of Particles, TiC*.

1. Introduction

The usage of epoxy resin has been a significant importance in the engineering field for a long period of time. Many components are made of epoxy based materials and are proven to be outstanding in many aspects such as mechanical properties, thermal conductivity, and electrical properties [1]. Mechanical properties have been a major scope since these aspects play an important role in industrial and material refurbishing in numerous field, such as automotive, aerospace, electronics, and biotechnology applications [2]. Epoxies, generally, have high chemical and corrosion resistance, good mechanical and thermal properties, outstanding adhesion to various substrates, low shrinkage upon cure, good electrical insulating properties, and the ability to be processed under a variety of conditions which make it suitable candidate as matrix materials for advanced composites applications [3] [4]. The curing reaction of the epoxy takes place after the addition of a hardener solution into the epoxy resin. During curing, the molecules form cross links with each another and grow in a three-dimensional network that finally forms a solid epoxy resin. Most reinforcing materials used nowadays, such as natural fiber, glass fiber, carbon fiber, etc., have a lower hardness and a higher wear rate compared to Titanium carbide. Composite reinforced with titanium carbide offer an outstanding properties such as high strength to weight ratio, high torsion stiffness, high hardness, good corrosion and wear resistance. Composite systems consisting of a polymer matrix and particles of titanium carbide have been considered as a novel class of smart materials. Researchers investigated abrasive wear behaviour of SiC and TiC fillers filled epoxy composites. They concluded that filled composite showed excellent abrasion resistance compared to unfilled Composites [5; 6; and 7]. Properties of the composites are determined by many factors such as the ratio, size, and shape of reinforced TiC particles. From the literature review it is observed that the researchers have studied the wear property of various inorganic fillers. Hence, the present study focuses on the effect of the contents ratio of TiC on mechanical and tribological behavior of the composites and to have better understanding of the synthesis and characterization the Epoxy- TiC composites.

2. Experimental

2.1. Raw Materials

The main material involved in the present study is the Epoxy which the matrix. The Epoxy is formed from two different components; the first is the resin and second is the hardener with the following specifications:

1. Density of Resin, and Hardener were 1.22, and 0.96 g/ml, respectively;
2. Viscosity of Resin, and Hardener (measured at 20-23◦C) were 800, and 400 mPa s, respectively;
3. Cure Time of mixture (23°C) 24 hours.

* Corresponding author e-mail: vijaya9966998024@rediffmail.com, bandarishankar@gmail.co.in.

In the present study, the reinforcement material was commercial TiC powder with average particle size 3μm supplied by Inframat® Advanced Materials LLC (USA). Titanium carbide is considered a promising reinforcing material towards the development of matrix composites due to its high hardness, melting point, chemical and thermal stabilities, wear resistance, solvency of other carbides, and good wettability and relative thermal stability with many binder materials [10].

2.2. Fabrication of Mold

Aluminum block (20cm ×10cm ×1.6cm) was used as a base for providing a perfect mold that can be reused several times in molding the specimen into required shapes.

The three main shapes that are required for testing were fabricated using the aluminum block. The dimensions, of specimens for Tensile and Impact test according to American Society for Testing and Materials (ASTM) D638, D6110 [8; 9], as shown in Fig. 1.

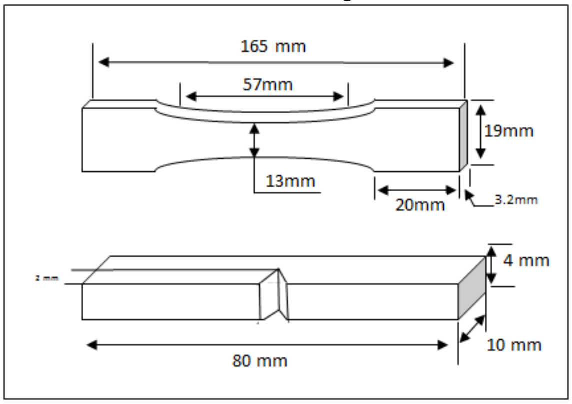

Fig. 1. The dimensions, of specimens for Tensile and Impact test

The dimensions of the specimens prepared for the Wear test were based on the available jig in the pin-on-disc machine. It was more convenient to fabricate rectangular shape specimens for this test. Mold was designed by using CATIA V.55 software. The design is later transferred to develop Computer Numerical Control (CNC) codes which will be used in the milling of aluminum block. The mold after milling and polishing processes is shown in Fig. 2.

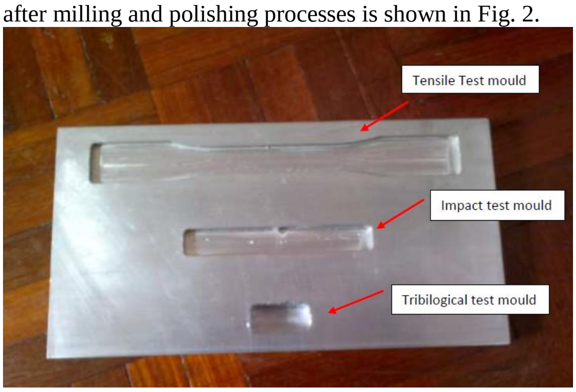

Fig. 2. Mold after milling and polishing processes

Mold was polished with abrasive paper several times until a smooth surface was obtained. The completed mold needs high attention to ensure a smooth release of the composite when it cures in the mold. For the first time five layers of wax were required to ensure that the surface is fully covered. After that only two layers of wax were sufficient to remove composite from the mold easily.

2.3. Preparation and Characterization of Composites

The composite was prepared according to wt% ratio. Pure Epoxy composite and the varying ratio of TiC are provided in Table 1.

Table 1. Epoxy-TiC composites specimens with different wt% ratio of TiC

Set of specimens	TiC content in composite,wt%
1	0wt% of TiC
2	5wt% of TiC
3	10wt% of TiC
4	15wt% of TiC
5	20wt% of TiC
6	25wt% of TiC

The fabrication of composites consists of three steps:

1. Mixing the Epoxy resin and TiC particle using a mechanical stirrer.
2. Mixing the hardener with the filled Epoxy resin.
3. Pouring the mixture into mold.

In the first and second steps, slow motion and steady stirring were applied to ensure that the mixing is done without formation of air bubbles (porosity). A fixed amount of Epoxy resin and hardener were used with a varying amount of TiC powder. In the last step, the mixtures were manually poured into previously prepared mold; the composites were cured at room temperature for 24h. Vickers hardness machine with load of 60kg for 5 seconds was used to investigate the influence of particulate weight fraction of TiC on the matrix hardness. Five different points were taken for each sample and the average value was taken to eliminate errors due to local non-homogeneity. The tensile test was carried out by Universal Testing Machine GUNT WP 300; the specimens were subjected to failure at a constant rate. Pin-on-disk machine shown in Fig. 3 was used to measure the wear resistance of samples. The test was carried out under dry sliding conditions, in ambient air at room temperature ≈ 25 ºC. The disk was rotated by DC motor with sliding rotation speed of 500 rpm and 40N load.

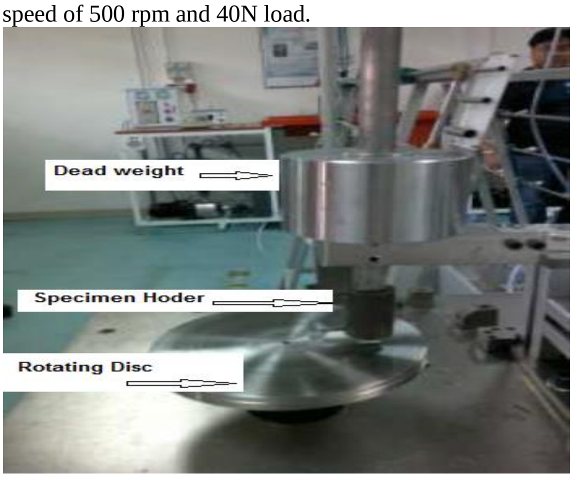

Fig. 3. Pin-On-Disk set-up

The impact test was performed by using Charpy Impact Test Instrument [Testing Machine INC, AMITYVILLE, New York Company] to investigate the influence of particulate weight fraction of TiC on the impact. Optical Microscope (OM) was used for analysis microstructure of different composites compositions.

3. Results and Discussions

3.1. Introduction

The dimensions, of specimens for Tensile and Impact test according to American Society for Testing and Materials (ASTM) D638, D6110 [8; 9]. The dimensions of specimens prepared for Tensile and Impact test were 165± 0.02, 19± 0.01, 3.2± 0.01, and 80± 0.02, 10± 0.01, 4± 0.01 (mm). The three specimens were used to determine the average value of each property.

3.2. Hardness Measurements

The hardness measurement is known to be one of the most informative and rapid methods to determine the mechanical behavior of composites. Yield and ultimate tensile strengths, fatigue strength, wear, etc., are often in good correlation with hardness [11]. A higher hardness was also associated with a lower porosity [12]. Improvement of hardness depends on the amount, particle size, and uniformity distribution of TiC particles (Fig. 6).

Average Hardness Vickers (H.V) for Epoxy with different wt% TiC ratios are shown in Fig. 4.

It is observed from the results of hardness that all reinforced specimens have a higher hardness than that of the matrix material. In general the hardness increased with increasing the hard particles content of TiC. The hardness for specimens with (20 wt% and 25wt% TiC) decreased due to the agglomeration of TiC particles (Fig. 6) and formation of porosity (Fig. 7) during mixing process which lead to big indenting and resulting in a low HV value even though the material has a high hardness value. Furthermore, conditions of a specimen surface also play an important role in determining the hardness value. The surface should be smooth and flat which allows a perfect indenting.

3.3. Tensile Test

Many researchers reported that adding ceramics nanoparticles in an epoxy had a significant effect on the tensile properties of the modified epoxies [13; 14; 15; and16].

In general, increasing the TiC content leads to an increase in the ultimate tensile strength comparing with matrix material. In Fig. 5, the matrix fails with strain value (0.0227); this result shows that the matrix was ductile with the absence of TiC particles, and indicates that the adding of Nano TiC particles support the matrix by absorbing stresses and bear some load before failing.

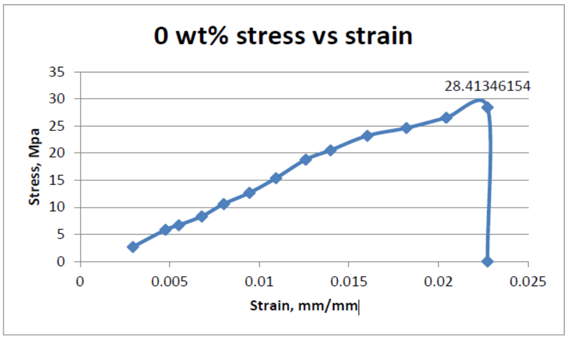

Fig. 5. Stress- strain diagram for 0 wt% of TiC

As shown in Table (2), due to the addition of different percentages of TiC, the tensile strength increased from (28.413 MPa) for the unreinforced matrix to (35.024MPa)) for 15 wt% TiC specimens and the strain failure reduces from (0.0227) for the unreinforced matrix to (0.0156) for 15 wt% TiC specimens. This indicates that the composite properties change from ductile to tough and brittle by good distribution of TiC particles in the resin, as shown in Fig. 6. Also the 25wt% TiC specimen exhibits lowest tensile strength (26.995MPa) comparing with other specimens due to the agglomerated TiC particles in the resin with higher TiC percentages. This indicates that the material became brittle and no plastic deformation was observed during fracture. The ultimate tensile strength, strain failure, and young modulus of elasticity for different specimens are given in Table 2.

Table 2. The relation between TiC powder and tensile strength of the composites

Specimens	Tensile strength MPa	Strain failure	Young modules, GPa
0wt% of TiC	28.413	0.0227	1.25
5wt% of TiC	29.688	0.0108	2.761
10wt% of TiC	31.178	0.0125	2.492
15wt% of TiC	35.024	0.0156	2.241
20wt% of TiC	30.385	0.0125	2.436
25wt% of TiC	26.995	0.0114	2.375

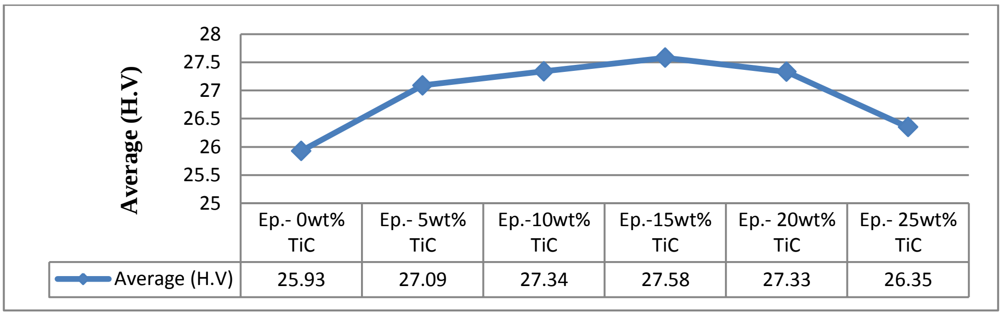

Fig. 4. Average hardness value for epoxy matrix composites reinforced with various ratios of TiC

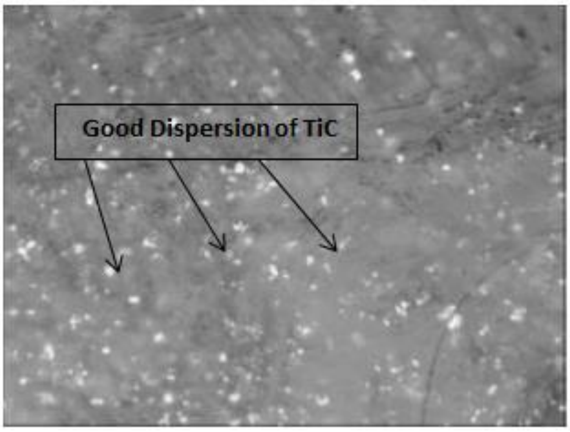

Fig. 6. OM image at 50x showing even dispersion of TiC powder for 15wt%

The shiny particles in Fig. 6 are the TiC powder that is dispersed in the composite uniformly. This proves that the better particles dispersion lead to enhance composite properties. For the 20wt% TiC specimen, a decrease in tensile strength is observed and there is further decreasing in tensile strength for 25wt% TiC specimen. This drop in tensile strength can be explained by the agglomerations and porosity of TiC powder, as shown in Figs. 7 and 8.

The agglomeration of TiC occurs due to high specific surface area which causes an increase in the surface energy of powder and lead to rapid recombination of micro-particulate into agglomerates to compensate unsaturated surface forces via surface reconstruction [17]. The agglomeration leads to creating large pores among agglomerates which lead to decrease in the tensile strength. In general the failure of specimens is caused by cracks around pores that are formed during fabrication and agglomerations. Pores that are trapped in the composite forms empty places in the structure of the composite and help to propagate cracks and allowing the composite to fail at a low stress load. A slight deformation would propagate to crack when even a small load is applied to the composite. The addition of TiC particle increases the brittleness of the epoxy. This is proven by the smooth and flat fracture of the entire composite when it fails. Almost all the fracture was observed to be perpendicular with the direction of the load applied to each composite.

3.4. Effects TiC Ratio on Impact, and Wear

Inorganic particles are frequently employed to improve the mechanical performances of epoxy for engineering applications. Toughness can be improved by the addition of inorganic particles. The resistance to impact (amount of energy absorbed by each specimen before fracture) is one of the key properties of materials. In fact, there is almost a constant rate of increase in material toughness and fracture toughness with the increase of reinforcement material content, as shown in Fig. 9.

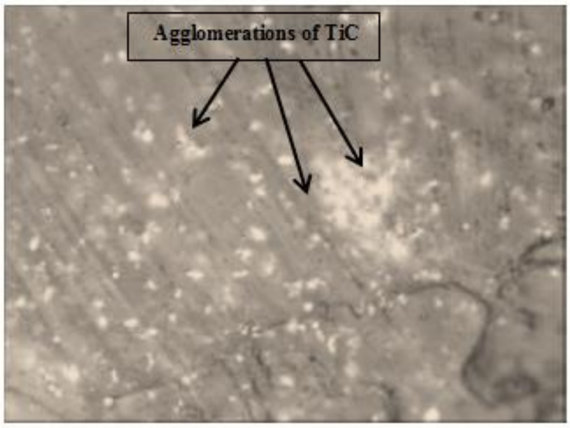

Fig. 7. OM image at 50x of agglomeration of TiC particle in 25wt%

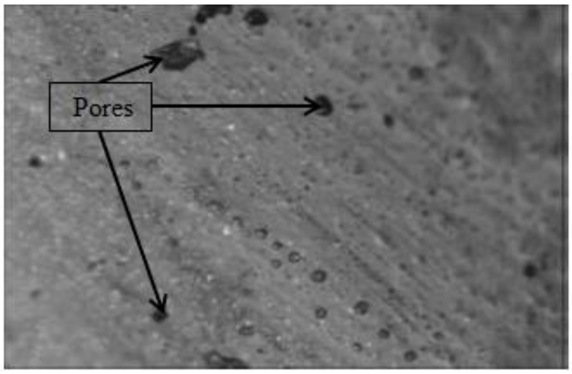

Fig. 8. OM image at 50x of air bubbles in composite

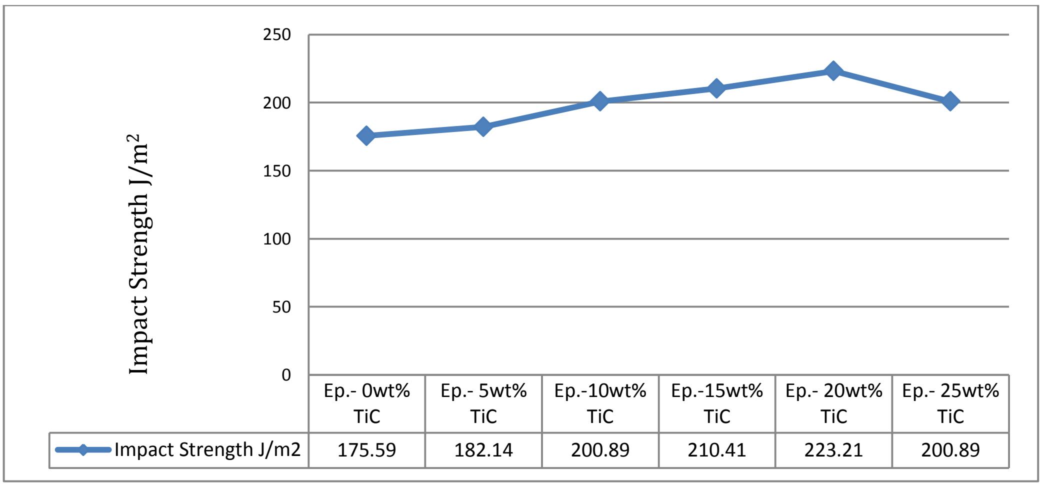

Fig. 9. Average Impact strength value for epoxy matrix composites reinforced with various ratios of TiC

From Fig. 8, it is observed that the impact strength of the pure epoxy composite shows the lowest impact strength at 0.176 kJ/m^2, whereas the 20 wt% has impact strength of 0.223 kJ/m^2. There is a slight increment in the impact strength when the epoxy is reinforced with different ratios of TiC powder. Homogeneously distributed TiC particles are able to improve simultaneously the toughness of the epoxy. Also high specific surface area for TiC particles promotes stress transfer from matrix to TiC particles. With small particle size of TiC, the interparticle distance reduces under a certain filler content. This may activate particle–particle interactions and result in a three-dimensional physical network structure of interphase in a polymer matrix. Good particle–matrix bonding is normally a prerequisite for enhanced fracture toughness [18]. The fracture area of each specimen is flat and smooth regarding wt% of TiC powder. The material behavior that changes after 20 wt% of TiC can be explained by increase of pores which creates a path for crack to propagation. This can be proven by the formation of micro pores that arise during the fabrication of the specimen. Since the composite was mixed manually, formation of micro-pores could not be avoided, even after the use of ultra-sonic vibrator. Furthermore, the decrease in availability of epoxy material to bond all the Titanium Carbide powder is also another reason for the decrease of impact strength after 20 wt%. Addition of hard ceramic TiC particles increases the hardness of the composites and enhances the resistance of the epoxy to the indenter penetration and reduces subsequent removal of material. By increasing TiC to 10wt.% in epoxy matrix the wear rate was lowest, as shown in Fig. 11, and small plough groove, as shown in Fig. 11 (b), compared with pure epoxy and 25wt.% TiC. There are several factors that affect the wear resistance of the composites such as the type of matrix material, the type of reinforcement, additives (graphite), surface roughness, processing technique (powder metallurgy or casting), sliding speed, load, type of friction (dry or lubricated)[19]. As in Table 3, most of these factors are constant to compare between different specimens compositions.

Table 3. Factors that are affect the wear resistance of the composites

Load, P (N)	**40**
Speed, N (rev/m)	500
Test Distance, d (m)	500, 1000, 1500, 2000
Time for each distance, t (seconds)	173, 347, 520, 694
Room temperature, °C	25±2
Contact condition	dry

From Fig. 10, the wear rate for all specimens with different TiC ratios were decreased with increasing sliding distance due to high interfacial adhesion of remaining TiC to synthetic matrix and could be due to filling of the abrasive paper while the rubbing process. Generally, the wear rates begin a gradual decline with the increasing sliding distance until a steady state condition is reached.

During the friction process bigger TiC particles on the friction surface are impressed deeper to the tested surface and are not easily releasable from the surface. On the other hand, smaller TiC particles on the friction surface are easily released from the surface of composite. The larger size of reinforcing particles can offer protection to the matrix during sliding. Once the reinforcing particles fracture or loosen from the matrix, they can be removed easily from the matrix, resulting in a certain amount of material loss. The two surfaces are brought into sliding contact at the beginning; the soft ductile epoxy matrix between TiC particles undergo deformation. The uniform distribution decreases the matrix between TiC particles which lead to decrease the wear and hardness. Generally, some of the wear debris is lost from the system and some entrapped between the contact surfaces. The entrapped debris particles produce further damage on both surfaces; however increasing the amount of hard TiC particles in the debris leads to more damage on both surfaces, as shown in Fig. 11(c). In order to investigate the wear mechanism, the surfaces of the worn composites were examined under OM.

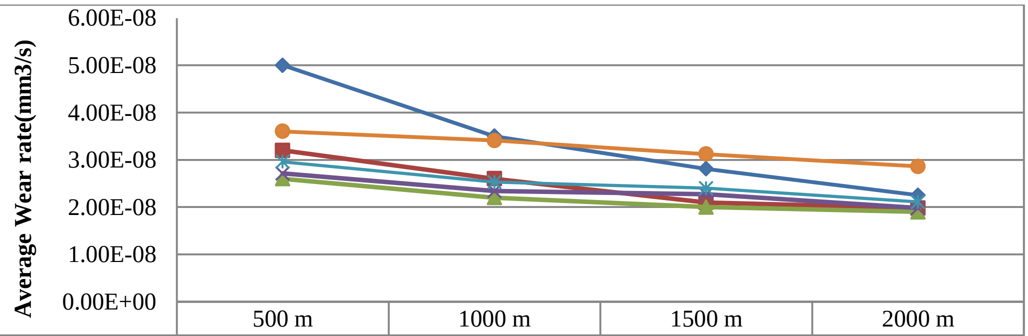

	500 m	1000 m	1500 m	2000 m
0wt% of TiC	5.00E-08	3.50E-08	2.81E-08	2.25E-08
5wt% of TiC	3.20E-08	2.60E-08	2.10E-08	1.98E-08
10wt% of TiC	2.60E-08	2.20E-08	2.00E-08	1.90E-08
15wt% of TiC	2.71E-08	2.34E-08	2.27E-08	1.98E-08
20wt% of TiC	2.96E-08	2.53E-08	2.40E-08	2.11E-08
25wt% of TiC	3.60E-08	3.41E-08	3.12E-08	2.86E-08

Fig. 10. Average wear rate for epoxy matrix composites reinforced with various ratios of TiC particles

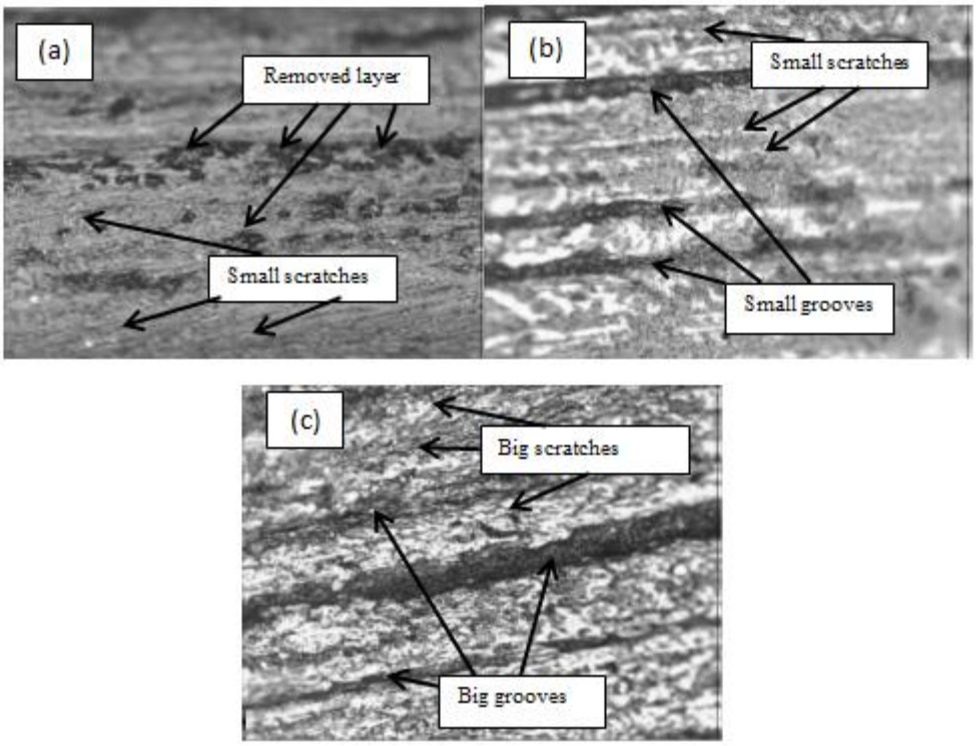

Fig. 11. OM of 0 wt%, 10 wt%, 25 wt% composite at 2000m sliding distance

Fig. 11(a-c) shows typical worn surfaces of the 0 wt.%, 10 wt.% , 25 wt.% TiC composites, respectively. OM for 0 wt. % TiC composite (Fig. 11 (a)) shows a very thin layer removed from some areas with grooves and scratches on the worn surfaces.

OM for 10 wt.% TiC composite (Fig. 11 (b)) shows very small grooves and scratches on the surface, whereas OM for 25 wt.% TiC composite (Fig. 11 (c)) shows many scratches and big grooves on the worn surfaces due to, but with little evidence, particulate fracture, even in composites with the highest weight fraction.

4. Conclusions

Composites reinforced with various ratios of TiC have been synthesized and characterized successfully. The mechanical properties such as hardness, tensile strength, impact, and wear resistance are observed to be increased considerably compared to the matrix composite. Hardness and tensile strength values show increment with addition of 15 wt% of TiC powder whereas hardness and tensile strength values decreased for specimens with (20 wt% and 25wt%) TiC due to agglomeration of TiC particles (Fig. 6) and porosity (Fig. 7) during mixing process. Impact strength had increment with ratio of 20 wt% of TiC. Wear rate improved greatly at 10 wt% TiC. OM for 0 wt.% TiC composite (Fig. 10 (a)) shows a very thin layer removed from some areas with grooves and scratches on the worn surfaces, whereas OM for 25 wt.% TiC composite (Fig. 10 (c)) shows many scratches and big grooves on the worn surfaces.

Acknowledgement

The authors would like to acknowledge the financial support the present work received from the Deanship of Scientific Research (DSR), University of Tabuk, Tabuk, Saudi Arabia, under grant No. S-1437-0033.

References

[1] Z. Yaping, Z. Ying, and N. Rongchang, "Effects of nanoparticles SiO2 on
the performance of nanocomposites". Materials Letters, Vol. 57(2003) 2940-2944.

[2] Z. Yuanxin, P. Farhana, L. Lance, "Fracture and Fatigue behavior of carbon nano fiber reinforced epoxy". Materials Science and Engineering: A, Vol. 452 (2007) 657-664.

[3] L. F. Barcia, P. T. Amaral, and G. B.Soares, "Synthesis and properties of epoxy
resin modified with epoxy-terminated liquid butadiene". *Polymer*, Vol. 44 (2003). 5811.

[4] J. M. L. Reis, F. C. Amorim, A. H. M. F. T. da Silva, H. S. da Costa Mattos, "Influence of temperature on the behavior of DGEBA (bisphenol A diglycidyl ether) epoxy adhesive". International Journal of Adhesion and Adhesives, Vol. 58 (2015) 88–92.

[5] B. Suresha, G. Chandramohan, "Investigations on Three-Body Abrasive Wear Behaviour of Composite Brake Pad Material". Plastic and Polymer Technology (PAPT), Vol. 3 (2014) 10-18.

[6] S. Basavarajappa, S. Manjunath Yadav, k. Santhosh, "abrasive wear behavior of granite-filled glass epoxy composites by SiC particles using statistical analysis". Polymer-plastics technology and engineering, Vol. 50 (2011) 516-534.

[7] C. Anand Chairman, S. P. Kumaresh Babu1, Muthukannan DuraiSelvam, K.R. Balasubramanian, "Investigation on two body abrasive wear behavior of titanium carbide filled glass

fabric epoxy composites- a Box-Behnken approach". International Journal of Engineering, Science and Technology, Vol. 3 (2011) 119-129.

[8] ASTM Standards, "ASTM D 638, Standard Test Method for Tensile Properties of Plastics" ASTM, West Conshohohoken, , PA (2002) 19428-2959.

[9] M.G. Bader, J.E. Bailey, and I. Bell,"The Effect of Fibre-Matrix Interface Strength on the Impact and Fracture Properties of Carbon-Fibre Reinforced Epoxy Resin Composites". Journal of Physics D: Applied Physics, Vol. 6 (1973) 572-586.

[10] A. Farid, S. Guo, X. Yang, Y. Lian, "Stainless steel binder for the development of novel Ticreinforced steel cermets". J of Univ of Sci and Technol Beij, Vol. 13 (2006) 546-550.

[11] B. N. Mordyuk, M. O. Iefimov, G. I. Prokopenko, T. V.Golub, "Structure, microhardness and damping characteristics of Al matrix composite reinforced with AlCuFe or Ti using ultrasonic impact peening". Surface & Coatings Technology, Vol. 204 (2010) 1590–1598.

[12] Y. Sahin, M. Acilar, "Production and properties of SiCp-reinforced aluminium alloycomposites". Composites Part A: Applied Science and Manufacturing, Vol.34 (2003) 709–718.

[13] N. A. Siddiqui, E. L. Li, M.-L. Sham, "Tensile strength of glass fibres with carbon nanotube-epoxy nanocomposite coating: effects of CNT morphology and dispersion state". Composites A, vol. 41 (2010) 539–548.

[14] L. Jingchao, L. Xiaobing, Z. Hualin, Y. Yahui, and F. Wanli, "Study of epoxy Resin Reinf orced and Toughened by nm SiO2". Chinese Journal of Colloid & Polymer, vol. 18 (2000)15–17.

[15] C. Huang, Y. Zhang, S. Fu, and L. Li, "Mechanical properties of epoxy composites filled with SiO2 nano particles at room and cryogenic temperatures". Acta Materiae Compositae Sinica, vol. 21(2004)77–81.

[16] M. Bakar, I. Wojtania, I. Legocka, and J. Gospodarczyk, "Property enhancement of epoxy resins by using a combination of polyamide and montmorillonite". Advances in Polymer Technology, vol. 26 (2007) 223–231.

[17] C. Suryanarayana: New York: Marcel Dekker. (2004). 60-85.

[18] Z. Hui, Z. Zhong, F. Klaus, E. Christian "Property improvements of in situ epoxy nanocomposites with reduced interparticle distance at high nanosilica content". Acta Materialia, vol. 54(2006) 1833–1842.

[19] D. Bialo, "The tribological characteristics of the Al-20Si-3Cu-1mg alloy reinforced with Al2O3 particles in relation to the hardness of a mating steel". J. Materials Science, vol. 35 (2000) 5497 – 5501.

JJMIE

Volume 10 Number 4, December.2016
ISSN 1995-6665
Pages 239-244

Jordan Journal of Mechanical and Industrial Engineering

The Impact of Large Scale Photovoltaic Systems on the Harmonic Increase in Distribution Networks

I. Etier [a,*], M. H. Abderrazzaq [b], A. Al Tarabsheh[a,c], O.A. Saraereh[a], M. AlBdour[d]

[a] Electrical Engineering Dept., Hashemite University, Zarqa, Jordan
[b] Hijjaw Faculty for Engineering Technology, Yarmouk University, Irbid, Jordan
[c] Electrical and Computer Engineering Department, Abu Dhabi University, Abu Dhabi, UAE
[d] Electrical Engineering Dept., German-Jordan University

Received July, 20, 2016 *Accepted September, 20, 2016*

Abstract

The significance of electricity generation by photovoltaic (PV) systems comes from the direct conversion of light into electrical energy. Although such a system is widely used in a small scale, the tendency to apply it in a large scale is gaining ground day after day. However, large generation systems of this type are associated with their own problems arising when they are connected to the national grid. One of these problems is the generation of harmonics from control and power conversion devices included in Photovoltaic system. In the present paper, the mutual impact between large-scale photovoltaic generation systems and electrical grid will be studied in terms of power quality. This requires building a model of large-scale photovoltaic system, connecting it to the grid and testing it under various conditions. Several scenarios will be proposed for the operation of such system taking into consideration the penetration level of solar system, loading levels and load composition of the examined grid. The key elements, exciting harmonic problem, will be identified in the present work and the issues related to such phenomenon will be studied in parallel with other operational patterns dominating in distribution grids. As being relatively intermittent source of energy, photovoltaic will have some means of protection and control which will be considered as parts of this system. The present paper also combines the results obtained from Simulink into LabVIEW which provides a reliable way in analyzing the variation of parameters governing the harmonic behavior. After connecting PV arrays to the grid, the harmonic level increases up to 13.3% in the case of 150 kW PV systems because of the power electronic devices in operation. The effects of the solar radiation and the operating temperature of PV modules on the harmonics are investigated and modeled. The simulations show that the total harmonic distortion is 13.22 %, 13.30%, and 13.40% at T= 30°C, 25°C and 20°C, respectively.

Keywords:*Photovoltaic, generation, solar, harmonics, distribution and grid*.

1. Introduction

The continuous increase in oil prices and the frequent warnings of limited resources and reserves of such fuel have pushed the decision-makers in energy industry to accelerate the use of renewable energy, especially the wind and solar. The intermittent nature of wind makes it unfavorable in many locations, whereas electricity generation by Photovoltaic (PV) is more stable and reliable. Therefore, the installation of PV arrays is not limited to residential load at low voltage, but it extends to include the medium voltage at utility scale. The introduction of this new approach of electricity generation system has its own influence on the performance of distribution networks including the power quality of the supply.

The summation of all harmonic components of the PV voltage or PV current waveform compared to the fundamental component of the voltage or current wave is defined as the Total Harmonic Distortion. The presence of a high value of THD is one of the main indices of power quality poorness. On the other hand, the large scale of PV integration into distribution network needs a robust system of control devices, converting equipment and protective relaying. With the increase of non-linear loads within these systems, the harmonic penetration level will be augmented. Therefore, one of the vital concerns of distribution utilities is to take the required precautions and to conduct the necessary research to be immune from the side effects of PV large scale distribution.

Although the main concern in PV development and application was on the improvement of cells efficiency, several researchers were interested in PV integration with electric grid [1-3]. Another group of workers has tried to use a suitable simulator to study photovoltaic generation systems and connect them with the grid [4], whereas some investigators have attempted to reduce the harmonic impact by applying new topology for PV generation systems integrating current harmonic compensation by using two inverters. The first one was with a feedback loop to compensate the low order harmonics, and the second

* Corresponding author e-mail: etier@hu.edu.jo.

one with a feed forward loop for compensating high order harmonics [5-6].

Despite the importance of the worksabove, the research of harmonic generation associated with large scale PV systems is still in need for more investigation and further study. In the present work much attention is paid to individual harmonics in addition to the THD for existing distribution systems. In comparison with other works, the present paper demonstrated and tested a model of large scale PV system. In addition, several scenarios were proposed for the operation of such system taking into consideration the penetration level of solar system, loading levels and load composition of the examined grid.

2. System Model and Data Collection

The present work was started by building a large scale PV generation model using Simulink to provide a power up to 150 kVA at maximum power point. The next step was to set the parameters of a radial feeder chosen as an example from a real distribution network of Irbid District Electrical Company- Jordan (IDECO). After that, the jointing process has been made using PWM inverter. In this system, the PV model operates as a distributed generation feeding the network with electrical supply. The main components included in this model are:

1. Current network configuration before PV connection and the values of normal harmonic distortion (without PV).
2. The existing loads taking into consideration nonlinear ones.
3. Transmission lines and transformers impedances in addition to generation part
4. Boost chopper followed by controlled inverter.
5. PV generation unit with a suitable interface to enter temperature value, insolation and PV module parameters.
6. Measuring and monitoring system for voltage and power values.

The harmonic content was initially known by monitoring the THD in the examined system at the supply point. Then, the PV system was connected through an inverter to determine the influence of such generator on the THD. The analysis is not restricted to one harmonic value; it is also concerned with studying the effect of radiation and temperature variations on different THD values. This approach provided a better prediction for THD value during daily and seasonally variations.

The data used in modeling the radial power system were obtained from (IDECO) and the main components to operate such system were transformers, medium voltage transmission lines and loads. In addition to that, harmonic sources were presented by nonlinear loads with rectifying devices, whereas PV modules were selected from Centrosolara Company, where the S520P36 Ultra module is used. By using LabVIEW, Harmonic analysis interface is built to give brief results about voltage and current harmonic contents, THD and inter harmonics depending on waveforms taken from Simulink results. Figure 1 shows a single line diagram of the examined distribution section.

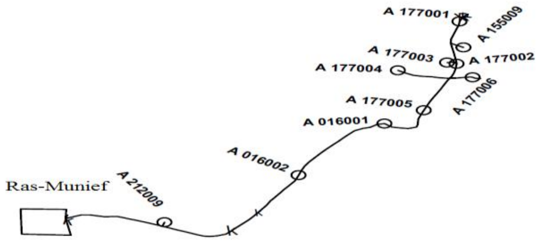

Figure 1. Single line diagram of the distribution section

3. System Simulation and Results

It is expected that the main source of harmonics during the operation of PV system will be the inverter and the harmonic composition in this case will be a function of its capability to convert the DC output of the solar panels into pure AC sine wave. Therefore, a MATLAB/Simulink interface for solar module parameters was built.

3.1. The Harmonic Contents before Connecting PV Arrays

The examined system was initially simulated with its actual load under normal conditions. The measuring point was selected to be at the beginning of the line, directly after the power source. As illustrated in Figure 2, the simulation results have shown the harmonic contents waveforms of the voltages and currents.

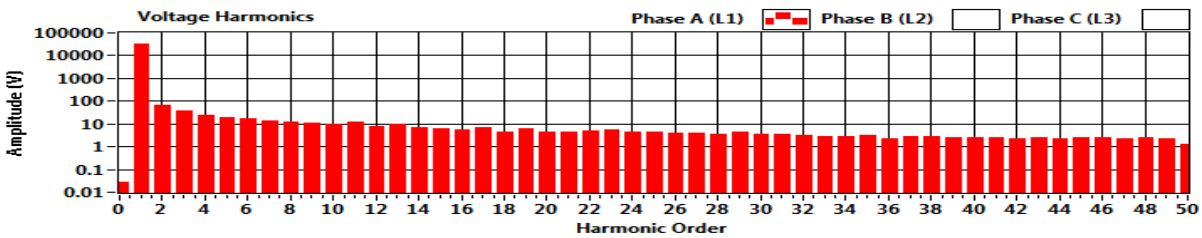

Figure 2 (a). Voltage harmonics shown in phase A

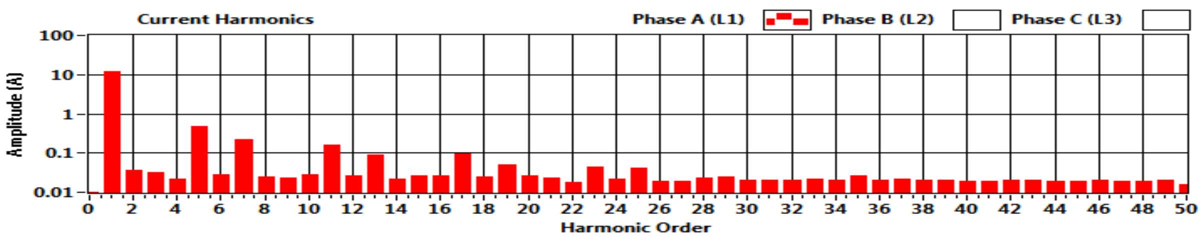

Figure 2 (b). Current harmonicsshown in phase A

The THD_v was evaluated by LabVIEW software and found to be 0.58% whereas the THD_I is 4.7%. The significant harmonic orders are the 5^{th}, 7^{th}, 11^{th}, and 13^{th} which resulted from the operation of six-pulse converters. This is normal for such a system compared with standard values.

Interharmonicswere also taken in consideration when the analysis was done. Figure 3 illustrates sample of measured current interharmonics.

3.2. Harmonic Contents after Connecting the PV Generation

The current-voltage characteristic of PV modules is non-linear and depends on the level of solar irradiance on the surface of the PV modules and their operating temperatures. Therefore, the maximum power point will vary according to the ambient conditions. When the solar irradiance varies at constant temperature, the short-circuit current changes proportionally with the solar irradiance while, the open-circuit voltage changes to a lower extent. However, when the temperature varies at constant solar irradiance level of 1000 W/m2, the open-circuit voltage, in this case, changes in an inverse way with respect to the temperature, whereas the short-circuit current changes to a lower extent. In the operating field, the solar radiance and the temperature change simultaneously which leads to the need to establish test devices. In the PV industry, the standard conditions refer to the temperature of 25°C and to the solar irradiance of 1000 W/m^2, as well as to Air Mass (AM) equal to 1.5, at null wind speed. These conditions refer to a day with clear sky and to a surface having an angle of 41.81° with respect to the horizon [7].

The PV is usually connected to the inverter, the operation of which will be the dominant effect on the production of harmonics. This is attributed to the fact that semiconductor devices are the main components of the inverter and, therefore, it is worth giving this element more concentration regardless of its type. The one employed in the present paper is a pulse width modulation (PWM) inverter with operating switching frequency of 5kHz. Step up chopper is also used before the inverter to provide rms voltage at the second side of the inverter. The voltage is then stepped up to 33kV using a step up transformer to match the distribution voltage connection point. Additionally, a Voltage Source Converter control (VSC) is used to achieve constant AC output value from the inverter with the variation of generation values and this improves the operation of such generation system by keeping the voltage level constant. DC-DC boost converter, inverter and VSC control are assumed to operate as constant parameters in the simulation.

3.2.1. The Effect of Changing of Solar Radiation on Harmonic

By connecting PV system to the grid, it starts supplying part of the distribution load with the required electrical energy. However, the operation of switches and converting devices from DC to AC will cause a non-pure sinusoidal output signal delivered to the grid. The analysis starts at a high value of insolation (1000W/m^2) and then it decreases to illustrate the change of harmonic contents.

The results show that the voltage waveforms have insignificant harmonic distortion compared with that of current waveforms. Figure 4 demonstrates spectrum of current harmonic values in phase A.

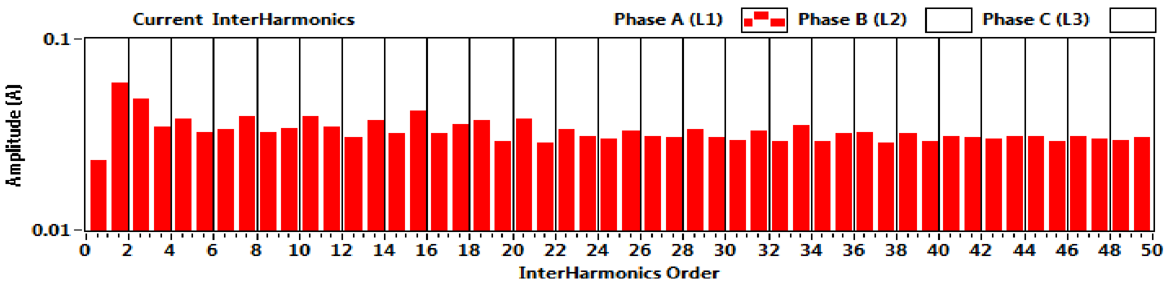

Figure 3. Current interharmonics

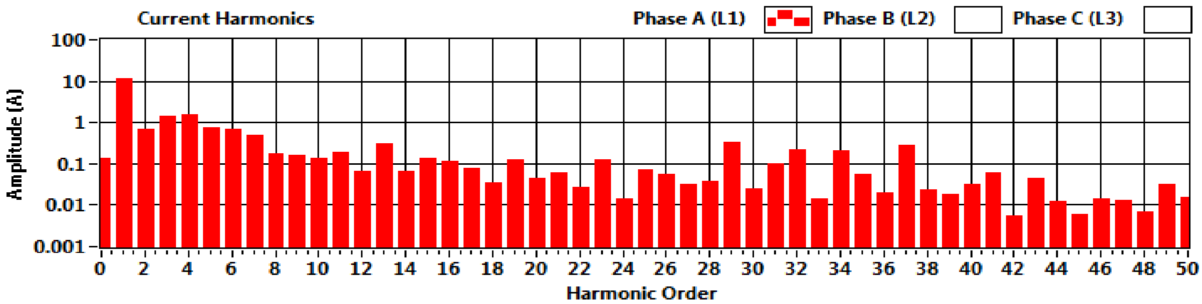

Figure 4. Spectrum of current harmonic values in phase A at insulation level of 1000W/m^2

The resulted THD in current waveforms is 13.3%. This value is much higher than that of the studied system before PV connection.Therefore, the existence of the solar system under normal conditions raised the THD to a very high value. The system was also simulated at 700 W/m^2 and 25^{o}C, which is less than the standard value of solar radiation. In order to investigate the effect of low solar radiation on harmonics, the same parameters were assessed. Figure 5 shows current harmonic values in phase A for this case.

The resulted THD in current waveforms is 13.09% at 700W/m2 solar radiation. For 500 W/m2 insolation, the same process was repeated and Figure 6 shows the spectrum of current harmonics in phase A.

3.2.2. TheEffect of Changing Temperature on Harmonic

In this part of the work the solar radiation will be considered as a constant and the temperature will be the variable factor. The results will be taken at different values of temperatures namely, 30^{o}C, 25^{o}Cand 20^{o}C. In all cases the solar radiation was assumed to be 1000 W/m^2. Figure 7 illustrates the spectrum of current harmonic at temperature of 30^{o}C in phase A.

The resulted THD in current waveforms is 13.3% in this case. Figures 8 and 9 show the spectrum of harmonic current at temperatures of 25oC and 20oC, respectively.

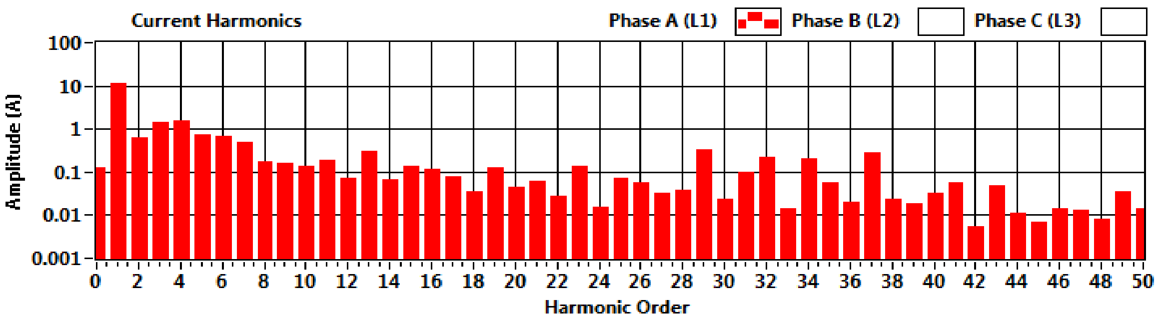

Figure 5. Spectrum of current harmonic values in phase A at insulation level of 700W/m^2

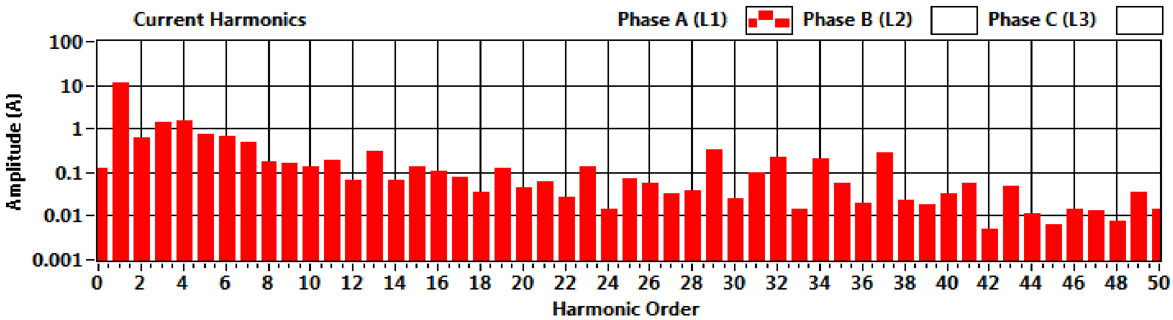

Figure 6. Spectrum of current harmonic values in phase A at insulation level of 500W/m^2 [THD = 13.07%]

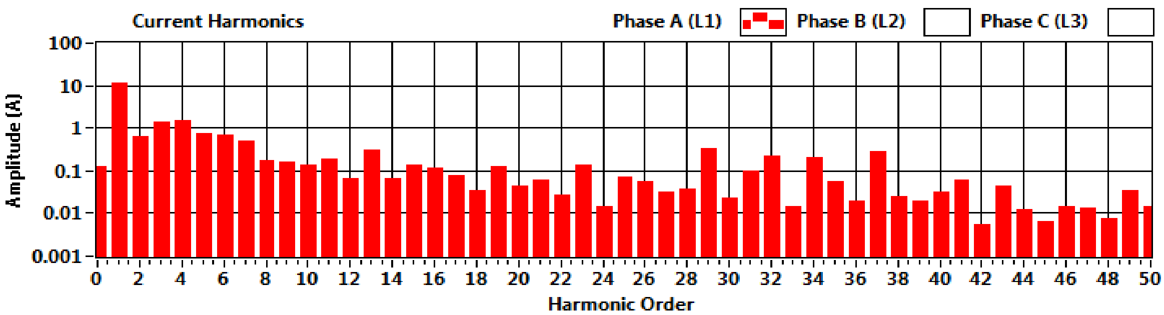

Figure 7. Spectrum of current harmonic in phase A at a temperature of 30^{o}C.

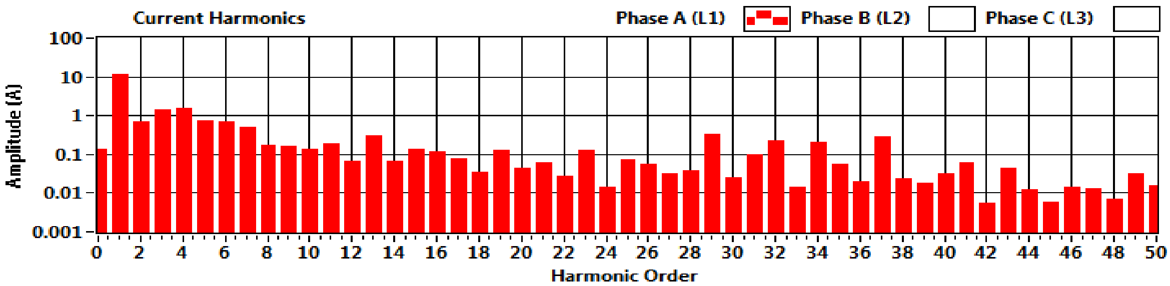

Figure 8. Spectrum of current harmonic in phase A at a temperature of 25^{o}C [THD = 13.3%]

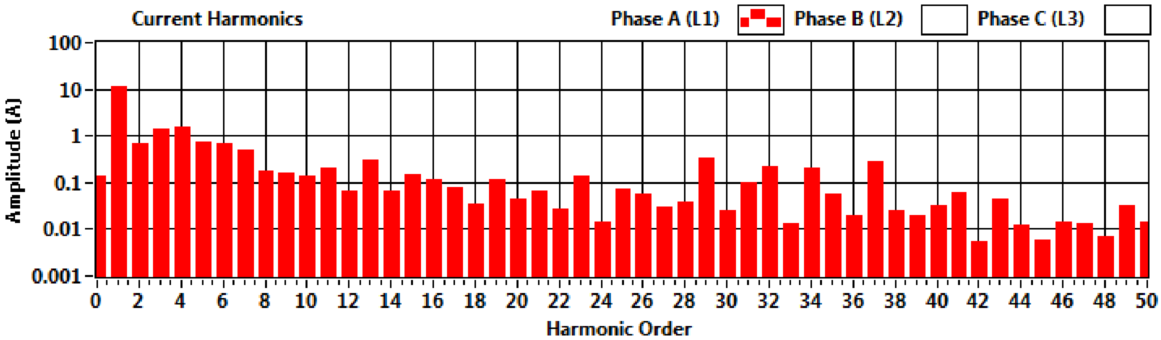

Figure 9.Spectrum of current harmonic in phase A at a temperature of 20^{o}C [THD = 13.4%]

4. Analysis and Discussion

The employment of high performance simulator, which is based on MATLAB/Simulink program, provides a model that can be easily adopted for various temperature and radiation values to set a precise solar generator model. One of the strong points of the present work is the possibility of taking the waveforms of current and voltages obtained from Simulink and analyze them in another tool (LabVIEW). The latter is well-known as a strong tool in harmonic analysis. This approach provides an accurate and effective way in analyzing the variation of parameters governing the harmonic behavior. It simulates a real power system and adds one of renewable resources to existing grids to monitor the effect of integration.

Before connecting the PV system to the distribution network, the THD was found to be 4.6%. Although this factor is a good indication of harmonic level, it is usually advisable to inspect the individual harmonics. In comparison of the harmonic voltage to the harmonic current values, the latter was more noticeable. Usually, the main source of harmonics is the nonlinear loads in the system. However, after connecting PV arrays to the grid, the harmonic level has shown a significant increase. By installing large amounts of PV arrays (in this case 150 kW), the THD level becomes remarkably high (13.2 %). This value reflects the seriousness of the problem and the high percentage of electronic devices involved. The continuous operation of power electronic devices in the inverter and the currents that are injected to the grid are indicators about the degree of distortion that can be sensed during measurements. Any adjacent load will draw a distorted current and by passing through impedances more distortion can be recorded. With time the system becomes completely "polluted" and the THD gets higher and higher. This high value of THD may affect sensitive controlling systems and loads.

The individual harmonics that appear significantly before adding the PV system were the 5th, 7th, 11th and 13th. This is attributed to the six pulse power converter used in the loads. After connecting the PV system, the harmonics were increased because the influence of the inverter in the solar generation system. Even harmonics also appear due to the operation of the transformer between PV system and the grid but with small values.

Solar radiation is one of the main parameters that affect the generation level of PV arrays. It appears from the characteristics that the value of output power from PV arrays will increase as the radiation increases. The variation of the solar radiation occurs in a random manner during cloudy days and varies from day to day, which makes the predicting of the exact value of generation a difficult task. However, the model used can provide the flexibility to change the insolation level to any value, which facilitates prediction the generated power and its influence on the harmonics.

The slight decrease in THD with decreasing the radiation is attributed to the decrease in the value of generated power, and consequently, a less distorted current will be delivered to the grid.

One of the most important factors that affect the operation of all electrical devices is the temperature. The excessive increase in temperature causes less efficient operation of devices in general. Here in PV arrays, the temperature is one of the main dominant factors that affect the generated power by variation the efficiency of PV cells. When running the simulation at a temperature of 30^{o}C, the THD was found to be 13.22 % and then, at 25^{o}C it is found to be 13.3 %. Finally, the THD was 13.4% at 20^{o}C. Therefore, it is not difficult to notice that the temperature decrease causes an increase in the THD in the system. When the temperature increases, the generated power will decrease, so less current delivered to the grid and then less distorted signal presented in the system.

5. Conclusions

The present work has revealed several conclusions. Firstly, the distribution systems, which will be treated as incubators for PV generation, have already some harmonic problems. Although these problems are still not dangerous, but they are in a continuous increase and they might cause serious problems in the future.Secondly, the present work has clearly illustrated that the connection of large scale PV to the distribution grid will significantly increase the THD level and will augment the problem of distribution system performance. The obtained level of THD exceeds the permissible limit for normal operating systems. Finally, the impact of solar radiation and temperature on the harmonic spectrum and THD level was clear. The increase in radiation and the reduction in temperature lead to an increase in the output of the PV, which means an increase in the distorted current and an increase in the harmonic level. However, the change in THD was small in some cases due the selected range of variation.

References

[1] R. A. Messenger and J. Ventre, "photovoltaic system engineering, second edition", Boca Rota, 2004.

[2] F. Batrinu, G. Chicco, J. Schlabbach and F. Spertino," Impacts of grid-connected photovoltaic plant operation on the harmonic distortion", IEEE Electro technical Conf, MELECON pp.861-864, 2006.

[3] P. P. Dash and A. Yazdani, "A Mathematical Model and Performance Evaluation for a Single-Stage Grid-Connected Photovoltaic (PV) System", International Journal of Emerging Electrical Power Systems, Vol. 9, Issue 6, 2008.

[4] I. H. Altas, and A.M. Sharaf, "A Photovoltaic Array Simulation Model forMatlab-Simulink GUI Environment", IEEE Clean Electrical Power Conference ICCEP'07, pp.341-345, 2007.

[5] G. M. S. Azevedo, M. C. Cavalcanti, F. A. S. Neves, L. R. Limongi, K. C. Oliveira, "Grid Connected Photovoltaic Topologies with Current Harmonic Compensation", IEEE Industrial Electronics (ISIE) Symposium, pp. 2394-2399, 2010.

[6] Rita Pinto, Sílvio Mariano, Maria do Rosário Calado and José Felippe de Souza "Impact of Rural Grid-Connected Photovoltaic Generation Systems on Power Quality", Energies 2016, 739; doi:10.3390/en9090739.

[7] V. BARBU, G. CHICCO, F. CORONA, N. GOLOVANOV, F.SPERTINO, "Impact of Photovoltaic Plant Connected to The MV Network On the Harmonic Distortion: An Experimental Assessment", U.P.B. Sci. Bull., Series C, Vol. 75, Iss. 4, 2013.

JJMIE

Volume 10 Number 4, December.2016
ISSN 1995-6665
Pages 245-251

Jordan Journal of Mechanical and Industrial Engineering

Improving Surface Quality of AA 6351 by the Stiff Burnishing Technique

Anil Sureshchandra Maheshwari [a,*], Rupesh Ratnakar Gawande [b]

[a] *Department of Mechanical Engineering, Sandip Institute of Engineering & Management, Nashik. Affiliated to Savitribai Phule Pune University, Pune (Maharashtra), India*

[b] *Department of Mechanical Engineering, Bapurao Deshmukh College of Engineering, Sevagram. Affiliated to Rashtrasant Tukadoji Maharaj Nagpur University, Nagpur (Maharashtra), India*

Received June, 27, 2016 *Accepted September, 20, 2016*

Abstract

Burnishing process is used as a surface treatment for increasing the surface quality of circular or flat surfaces. The present paper investigates the effect of different burnishing parameters (speed, feed, depth of penetration and number of passes) on the surface quality of AA 6351. In conventional flexible burnishing tool, when the ball or roller is pressed against the material, gives waviness on the surface of the component, as properties of material throughout the length of the component are not uniform. Proposed stiff roller burnishing tool (Specially designed for CNC Lathe) can avoid these effects due to its high stiffness. Experimental work based on Response Surface Methodology (RSM), using Central Composite Design was carried out. Statistical Analysis of the results shows that the depth of penetration has a substantial effect on surface roughness and depth of penetration, speed and number of passes has significant effect on microhardness. Optimization of burnishing parameters was done to minimize surface roughness and maximize surface hardness using desirability function. Experiments were performed using optimum level of parameters to prove the effectiveness of desirability function and validate the phenomenon.

Keywords: *Stiff Ball Burnishing, surface roughness, surface hardness, desirability function, AA 6351*.

1. Introduction

In the present scenario, industry demands mechanical components with improved strength to weight ratio and good performance with reliability. Conventional methods like honing, lapping, grinding improves the surface finish of the component, which is not sufficient to improve performance with reliability. To improve the reliability of a component, the surface integrity of the component is to be increased. This can be achieved through numerous processes, like burnishing, shot peening, low plasticity burnishing which can improve the surface integrity of the material. In low plasticity burnishing residual compressive stresses are induced on the surface with less amount of cold work, that increases the fatigue life of the component even at high temperature [1]. For a specific material, we need to find optimum burnishing force, which will give us required surface quality. But if the material is changed, we need to find optimum force for that material. On the other hand, if we consider contact pressure between roller and workpiece material, we need to know the diameter of the roller, contact area, roller material, its shape, and size, as well as workpiece material. By considering various industrial applications of burnishing process on various materials, an extensive database of optimum contact pressure for materials is required to be maintained. This is required if one thinks that optimum contact pressure depends on burnishing process parameters and contact pressure. Therefore the focus of the present investigation is the depth of penetration, which the stiff burnishing tool penetrates the roughness valley, based on initial surface roughness, which can give us better surface quality [2]. Surface integrity is the sum of all the elements that describes all conditions existing on or at the surface of the finished workpiece. Surface integrity has two aspects. The first is surface topography which describes the roughness, lay or texture of the outermost layer of the workpiece. The second is surface metallurgy that describes the nature of the component. Burnishing is the cold working process in which rolling part of the tool, ball or roller is rolled over the surface of the component. As a result of rolling of ball or roller over the surface, Hertz contact stresses are developed, which overstep the yield stress, leading to plastic deformation of the surface layer. This increases surface finish and surface microhardness of the component, which in turn increases the surface integrity of the component [3][4]. Thus, the surface integrity has attracted the interest of researchers, e.g., those who want to increase the life of the component. The functional performance of a component, such as a load bearing capacity, wear resistance, fatigue strength depends on surface integrity which includes surface roughness, surface

* Corresponding author e-mail: maheshwari_anil@rediffmail.com.

hardness, induced compressive stresses and surface topography [5]. Many researchers had studied the effect of different burnishing parameters on, for instance, surface integrity of different materials [6]–[8], surface roughness and microhardness[9]–[12], wear resistance [13][14] and fatigue strength of the different materials, and found that there is improvement in surface finish, surface microhardness, wear resistance, fatigue strength and surface integrity of the material[15]–[17]. Several researchers had optimized burnishing process parameters for enhancing surface quality of material[18]–[21]. However, for optimization of burnishing parameters for a specific material, we need to carry out several experiments with a different combination of burnishing parameters. To minimize the number of experiments Taguchi[22] and RSM[23] were used by many researchers. Dweiri*et al*. [24] used fuzzy modeling for optimization of roller burnishing parameters to improve the surface finish of non-ferrous components. It was observed that as burnishing force increases surface roughness decreases. Revankar[25] investigated optimum burnishing parameters to enhance surface roughness and surface hardness of titanium alloy using Taguchi technique. It was observed that the increase in the burnishing force and number of passes improves the surface finish of the workpiece and the same was the case for hardness but with an increase in speed hardness decreases. RSM and Desirability function was employed for optimization of burnishing parameters and the quadratic model was developed to predict the surface finish of the workpiece [26]. Aluminum alloy is widely used in automobile and aerospace sector due to its properties like high corrosion resistance, high strength to weight ratio. In the present study, AA 6351 was used as a workpiece material. It is most widely used alloy in a wide variety of general applications in small scale industry as well as large scale industries and detailed analysis for burnishing is not found reported. It is also used in pressure vessels, rail and road bridges and can be used in aerospace structure [27].

We need to find out some law in deciding the value of parameters, which will be same for different materials. Here we are concentrating on optimization of the depth of penetration based on initial surface roughness.

2. Stiff Ball Burnishing

Operation of stiff ball burnishing is illustrated in Figure 1. Dynamic behaviour of the burnishing tool is not found reported due to waviness of workpiece surface. Available research does not provide any information on a theoretical or practical aspect of the tool behaviour under real time burnishing process. This is due to the fact that the process is performed on the uneven surface, therefore magnitude of the force acting on the tool cannot be known. Taking into consideration the above fact authors tried to use very high stiffness spring in the tool, so that effect of waviness will not affect the burnishing operation. The depth of penetration is decided based maximum value of Rp (Maximum peak height) on initial surface roughness. The ball is placed on the outer race of the bearing, so that it can rotate freely during burnishing process. The tool is designed in such a way that it will give constant depth of penetration.

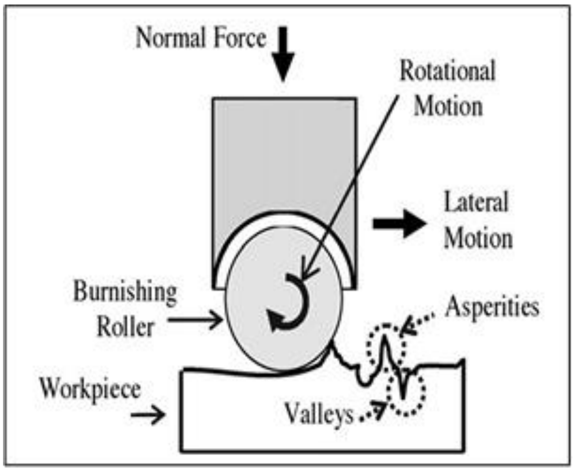

Figure 1. Burnishing Mechanism

3. Experimental Study on Stiff ball Burnishing

Specimens (Size 30mm X 250mm) were prepared on CNC lathe using carbide tip tool having 0.8 mm radius. All burnishing tests were conducted on LMW make CNC lathe having Fanuc Controller at Sandip Institute of Technology and Research Centre, Nashik. Kerosene was used as a coolant. Based on literature review speed, feed, depth of penetration and number of passes were selected as burnishing parameters [28]–[30]. Pilot experiments were conducted, to decide the range of parameters. The experimental work determined the effect of burnishing parameters on surface roughness and hardness. The surface roughness was measured using SURFCOM 130A and surface hardness was measured using Mitutoyo make Micro Vickers Hardness Tester of both turned and burnished surface at Nasik Engineering Cluster (NEC), Nashik. Table 1 shows values of burnishing parameters used.

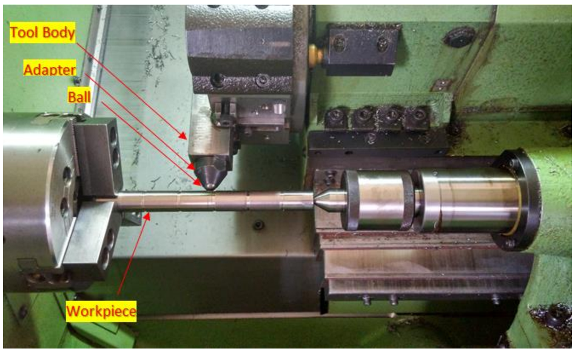

Figure 2. Experimental Setup

Table 1. Burnishing parameters

	Minimum	Intermediate			Maximum
Speed (rpm)	600	700	800	900	1000
Feed (mm/rev)	0.03	0.04	0.05	0.06	0.07
Depth of Penetration(mm)	0.15	0.3	0.45	0.6	0.75
Number of Passes (Units)	1	2	3	4	5

4. Parametric Analysis of Burnishing Process on Surface Roughness and Surface Hardness

In the first stage of the present study based on Response Surface Methodology (RSM) using Central Composite Design (CCD), 30 experiments were conducted using a combination of parameters given in Table 2. The effect of burnishing parameters on the surface roughness and surface microhardness were studied.

Table 2. Design Matrix and Response

Sr No	Speed (rpm)	Feed (mm/rev)	Depth of Penetration (mm)	Number of Passes	Surface Roughness (μm)	Surface Hardness (Hv)
1	1000	0.05	0.45	3	0.063	145.2
2	900	0.04	0.3	4	0.065	143.2
3	900	0.04	0.6	4	0.103	143.8
4	700	0.04	0.3	4	0.067	144.1
5	900	0.06	0.6	2	0.077	143.1
6	800	0.07	0.45	3	0.059	145.8
7	900	0.06	0.6	4	0.079	144.3
8	800	0.05	0.45	3	0.061	146.6
9	600	0.05	0.45	3	0.063	145.3
10	800	0.05	0.45	3	0.06	147.1
11	800	0.05	0.75	3	0.074	145.3
12	700	0.06	0.6	2	0.079	143.8
13	900	0.04	0.3	2	0.068	142.7
14	900	0.06	0.3	4	0.057	144.6
15	700	0.06	0.3	4	0.068	144.2
16	700	0.06	0.6	4	0.0728	142.9
17	700	0.04	0.6	2	0.08	143.5
18	700	0.04	0.6	4	0.079	144.5
19	900	0.04	0.6	2	0.078	144.2
20	700	0.04	0.3	2	0.068	143.8
21	800	0.05	0.15	3	0.063	145.1
22	700	0.06	0.3	2	0.066	144.3
23	800	0.05	0.45	1	0.059	142.1
24	800	0.05	0.45	3	0.061	146.3
25	800	0.05	0.45	3	0.063	146.1
26	800	0.03	0.45	3	0.068	146.5
27	800	0.05	0.45	3	0.059	147.5
28	800	0.05	0.45	3	0.062	147.1
29	800	0.05	0.45	5	0.066	145.5
30	900	0.06	0.3	2	0.068	143.2

ANOVA was used to find the effect of different burnishing parameters on response parameters based on a 95% confidence level. ANOVA for surface roughness quadratic model implied that depth of penetration and quadratic term of, depth of penetration plays an important role in improving the surface finish of the material. Other parameters are found dormant. However, surface microhardness results show that due to a depth of penetration, speed and number of passes (3 to 4) cold work increases which results in, increase in surface hardness. The optimization of burnishing parameters was done using desirability function, to achieve minimum surface roughness and maximum surface hardness. It is found that at speed of 800 rpm, the feed of .05mm/rev., depth of penetration of 0.45 mm and number of passes three, we can get minimum surface roughness and maximum surface hardness. Desirability function value comes 0.814.

Table 3.ANOVA for Response Surface Roughness Quadratic Model

Analysis of variance table [Partial sum of squares - Type III]						
	Sum of		Mean	F	p-value	
Source	Squares	Df	Square	Value	Prob> F	
Model	0.020062	14	0.001433	3.84048853	0.0070	Significant
A-Speed (rpm)	0.000294	1	0.000294	0.7879221	0.3887	
B-Feed (mm/rev)	0.00028	1	0.00028	0.75084867	0.3999	
C-Depth of Penetration (mm)	0.003651	1	0.003651	9.78381276	0.0069	
D-Number of Passes	0.00058	1	0.00058	1.55485081	0.2315	
AB	0.000992	1	0.000992	2.65923709	0.1238	
AC	0.000272	1	0.000272	0.72963195	0.4064	
AD	5.63E-05	1	5.63E-05	0.1507504	0.7033	
BC	0.0004	1	0.0004	1.07200286	0.3169	
BD	0.000676	1	0.000676	1.81168483	0.1983	
CD	0.0001	1	0.0001	0.26800071	0.6122	
A^2	0.000237	1	0.000237	0.63430026	0.4382	
B^2	0.000163	1	0.000163	0.43674545	0.5187	
C^2	0.012168	1	0.012168	32.6106141	< 0.0001	
D^2	6.7E-05	1	6.7E-05	0.17946476	0.6778	
Residual	0.005597	15	0.000373			
Lack of Fit	0.00527	10	0.000527	8.04503817	0.0164	Significant
Pure Error	0.000328	5	6.55E-05			
Core Total	0.025659	29				

The model F-value of 3.84 suggests that model is significant and there is 0.70% chance only that "Model F-Value" this large could occur due to noise. Values of "Prob>F" less than 0.05 indicates that model terms are significant. The "Lack of Fit F-Value" of 8.05 indicates that the lack of fit is significant and there is only 1.64% chance that a "Lack of Fit F-Value" this large could occur due to noise. The value of R^2 is equal to 0.8214. Adequate Precision measures the signal to noise ratio. Signal to noise ratio 9.152 as per present analysis implies an adequate signal to navigate the design space.

The reduced best fitted second order model using least square criteria for surface roughness in coded form is as below:

$$\text{Surface Roughness} = 0.0545 + 0.01333*C + 0.021063*C^2 - 0.005*B*C + 0.0025*C*D - 0.0065*B*D \quad (1)$$

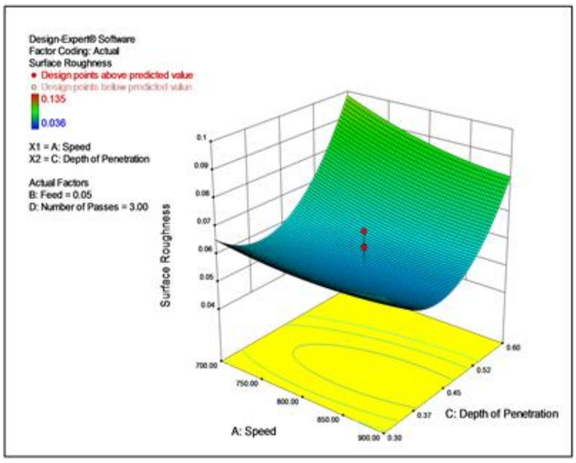

Figure 3. Effect of speed and depth of penetration on surface roughness

Table 4.ANOVA For Surface Hardness Quadratic Model

Analysis of variance table [Partial sum of squares - Type III]						
	Sum of		Mean	F	p-value	
Source	Squares	df	Square	Value	Prob> F	
Model	44.34867	14	3.167762	3.064587	0.0196	significant
A-Speed	0.201667	1	0.201667	0.195098	0.6650	
B-Feed	0.026667	1	0.026667	0.025798	0.8745	
C-Depth of Penetration	0.006667	1	0.006667	0.00645	0.9371	
D-Number of Passes	4.001667	1	4.001667	3.871332	0.0679	
AB	0.25	1	0.25	0.241857	0.6300	
AC	0.7225	1	0.7225	0.698968	0.4163	
AD	0.36	1	0.36	0.348275	0.5639	
BC	1.21	1	1.21	1.17059	0.2964	
BD	0.0025	1	0.0025	0.002419	0.9614	
CD	0.09	1	0.09	0.087069	0.7720	
A^2	10.08107	1	10.08107	9.75273	0.0070	
B^2	3.986786	1	3.986786	3.856936	0.0684	
C^2	10.50107	1	10.50107	10.15905	0.0061	
D^2	25.74107	1	25.74107	24.90268	0.0002	
Residual	15.505	15	1.033667			
Lack of Fit	14.05667	10	1.405667	4.852704	0.0476	significant
Pure Error	1.448333	5	0.289667			
Core Total	59.85367	29				

The model F-value of 3.064 implies that model is significant and there is only 1.96% chance that "Model F-Value" this large could occur due to noise. The "Lack of Fit F-Value" of 4.85 indicates that the lack of fit is significant and there is only 4.76% chance that a "Lack of Fit F-Value" this large could occur due to noise. The value of R^2 is equal to 0.8701. Adequate Precision measures the signal to noise ratio. Our signal to noise ratio 6.526 suggests an adequate signal, to navigate the design space.

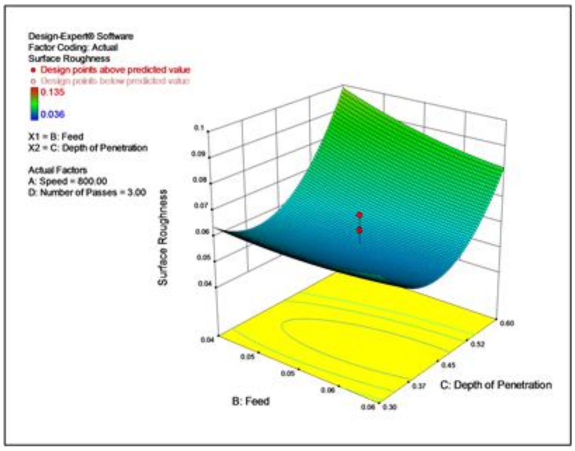

Figure 4. Effect of feed and depth of penetration on surface roughness

The reduced best fitted second order model using least square criteria for surface hardness in coded form is as below:

$$\text{Surface Hardness} = 146.7833 - 0.61875*C^2 - 0.96875*D^2+0.0125*B*D + 0.125*A*B + 0.02125*A*C \quad (2)$$

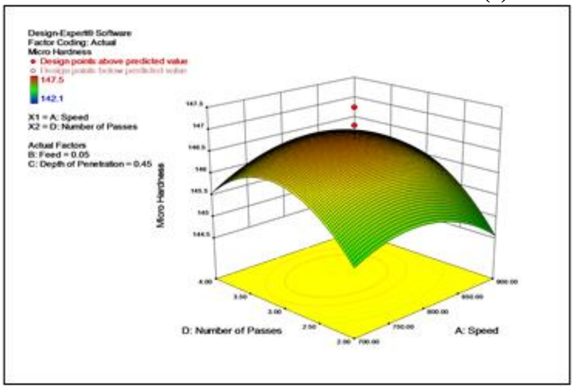

Figure 5. Effect of Number of passes and speed on surface hardness

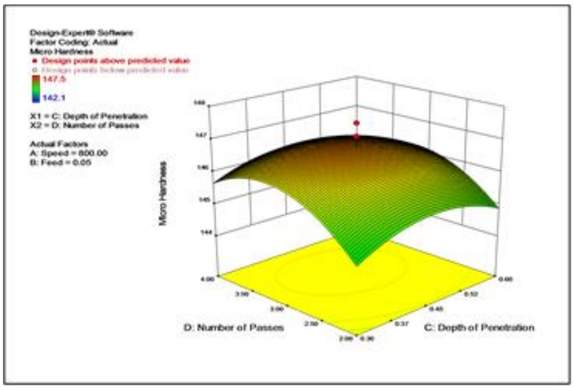

Figure 6. Effect of number of passes and depth of penetration on surface hardness

5. Analysis of the Burnished Surface Quality

5.1. Surface Roughness

In the second stage of the present work, analysis of surface roughness (Ra) was done, in comparison with surface roughness before burnishing. The depth of penetration plays a vital role in improving surface finish. It was observed that depth of penetration equal to 0.8 to 0.9 times Rp (peak value of surface roughness) gives us best surface finish. We were able to get super finished surface having lowest Ra value 0.057 µm, due to stiff burnishing tool.

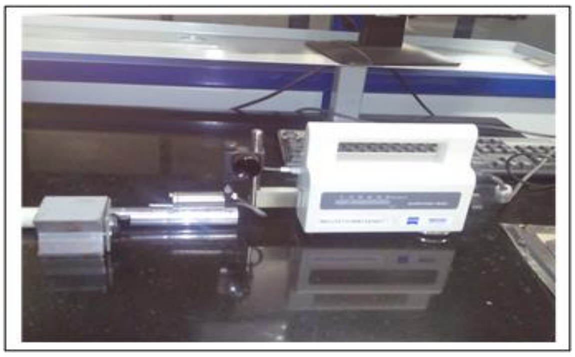

Figure 7. Surface Roughness Tester

5.2. Surface Microhardness

Depth of penetration creates high pressure and plastic deformation of material takes place, which produces limited cold work region. The thickness of the metal layer formed due to pressure increases as the depth of penetration and number of passes are increased. But after a certain value of the depth of penetration and number of passes surface got damaged. Surface hardness obtained was 147.5. Speed also plays role in improving surface hardness. As speed increases, heat generation between tool and workpiece increases and surface of the workpiece becomes soft. So, after 900 rpm speed, surface hardness decreases.

Figure 8. Surface Microhardness Tester

5.3. Optimization of Burnishing parameters

There are two responses, one is surface roughness and the other is surface hardness. We want to minimize surface roughness and maximize surface hardness. Therefore we optimized burnishing parameters. This was done using Desirability function, using software tool. The value of desirability function came as 0.814. Following Table 5 shows upper and lower limit of burnishing parameters, their weight, and importance of each parameter.

Table 5. Burnishing Parameters Range for Optimization

		Lower	Upper	Lower	Upper	
Name	Goal	Limit	Limit	Weight	Weight	Importance
A:Speed	is in range	700	900	1	1	3
B:Feed	is in range	0.04	0.06	1	1	3
C:Depth of Penetration	is in range	0.3	0.6	1	1	3
D:Number of Passes	is in range	2	4	1	1	3
Surface Roughness	minimize	0.057	0.103	1	1	3
Microhardness	maximize	142.1	147.5	1	1	3

5.4. Validation of Mathematical Models

By using burnishing parameters optimum values again, experiments were conducted to validate mathematical models developed. It was observed that % error is less than 10% in almost all tests. Table 6 shows the results of the validation experiments and % error.

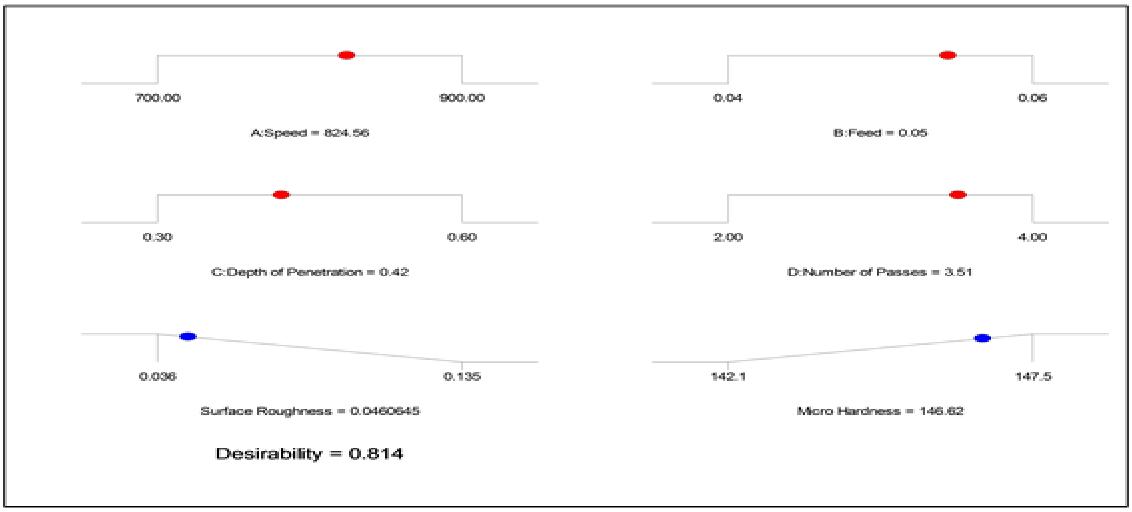

Figure 9. Optimization using Desirability Function

Table 6. Validation Experiments

A	B	C	D	Ra (Measured)	Hv (Measured)	Ra (Predicted)	% Error in Ra	Hv (Predicted)	% Error in Hv
700	0.06	0.6	4	0.078	147.2	0.07434068	4.92236552	145.23855	1.350502329
900	0.04	0.6	4	0.069	149.2	0.07492068	7.902597787	147.03755	1.470678748
900	0.04	0.6	2	0.08	149.1	0.07244068	10.43518642	158.66155	6.026381313
900	0.06	0.3	2	0.063	148.9	0.06102467	3.236936799	155.3416125	4.146739818
900	0.04	0.3	4	0.067	145.6	0.06229467	7.553342846	141.4671125	2.921447556
800	0.05	0.45	3	0.071	146.3	0.067051258	5.88914011	150.5911281	2.849522531
700	0.06	0.3	4	0.063	145.5	0.06174467	2.033098565	140.9431125	3.233139541
700	0.06	0.3	2	0.066	147.8	0.06102467	8.152981409	152.5666125	3.124282844
900	0.06	0.6	4	0.078	146.2	0.07434068	4.92236552	149.28855	2.068845869
900	0.06	0.3	4	0.066	146.4	0.06174467	6.891817545	143.7181125	1.866074814

6. Conclusions

The influence of stiff ball burnishing parameters for improving the surface quality of rotating parts was examined. Along with it, the study of surface roughness and surface hardness achieved was carried out. Based on investigations achieved, subsequent conclusions are drawn:

- The depth of penetration plays important role in enhancement of surface finish up to certain value. As the depth of penetration increases, pressure on the workpiece surface increases and plastic deformation at the surface of the workpiece takes place. Due to this, material will flow into the valleys and we can get the better surface finish. But if it increases beyond a particular limit surface get damaged, as a combination of parameters is giving us required result.
- Burnishing speed, feed, and a number of passes hardly affect the surface roughness. Thus, it is possible to use maximum speed and feed to reduce process time. And we can keep the number of passes as one only. But we can increase speed and feed up to a certain limit, otherwise, the surface may get damaged. There is an interaction between different burnishing parameters used.
- Speed, Depth of penetration and number of passes are critical parameters to enhance surface hardness. But we need to take them at a particular level, as increase or decrease in values can reduce surface hardness. As the depth of penetration and number of passes increases, surface hardness increases, but if values are too high surface will be get damaged, results into increase in surface roughness. Therefore optimum values of burnishing parameters are the key elements to achieve minimum surface finish and maximum surface hardness.
- The depth of penetration is equal to 0.8 to 0.9-times maximum peak height of the surface roughness. This means we can decide the depth of penetration for any material based on initial surface.

Acknowledgement

The authors express their sincere thanks to Mr. Y. S. Pawar, Director of Mech. India Pvt. Ltd., Dombival for continuous support and timely guidance for the present research. The authors are grateful to authorities of Sandip Institute of Technology & Research Centre for allowing us to carry out experimentation in the workshop.

References

[1] D. Hornbach, P. Prevey, and E. Loftus, “Application of Low Plasticity Burnishing (LPB) to Improve the Fatigue Performance of Ti-6Al-4V Femoral Hip Stems,” *J. ASTM Int.*, vol. 3, no. 5, p. 13580, 2006.

[2] B. Tadic, S. Randjelovic, P. Todorovic, J. Zivkovic, V. Kocovic, I. Budak, and D. Vukelic, “Using a high-stiffness burnishing tool for increased dimensional and geometrical accuracies of openings,” *Precis. Eng.*, vol. 43, pp. 335–344, 2016.

[3] B. Tadic, P. M. Todorovic, O. Luzanin, D. Miljanic, B. M. Jeremic, B. Bogdanovic, and D. Vukelic, “Using specially designed high-stiffness burnishing tool to achieve high-quality surface finish,” *Int. J. Adv. Manuf. Technol.*, vol. 67, no. 1–4, pp. 601–611, 2013.

[4] J. a. Travieso-Rodriguez, G. G. Gras, J. J. Peiró, F. Carrillo, G. Dessein, J. Alexis, and H. G. Rojas, “Experimental Study on the Mechanical Effects of the Vibration-Assisted Ball-Burnishing Process,” *Mater. Manuf. Process.*, vol. 30, no. 12, pp. 1490–1497, 2015.

[5] M. H. El-Axir and M. M. El-Khabeery, “Influence of orthogonal burnishing parameters on surface characteristics for various materials,” *J. Mater. Process. Technol.*, vol. 132, no. 1–3, pp. 82–89, 2003.

[6] A. Sequera, C. H. Fu, Y. B. Guo, and X. T. Wei, “Surface Integrity of Inconel 718 by Ball Burnishing,” *J. Mater. Eng. Perform.*, vol. 23, no. 9, pp. 3347–3353, 2014.

[7] H. Hamadache, L. Laouar, N. E. Zeghib, and K. Chaoui, “Characteristics of Rb40 steel superficial layer under ball and

roller burnishing," *J. Mater. Process. Technol.*, vol. 180, no. 1–3, pp. 130–136, 2006.

[8] S. Purushothaman, "Prediction of Burnishing Surface Integrity using Radial Basis Function Turned part Burnishing Workpiece Burnishing," vol. 6, no. 3, pp. 391–399, 2011.

[9] T. a. El-Taweel and M. H. El-Axir, "Analysis and optimization of the ball burnishing process through the Taguchi technique," *Int. J. Adv. Manuf. Technol.*, vol. 41, no. 3–4, pp. 301–310, 2009.

[10] M. H. El-Axir, O. M. Othman, and A. M. Abodiena, "Study on the inner surface finishing of aluminum alloy 2014 by ball burnishing process," *J. Mater. Process. Technol.*, vol. 202, no. 1–3, pp. 435–442, 2008.

[11] A. M. Hassan, "The effects of ball- and roller-burnishing on the surface roughness and hardness of some non-ferrous metals," *J. Mater. Process. Technol.*, vol. 72, no. 3, pp. 385–391, 1997.

[12] F. Gharbi, S. Sghaier, H. Hamdi, and T. Benameur, "Ductility improvement of aluminum 1050A rolled sheet by a newly designed ball burnishing tool device," *Int. J. Adv. Manuf. Technol.*, vol. 60, no. 1–4, pp. 87–99, 2012.

[13] N. S. M. El-Tayeb, K. O. Low, and P. V Brevern, "Influence of roller burnishing contact width and burnishing orientation on surface quality and tribological behaviour of Aluminium 6061," *J. Mater. Process. Technol.*, vol. 186, no. 1–3, pp. 272–278, 2007.

[14] K. S. Rababa, M. M. Al-mahasne, and P. O. Box, "Effect of Roller Burnishing on the Mechanical Behavior and Surface Quality of O 1 Alloy Steel," *Res. J. Appl. Sci. Eng. Technol.*, vol. 3, no. 3, pp. 227–233, 2011.

[15] J. Byrne, J. I. M. Byrne, R. a Cláudio, and A. Burgess, "Resisting Metal Fatigue in Aeroengines , Surface Damage and Surface Treatments," vol. 20, pp. 30–39, 2008.

[16] G. H. Majzoobi, F. Zare Jouneghani, and E. Khademi, "Experimental and numerical studies on the effect of deep rolling on bending fretting fatigue resistance of Al7075," *Int. J. Adv. Manuf. Technol.*, vol. 82, no. 9–12, pp. 2137–2148, 2015.

[17] M. Salahshoor and Y. B. Guo, "Process mechanics in ball burnishing biomedical magnesium-calcium alloy," *Int. J. Adv. Manuf. Technol.*, vol. 64, no. 1–4, pp. 133–144, 2013.

[18] C. S. Jawalkar and R. S. Walia, "Study of roller burnishing process on En-8 specimens using design of experiments," vol. 1, no. 1, pp. 38–45, 2009.

[19] a.M. Hassan, H. F. Al-Jalil, and a.a. Ebied, "Burnishing force and number of ball passes for the optimum surface finish of brass components," *J. Mater. Process. Technol.*, vol. 83, no. 1–3, pp. 176–179, 1998.

[20] P. R. Babu, K. Ankamma, T. S. Prasad, a. V. S. Raju, and N. E. Prasad, "Optimization of burnishing parameters and determination of select surface characteristics in engineering materials," *Sadhana - Acad. Proc. Eng. Sci.*, vol. 37, no. August, pp. 503–520, 2012.

[21] U. Esme, "Use of grey based Taguchi method in ball burnishing process for the optimization of surface roughness and microhardness of AA 7075 aluminum alloy ," *Uporab. grey-Taguchijeve Metod. pri procesu glajenja za Optim. povr[inske hrapavosti mikrotrdote Alum. zlitine AA 7075*, vol. 44, no. 3, pp. 129–135, 2010.

[22] F. J. Shiou and C. C. Hsu, "Surface finishing of hardened and tempered stainless tool steel using sequential ball grinding, ball burnishing and ball polishing processes on a machining centre," *J. Mater. Process. Technol.*, vol. 205, no. 1–3, pp. 249–258, 2008.

[23] M. S. Said, J. a Ghani, M. S. Kassim, S. H. Tomadi, C. Hassan, and C. Haron, "Comparison between Taguchi Method and Response Surface Methodology (RSM) In Optimizing Machining Condition," *Int. Conf. Robust Qual. Eng.*, pp. 60–64, 2013.

[24] F. Dweiri, A. M. Hassan, A. Hader, and H. Al-Wedyan, "Surface Finish Optimization of Roller Burnished Nonferrous Components by Fuzzy Modeling," *Mater. Manuf. Process.*, vol. 18, no. 6, pp. 863–876, 2003.

[25] G. D. Revankar, R. Shetty, S. S. Rao, and V. N. Gaitonde, "Selection Of Optimal Process Parameters In Ball Burnishing Of Titanium Alloy," *Mach. Sci. Technol.*, vol. 18, no. 3, pp. 464–483, 2014.

[26] A. Sagbas, "Analysis and optimization of surface roughness in the ball burnishing process using response surface methodology and desirabilty function," *Adv. Eng. Softw.*, vol. 42, no. 11, pp. 992–998, 2011.

[27] O. F. Mechanical, "IJMET © I A E M E EXPERIMENTAL INVESTIGATION OF TENSILE STRENGTH ON AL 6351," pp. 110–114, 2014.

[28] M. H. El-Axir, O. M. Othman, and A. M. Abodiena, "Improvements in out-of-roundness and microhardness of inner surfaces by internal ball burnishing process," *J. Mater. Process. Technol.*, vol. 196, no. 1–3, pp. 120–128, 2008.

[29] M. M. El-Khabeery and M. H. El-Axir, "Experimental techniques for studying the effects of milling roller-burnishing parameters on surface integrity," *Int. J. Mach. Tools Manuf.*, vol. 41, no. 12, pp. 1705–1719, 2001.

[30] S. Thamizhmnaii, B. Bin Omar, S. Saparudin, and S. Hasan, "Surface roughness investigation and hardness by burnishing on titanium alloy," *Manuf. Eng.*, vol. 28, no. 2, pp. 13–14, 2008.

JJMIE

Volume 10 Number 4, December. 2016
ISSN 1995-6665
Pages 253 - 261

Jordan Journal of Mechanical and Industrial Engineering

Two-Dimensional Analysis of Low Pressure Flows in the Annulus Region between Two Concentric Cylinders with Solid Fins

Wael Al-Kouz[a*], Suhil Kiwan[b], Aiman Alshare[c], Ahmad Hammad[c], Ammar Alkhalidi[d]

[a] *Mechatronics Engineering Department, German Jordanian University, Amman, 11180, Jordan*

[b] *Mechanical Engineering Department, Jordan University of Science and Technology, Irbid, 22110, Jordan*

[c] *Mechanical and Maintenance Engineering Department, German Jordanian University, 11180, Jordan*

[d] *Energy Engineering Department, German Jordanian University, 11180, Jordan*

Received August, 17, 2016 *Accepted November, 17, 2016*

Abstract

A finite volume code is used to solve for the steady-state two-dimensional laminar natural convection heat transfer for the gaseous low pressure flows in the annulus region between two concentric horizontal cylinders with an attached solid fin to the inner cylinder. Such flows can be found in the "evacuated" solar collectors and in the receivers of the solar Parabolic Trough Collectors (PTCs). Boussinesq approximation is utilized to model the buoyancy effect. It is found that Nusselt number (*Nu*) depends inversely on Knudsen number and directly on Rayleigh number. In addition, it is found that attaching a solid fin to the inner cylinder will enhance the heat transfer for such flows. Also, It is found that by increasing the tilt angle of the solid fin, then better heat transfer is achieved. Finally, it is concluded that by increasing the conductivity ratio, better heat transfer is gained.

Keywords: natural convection, heat transfer, low pressure, concentric cylinders, solar collectors, parabolic trough.

Nomenclature

C_p	Specific heat [J kg^{-1} K^{-1}]
D	Molecular diameter of the gas [m]
D_i	Inner annulus diameter [m]
D_o	Outer annulus diameter [m]
E	Energy flux on a surface per unit time
g	Gravity acceleration [m/s^2]
k	Thermal conductivity [W m^{-1} K^{-1}]
k_B	Boltzman constant= $1.38066\times10^{-23}\,JK^{-1}$
k_{eff}	Effective thermal conductivity [W m^{-1} K^{-1}]
Kn	Knudsen number
K_r	Fin thermal conductivity ratio
k_r	Effective thermal conductivity ratio (k_{eff}/k_f)
L	Length of the cylinder [m]
L_g	Gap Spacing between the two cylinders (r_o-r_i) [m]
$\overline{L_g}$	Dimensionless gap spacing between the two cylinders (r_o-r_i)/r_i
P	Pressure [Pa]
Pr	Prandtl number
Q	Heat transfer [W]
q_w	Local heat flux [W/m^2]
r_i	Inner annulus radius [m]
r_o	Outer annulus radius [m]
T	Temperature [K]
T_i	Temperature of annulus inner surface [K]
T_o	Temperature of annulus outer surface [K]
Ra	Rayleigh number ($g\beta(T_1-T_2)L^3/\alpha\nu$)
Ra_c	Rayleigh number based on L_c =($g\beta(T_1-T_2)L_c^3/\alpha\nu$)
Ra_i	Rayleigh number based on the inner diameter
Ra_m	Modified Rayleigh number
u	Velocity in x-direction [m/s]
v	Velocity in y-direction [m/s]
x, y	Cartesian coordinates [m]
x'	Line, starting from point a and ending at point b [m]
$\overline{X}$	Dimensionless $x' = \frac{x'}{r_o}$

Greek Symbols

α	Thermal diffusivity [m^2/s]
β	Thermal expansion coefficient [1/K]
λ	Molecular mean free path (m)
μ	Dynamic viscosity [kg m^{-1} s^{-1}]
ν	Kinematic viscosity [m^{2}s^{-1}]
φ	Angle as shown in Figure 1
ρ	Density of air, given by ideal gas equation (P/RT), [Kg/m^3]
σ	Lennard-Jones characteristic length (A^o)
σ_T	Thermal accommodation coefficient
σ_v	Momentum accommodation coefficient

* Corresponding author e-mail wael.alkouz@gju.edu.jo.

τ Tangential momentum

Θ Dimensionless temperature

Subscripts

eff Effective

f Fluid

F Fin

g Gap

i Inner

m Modified

n Normal

o Outer

r Ratio

1. Introduction

Rarefied and micro/nano flows have been studied extensively in the past two decades because of their relevance to the MEMS and NEMS devices as well as their wide applications found in the industry, such as aerospace, plasma and material processing applications [1; 2]. Recently, the whole world has started to depend on renewable energy as it produces no harmful pollutants to the environment and due to energy bill savings. Solar energy is one of the cleanest forms of renewable energy that is sustainable, inexhaustible, and inexpensive. In addition, solar energy is becoming more appealing as it can be gained without any restrictions. Researchers have investigated and developed technologies on how to harvest solar energy and to maximize the collection and utilization of solar energy. One of the most important applications for the rarefied flows that is related to the solar energy applications is the Parabolic Trough Collectors (PTCs) found in power plants. Since heat transfer analysis for PTCs is important for efficiency estimation of the power plant [3], this study aims to investigate the effect of attaching a fin to the inner cylinder on the flow and heat characteristics of the low pressure gaseous flow confined in the annulus region of two concentric cylinders. Also, the effect of Knudsen number and Rayleigh number on these characteristics will be addressed as well.

Rarefied flows can be classified by introducing Knudsen number (Kn). It represents the ratio of the mean free path (λ) to the characteristic length (L) of the geometry of interest.

Based on the study of Schaaf and Chambre [4] and that of Cercignani and Lampis [5], one can classify the flow regimes into four types: (i) Continuum regime if $Kn < 0.01$; (ii) Slip regime if $0.01 < Kn < 0.1$; (iii) Transitional regime if 1< Kn <10; and (iv) for $10 < Kn$, the free molecular regime. It is also worth to mention that in the slip flows, the slip boundary condition is applied at the surfaces and if the flow is non-isothermal, a temperature jump at the surface must be applied as well, while for the transitional and free molecular regimes, particle simulation methods, such as direct simulation Monte Carlo method, can be used to analyze the flow characteristics. For example, the supersonic gaseous flows into nanochannels using the unstructured 3-D direct simulation Monte Carlo method had been studied by Gatsonis *et al*. [6]. It was shown that the flow and heat transfer characteristics are affected by inlet Mach number (Ma), inlet pressure and the aspect ratio of the channel.

Similarity method is another technique that was utilized to solve for the flow and heat characteristics for continuum and rarefied flows. For instance, Kiwan and Al-Nimr [7] used the power law along with the similarity solution to solve for the flow and heat characteristics of a flow over a stretched microsurface. Also, Kiwan and Al-Nimr [8] used the same technique (similarity) to investigate the flow and heat characteristics for boundary layer flows in microsystems. In addition, Al-Kouz *et al*. [9] investigated the flow and heat transfer for rarefied flows over stretched surfaces using the similarity solution as well.

Flow in the region between two horizontally oriented concentric cylinders has been extensively studied experimentally and numerically in the past decades due to its relevance to parabolic trough solar collectors. The present paper provides further insight on the gaseous flow and heat transfer characteristics in the cavity of the annular region between two concentric cylinders, in which the inner cylinder is attached to a solid fin.

A comprehensive literature review for the computational and experimental investigations for the no-slip flow in the region of the annuli between two concentric cylinders is summarized by Kuehn and Goldstein [10; 11]. Moreover, Kuehn *et al*. [10] obtained a correlation using the conduction boundary layer model for the flow in the annulus region between to concentric horizontal cylinders. Raithby and Hollands [12] provided the following correlations for the conductivity ratio and length scale that is valid for $0.7 \le \Pr \le 6000$ and $Ra_c \le 10^7$ for the flow in the annulus region between two concentric cylinders:

$$k_r = \frac{k_{eff}}{k} = 0.386\left(\frac{\Pr}{0.861+\Pr}\right)^{1/4} Ra_c^{1/4} \tag{1}$$

where k_{eff} represents effective conductivity of the fictitious stationary fluid that will transfer the same amount of heat as the actual moving fluid, and L_c is given as follows:

$$L_c = \frac{2\left[\ln\left(r_\circ / r_i\right)\right]^{4/3}}{\left(r_i^{-3/5} + r_\circ^{-3/5}\right)^{5/3}} \tag{2}$$

Mack and Bishop [13] investigated the free convection in the annulus region between two concentric cylinders. In their study, they represented the stream function and the temperature variables using the third power of the Rayleigh number. The effects of Raleyigh number and radius ratio on the characteristics of the flow in the annuli of two infinite concentric cylinders using numerical techniques were studied by El-Sherbiny [14]. Rayleigh number was varied between 10^2 to 10^6, and the Radius Ratio, (RR) was taking the values between 1.25 and 10.

In his study, Mikhail A. Sheremet [15] investigated the effect of Ra, Pr, the inclination angle as well as the thermal conductivity ratio on the velocity and temperature fields of the laminar natural convection in an inclined cylindrical enclosure having finite thickness walls. The selected values for Rayleigh number were $Ra = 10^4$, 5×10^4, 10^5, while Prandtl number was varied to take the values of Pr = 0.7 and 7.0, the inclination angle values were 0, $\pi/6$, $\pi/3$, $\pi/2$ and the thermal conductivity ratio values of 5.7×10^{-4} and 4.3×10^{-2} is selected. The results show that it is possible to indicate two intervals with a maximum magnitude of the generalized heat transfer coefficient at various values of the inclination angle of the tube and the analyzed range of Rayleigh number while the increase in Prandtl number is reflected in a delay in the thermal stabilization zone. It was also shown that for a certain range of the Rayleigh number less than 1×10^5, the thermal component of the natural convection is dominant while for Rayleigh number greater than 1×10^5 the hydrodynamic component of natural convection is the dominant.

Bouras *et al*. [16] developed a finite volume code to solve for the governing equations resulted from the Boussinesq approximation and the velocity stream function formulation to investigate the effect of Prandtl number as well as Rayleigh number for the natural convection in the annulus space between two elliptical confocal cylinders. It was found that the heat transfer increases as the Rayleigh number increases. Low Rayleigh numbers makes the conduction heat transfer dominant while high Rayleigh numbers makes the convection heat transfer dominant. They also concluded that for low Rayleigh numbers there is no effect for Prandtl number on the heat transfer but for higher Rayleigh numbers increasing Prandtl number increases the heat transfer.

The effect of fin conductivity ratio, Darcy number and Rayleigh number on the average Nusselt number for porous fins attached to the inner cylinder of the annulus between two concentric cylinders were investigated by Kiwan *et al*. [17]. They found that the heat transfer is enhanced for the case of a porous fin, also it was found that for porous fin, unlike the solid fins, the heat transfer decreases by increasing the inclination angle of the fin. Bouras *et al*. [18] numerically investigated the double diffusive natural heat transfer convection in the annular space between confocal elliptic shape enclosures using a finite volume code to solve the governing equations. They found that both heat and mass transfer increase with increasing Rayleigh number. Furthermore, the iso-concentrations exhibit a plume as iso-therms at large Rayleigh numbers. The plume diffuse throughout the annular space since the Lewis number is greater than one.

The natural convection heat transfer of nanofluids in annular spaces between horizontal concentric cylinders was investigated by Cianfrini *et al*. [19]. They developed two empirical equations based on a wide variety of experimental data and used them for evaluation of the nanofluid effective thermal conductivity and dynamic viscosity, while the other effective properties are calculated based on the mixing theory. Different conditions, such as the diameter of the particles was considered in calculated the heat transfer enhancement due to the nanoparticles dispersion in the liquid, and they concluded that there is an optimum particle loading for the maximum heat transfer.

Chamissem *et al*. [20] investigated the effect of Rayleigh number for natural convection in annular space flows. They found that there is a possibility to get a multi-cellular flows if the enclosure impedes movement of the fluid even if the Rayleigh number is small. They found an interval of large Rayligh numbers where the relaxation coefficients do not only affect the speed of calculation convergence but also the solution of the transfer equation. The effect of the relaxation coefficients on the solution is not valid beyond this interval. In the case of very large Rayleigh numbers, the stream function takes two values just before the divergence of the solution, this is very clear for the cases where symmetry boundary conditions is in the vertical direction.

The parabolic trough solar receiver is one of the applications for the flow in the annulus region between two horizontal concentric cylinders. The heat transfer of this application was analyzed by Padilla *et al*. [21]. They validated their model by comparison to Sandia National Laboratory (SNL) parabolic trough solar collector test (SEGS LS-2) in which the inner diameter of the receiver is 70 mm while the outer diameter is 115 mm. Based on their model they presented correlations for the heat transfer in the parabolic trough solar receiver.

Al-Kouz *et al*. [22] investigated the low-pressure flows in the annulus region between two concentric cylinders; they studied the effect of rarefaction on the flow and heat characteristics of such flows. In addition, a correlation for the conductivity ratio was proposed for such flows.

Vacuum pressure that operates the receivers of the parabolic trough collectors and the evacuated tube collectors is related to the operating temperature and the mean free path can be found in [1; 2] as:

$$\lambda = \frac{k_B T}{\sqrt{2}\pi d^2 P} \tag{3}$$

where k_B is the Boltzmann constant, T the temperature, P the pressure, d is molecular diameter of the gas under investigation and λ is the mean free path.

In the present work, a finite volume numerical Computational Fluid Dynamics (CFD) solution utilizing Boussinesq approximation is used to obtain the solution for the natural convection heat transfer characteristics between two concentric horizontal cylinders. The inner cylinder is attached to a solid fin and is subjected to a constant high temperature while the outer cylinder is held at constant lower temperature. Prandtl number (*Pr*) is taken to be constant and is equal to 0.701. Effects of Knudsen number (*Kn*), Ralyeigh number (*Ra*), fin inclination angle and the conductivity ration on the flow and heat transfer characteristics are investigated.

2. Mathematical Formulation

2.1. Governing Equations

In the present study, a steady-state, two dimensional, and laminar flow is investigated. Boussinesq approximation is utilized to account for the buoyancy force and all fluid properties are considered constant.

Figure (1.a) shows one of the most relevant applications to our study, namely the receiver of the parabolic trough collectors. Fig (1.b) illustrates the geometry of the flow in the annulus region between the two concentric cylinders in which the inner cylinder is attached to a solid fin. In the present study, the slip and temperature jump boundary conditions were imposed at the boundaries and the slip flow regime is investigated.

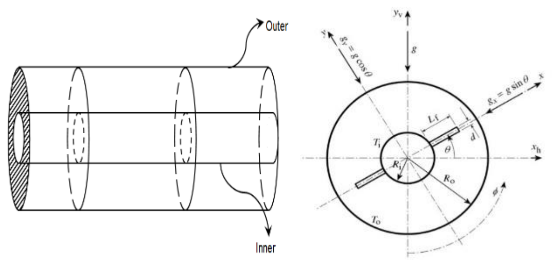

(a) (b)

Figure 1. (a) Parabolic trough receiver, (b) The geometry used for the computational domain, the annular region between two concentric cylinders with a solid attached fin

The governing equations that describe the problem under investigation are summarized below:

Conservation of mass:

$$\frac{\partial u}{\partial x}+\frac{\partial v}{\partial y}=0 \tag{4}$$

x-momentum:

$$\rho u\frac{\partial u}{\partial x}+\rho v\frac{\partial u}{\partial y}=-\frac{\partial P}{\partial x}+\rho g_x+\mu\left[\frac{\partial^2 u}{\partial x^2}+\frac{\partial^2 u}{\partial y^2}\right] \tag{5}$$

Note that the x component of the gravity is not equal to zero since there is a rotation for the solid fin that is attached to the inner cylinder of the annulus.

y-momentum:

$$\rho u\frac{\partial v}{\partial x}+\rho v\frac{\partial v}{\partial y}=-\frac{\partial P}{\partial y}-\rho g_y+\mu\left[\frac{\partial^2 v}{\partial x^2}+\frac{\partial^2 v}{\partial y^2}\right] \tag{6}$$

Energy:

$$\rho C_p u\frac{\partial T}{\partial x}+\rho C_p v\frac{\partial T}{\partial y}=k\left[\frac{\partial^2 T}{\partial x^2}+\frac{\partial^2 T}{\partial y^2}\right] \tag{7}$$

To estimate the fluid density, the ideal gas state equation is provided as an input:

$$\rho=\frac{P}{RT} \tag{8}$$

The boundary conditions applied are the slip and temperature jump at the inner and outer walls of the annulus, reported by Karniadakis *et al*. [1], Lockerby *et al*. [23] and Colin [24] as follows:

$$u_w-u_g=\left(\frac{2-\sigma_v}{\sigma_v}\right)\lambda\frac{\partial u}{\partial n}\approx\left(\frac{2-\sigma_v}{\sigma_v}\right)K_n\left(u_g-u_c\right) \tag{9a}$$

$$v_g=0 \tag{9b}$$

$$T_w-T_g=\left(\frac{2-\sigma_T}{\sigma_T}\right)\frac{2\gamma}{\gamma+1}\frac{k}{\mu c_v}\lambda\frac{\partial T}{\partial n}\approx\left(\frac{2-\sigma_T}{\sigma_T}\right)\frac{2\gamma}{\gamma+1}\frac{k}{\mu c_v}K_n\left(T_g-T_c\right) \tag{9c}$$

In equations (8a) and (8b), u_c and T_c represent the tangential velocity and temperature of the first cell from the wall in the computational domain. σ_v and σ_T represent the momentum and thermal accommodation coefficients and used as an inputs in the simulations, where:

$$\sigma_v=\frac{\tau_i-\tau_r}{\tau_i-\tau_w} \tag{10}$$

Where τ_i represents the tangential momentum of incoming particles to a certain surface (wall) and τ_r represents the tangential momentum of the reflected particles from that surface. While, τ_w is the tangential momentum of reemitted molecules from the surface with a temperature equal to the surface (wall) temperature:

$$\sigma_T=\frac{dE_i-dE_r}{dE_i-dE_w} \tag{11}$$

where dE_i is the energy flux of the incoming particles on a surface per unit time, dE_r represents the energy flux of the reflected particles per unit time, and dE_w denotes the energy flux of all the incoming particles that had been reemitted with the energy flux corresponding to the surface temperature T_w.

The corresponding Knudsen number (Kn) is defined as follows:

$$Kn=\frac{\lambda}{L_g} \tag{12}$$

where L_g is the gap spacing between the inner and outer cylinders.

Thermal boundary conditions are imposed at $r=r_i$ and r_o such that:

At $r=r_i$, $T=T_i$ (13)

At $r=r_{out}$, $T=T_o$ (14)

where T_i is the hot surface temperature and T_o is the cold surface temperature.

The local heat flux at the is calculated using Fourier's law of conduction at the surfaces of the inner cylinder and the fin as follows:

$$q_F=-k\frac{\partial T}{\partial n}\Big|_F \tag{15}$$

and $$q_i=-k\frac{\partial T}{\partial n}\Big|_i \tag{16}$$

Since the problem is steady, the heat transfer from the inner to the outer wall is calculated by integrating the local heat flux along the wall of the inner cylinder and the fin:

$$Q=\sum\left(\int_{A_i}q_i\,dA_i+\int_{A_F}q_F\,dA_F\right) \tag{17}$$

Then, the average heat transfer coefficient along the walls of the inner cylinder and the fin is calculated by combining equations 15, 16 and 17:

$$\bar{h}=\frac{Q}{(T_i-T_o)A_T} \tag{18}$$

From equation 19, the average Nusselt number can be calculated.

Price *et al*. [25] and Thomas [26] investigated the flow in the parabolic trough solar collector receiver, they lower the pressure in the annulus to a value that is less than one Torr, they found out that the resulting pressure for the free molecular regime in which Knudsen number is greater than 10 is approximately 0.013 Pa.

The present work aims to analyze the flow and heat characteristics for the slip flow regime in the annulus region between two horizontal concentric cylinders in which the inner cylinder is attached to a solid fin using two-dimensional computational model.

3. Numerical Solution

A finite volume analysis is utilized as a method of solution for the problem under investigation. The SIMPLE algorithm adopted from Versteeg and Malalasekera [27] and Patankar and Spalding [28] is used to calculate the pressure field. A hybrid second order accuracy scheme of central and upwind difference is used to differentiate the convective terms. The discretized equations are solved and the criterion of convergence is assumed when the maximum of the normalized absolute residual across all nodes is less than 10^{-6}.

4. Grid Independency

Fig. 2 shows a sample of the grid of the domain of the problem. It consists of a simple two-dimensional mesh. For the initial mesh, the grid step sizes are increasing in the radial and azimuthal directions with expansion factors of 1.06 and 1.15, respectively and then the adaptive grid technique is used. The chosen expansion factors are selected in order to capture the steep gradients near the solid-fluid interface and to better resolve the changes in the boundary layer. A systematic change was adopted to arrive at used factors as we have started with a uniform mesh and varied these parameters to a suitable level. Further change in these parameters will have no impact on the solution. In the adaptive grid technique, the velocity gradients near the walls are calculated and additional cells were added in order to reduce the velocity gradients below a certain value. A grid independency test is carried out by monitoring the heat transfer per unit length, and many solutions were obtained for different numbers of grid nodes. It was observable that there is a certain number of nodes in which any further increase of the nodes will not change the value if the heat transfer per unit length as can be seen in Table.1. It is clear from the table that the solution is mesh-independent for a grid of 80×480 in the radial and azimuthal directions, respectively. This grid size is used for all cases of *Ra*.

Table 1: Grid independent study

Mesh	Q(W/m)	Percentage change compared to 80x480 mesh
40×360	44.924	2.0196
60×360	44.2394	0.46493
80×360	43.989	-0.10365
80×480	44.0347	0

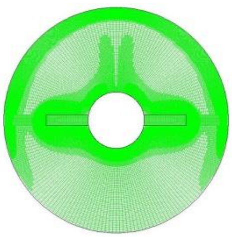

Figure 2 Adaptive grid system technique used in the simulations

5. Code Verification

To verify the numerical code, results of the current code are tested and compared with the results obtained by [10]. Fig. 3 illustrates a comparison between k_r obtained by the current code and that obtained by [10]; it should be noted that K_{eff} represents the thermal conductivity of the fluid, the verification utilized $Ra = 5.3\times10^4$. The comparison shows an error of less than 1.3 %. Also, Kiwan and Khodier [29] presented other validation studies using the same code for an open-ended channel partially filled with an isotropic porous medium.

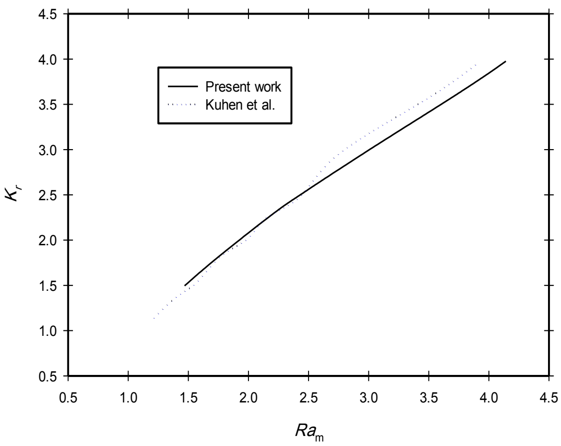

Figure 3. Comparison between current data and Kuhen et al. data

6. Results and Discussion

Fig 4(a) shows the velocity stream function contours. Knudsen number values of 0.01, 0.03, 0.05, 0.08 and 0.1 are considered. It is obvious from the graph that as Knudsen number increases, the center of rotation moves upward in the counter clockwise direction, this can be justified because of the rarefaction effect; the increase in rarefaction will increase the slip flow at the walls. Also, by increasing the mean free path, the interaction between molecules will be reduced and thus lower resulting velocities are obtained.

Fig. 4(b) illustrates the temperature contours (Isotherms) for different Knudsen numbers. The contours show that for all cases, the lower part of the annuli represents a case of a dominant conduction mode of heat transfer while in the upper part of the annulus; the convection mode is becoming dominant. One can see that for the lower part of the annulus that is in the region of 0 and 30 degrees counter clockwise, the flow is thermally stable while in the region between 70 and 90 degrees counter clockwise, the flow becomes unstable due to the buoyancy effects. It is also clear from the graph that as Knudsen number increases then the distortion and mixing of the flow decreases and consequently the heat transfer decreases.

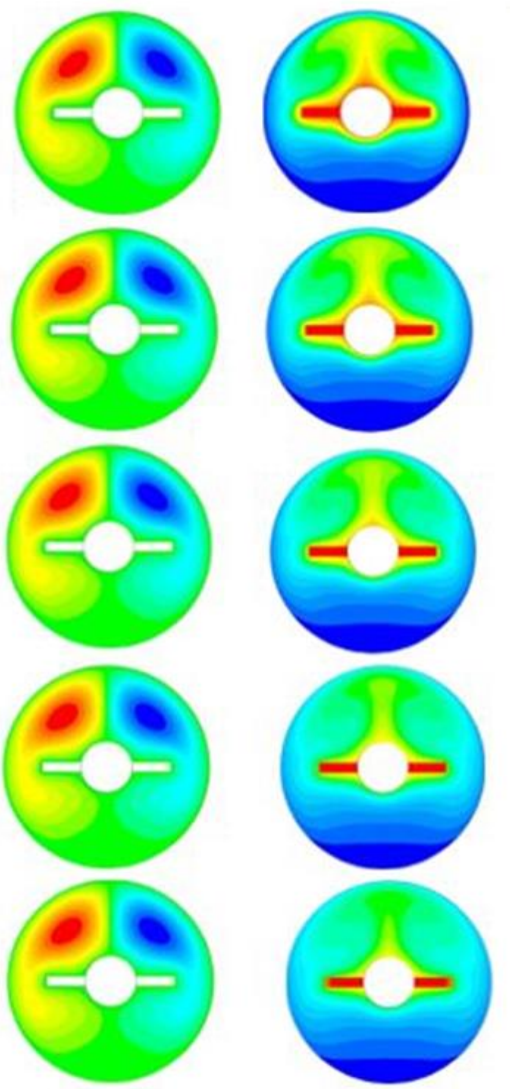

(a) (b)

Figure 4. (a) Streamlines [θ=0o], (b) Isotherms [θ=0o]

In Fig. 5, the temperature contours (isotherms) and the velocity stream function contours are plotted for different fin inclination angles. The graph shows for inclination angle θ=90^{o}, there are two symmetric circulation loops. As the fin inclination angle decreases, one of these loops is shifting upward while the other one is shifting downward. This shift increases the resistance to the flow. The maximum resistance is achieved for the case of angle θ=0^{o}. This case represents the minimum circulation velocity and the maximum thermal boundary layer thickness along the upper faces of the fins and the inner cylinder

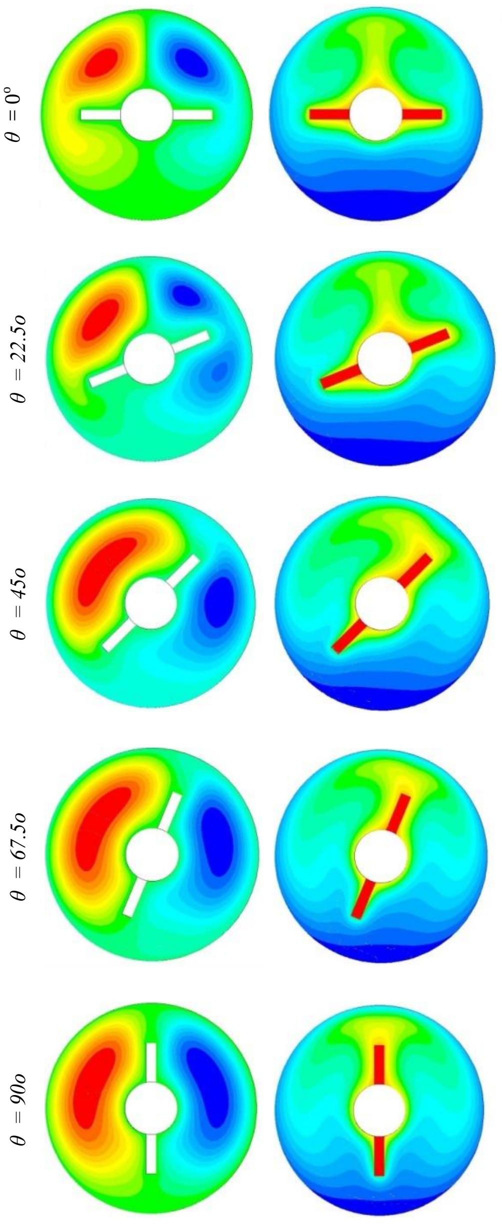

(a) (b)

Figure 5. (a) Streamlines for various fin inclination angles, (b) Isotherms for various fin inclination angles

Shown in Fig. 6, the variation of the local heat transfer coefficient *h* with the angle φ for both cases of the slip and no slip flows whether the inner cylinder is attached to a fin or not. The graph shows that by attaching a fin then the local heat transfer is higher than the case of the no fin for both of the slip and no-slip flows. Also, the graph shows that the slip flow will reduce the local heat transfer coefficient compared to the no slip flow case. Moreover, the graph illustrates that the local heat transfer coefficient will increase by increasing the value of angle φ for both of the slip and the no slip flows whether the inner cylinder is attached to a fin or not.

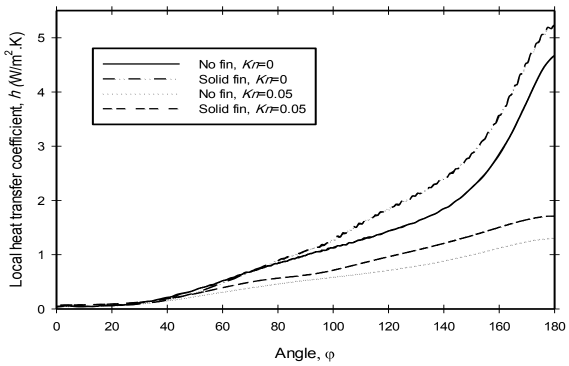

Figure 6. Variation of the local heat transfer coefficient for the cases of no fins and with fins for continuum and rarefied flows along the angle (φ).

Fig. 7 demonstrates the dimensionless vertical velocity V_y variations with the dimensionless radial distance r^* for different values of Knudsen numbers that cover the slip flow regime.it is obvious from the graph that the higher the Knudsen number, the lower dimensionless vertical velocity for cases where r^* is less than one. The opposite will occur for the cases where r* is higher than unity, the higher Knudsen number will result in lower dimensionless vertical velocity. This will result in less heat transfer and consequently lower Nusselt number.

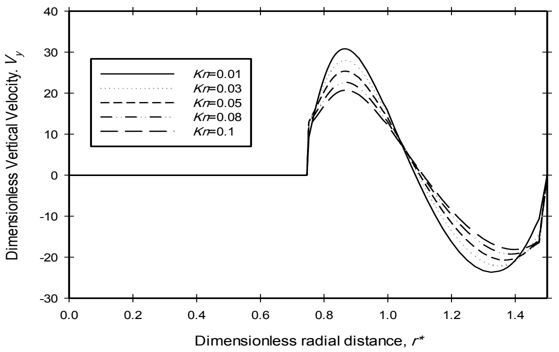

Figure 7. Variation of the dimensionless vertical velocity (V_y) with the dimensionless radial distance (r^*) for different Knudsen numbers

In Fig. 8, the dimensionless temperature distribution T^* is plotted against the dimensionless radial distance r^*, the graph shows that as Knudsen number increases then the temperature jump at the outer cylinder surface will increase.

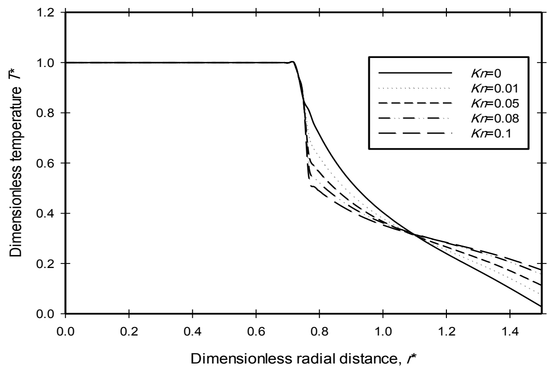

Figure 8 Variation of the dimensionless temperature (T^*) with the dimensionless radial distance (r^*) for different Knudsen numbers

The variation of the average Nusselt number with Rayleigh number for different Knudsen numbers is shown in Fig. 9. The graph illustrates that as Rayleigh number increases then the average Nusselt number is increasing for the same Knudsen number. Also, the graph shows that as Knudsen number increases, the average Nusselt number decreases for the same Rayleigh number. In addition, the graph shows that for low Rayleigh numbers, the dominant mode of heat transfer is conduction while for higher Rayleigh numbers, the convection heat transfer will dominate.

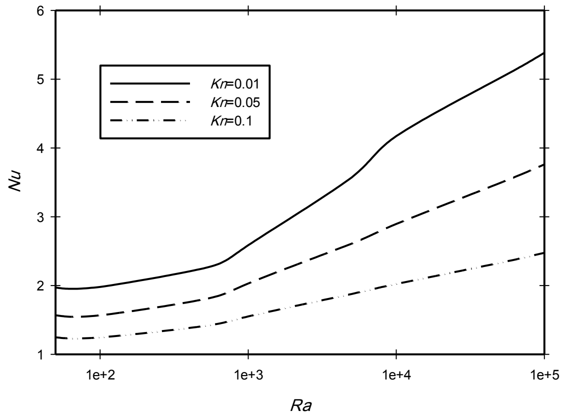

Figure 9. Variation of Nusselt number (Nu) with Rayleigh number (Ra) for different Knudsen numbers

Variations of the average Nusselt number with the conductivity ratio of the fin for different values of Knudsen number are plotted in Fig. 10. The graph shows that by increasing Knudsen number, then the average Nusselt number will decrease for the same conductivity ratio. In addition, it is obvious that as the conductivity ratio increases, the average Nusselt number increases up to a certain limit beyond which a further increase in the conductivity ratio has no significant effect on the average Nusselt number.

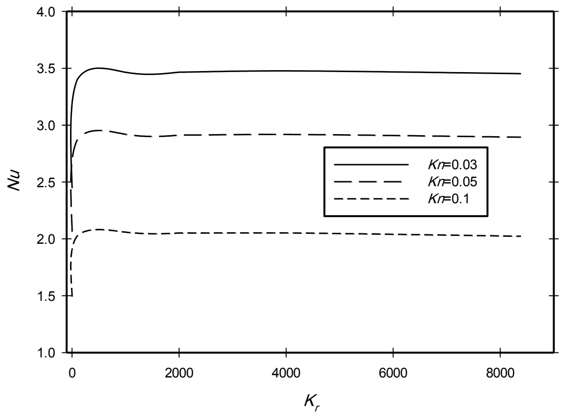

Figure 10. Variation of Nusselt number (Nu) with the conductivity ratio (Kr) for different Knudsen numbers

Figure 11 shows the average Nusselt number variations with the fin inclination angle, the graph shows that for the no slip and slip flows and for the region where θ is in the range of 0-20 degrees, the average Nusselt number is almost constant. Beyond this range, the higher the fin inclination angle, the higher the average Nusselt number. The graph also shows that there is almost an order of magnitude difference in the value of Nusselt number between the continuum versus the slip flow case.

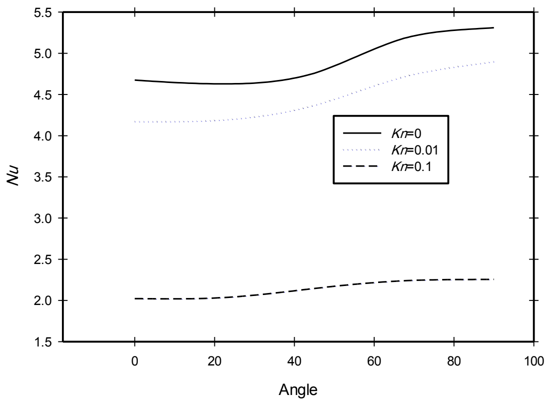

Figure 11 Variation of Nusselt number (*Nu*) with the fin inclination angle (θ) for different Knudsen numbers

7. Conclusions

A steady, two-dimensional analysis of low-pressure gaseous laminar flow in the annulus region between two concentric cylinders in which the inner cylinder is attached to a solid fin is carried out. This type of flow has a wide variety of applications such as the receiver of the parabolic trough collectors and the evacuated tube collectors. Rarefaction effects on both flow and heat characteristics of such flows are investigated. It is found that as Knudsen number increases, the slip velocity and the temperature jump at the boundaries will increase. In addition, it is found that as Knudsen number increases, the average Nusselt number will decrease. Moreover, it is found that by attaching a fin to the inner cylinder for such flows, average Nusselt number will increase for the same Knudsen number. Finally, It is concluded that no-slip (Continuum) flows have better heat transfer characteristics (measured by the average Nusselt number) than slip flows.

References

[1] Karniadakis G, Beskok A, and Aluru N. *Microflows and Nanoflows*. Springer; 2005.

[2] Bird G A. *Molecular Gas Dynamics and the Direct Simulation of Gas Flows*. Oxford Univ: Press Oxford; 1994.

[3] Patnode AM. *Simulation and Performance Evaluation of Parabolic Trough Solar Power Plants*. Master thesis. University of Wisconsin-Madison: College of Engineering; 2006.

[4] Schaaf S, Chambre P. *Flow of Rarefied Gases*. Princeton Univ: Press Princeton; 1961.

[5] Cercignani S, Lampis M. *Rarefied gas dynamics*. New York: Academic Press; 1974.

[6] N.A. Gatsonis, W. Al-Kouz, R.E. Chamberlin, ''Investigation of rarefied supersonic flows into rectangular nanochannels using a three-dimensional direct simulation Monte Carlo method'' . Physics of Fluids. Vol. 22, No. 1-16, 2010.

[7] S. Kiwan, M.A. Al-Nimr, ''Flow and heat transfer over a stretched microsurface''. ASME transaction J. Heat Transfer, Vol. 28, No. 6, 2009, 1-8.

[8] S. Kiwan and M.A. Al-Nimr, ''Investigation into the similarity for boundary layer flows in micro-systems''. ASME transaction; J. Heat Transfer, Vol. 132, No. 4, 2010, 1-9.

[9] W. Al-Kouz, M. Sari, S. Kiwan and A. Alkhalidi, ''Rarefied flow and heat transfer characteristics over a vertical stretched surface''. Journal of Advances in Mechanical Engineering. Vol 8(8), 2016, 1-13.

[10] T.H. Kuehn, R.J. Goldstein, ''An experimental and theoretical study of natural convection in the annulus between horizontal concentric cylinders''. J. Fluid Mech, Vol. 74, 1976, 695-719.

[11] T.H. Kuehn, R.J. Goldstein., ''Correlating equations for natural convection heat transfer between horizontal circular cylinders''. Int J. Heat MassTransfer., Vol. 19, 1976, 1127-1134.

[12] G.D. Raithby, K.G. T. Hollands, ''A general method of obtaining approximate solutions to laminar and turbulent free convection problems". Advances in Heat Transfer, No. 11, 1975, 265-315.

[13] L.R. Mack, E.H. Bishop, ''Natural convection between horizontal concentric cylinders for low Rayleigh numbers''. Q.J. Mech. Appl. Math. XXI, 1968, 223-241.

[14] A. El-Sherbiny, ''Natural convection in air layers between horizontal concentric isothermal cylinders''. Alexandria Engineering Journal, Vol. 43, No. 3, 2004, 297-311.

[15] M.A. Sheremet, ''Laminar natural convection in an inclined cylindrical enclosure having finite thickness Walls''. International Journal of Heat and Mass Transfer, Vol. 55, 2012, 3582–3600.

[16] A. Bouras, M. Djezzar, C. Ghernoug, ''Numerical simulation of natural convection between two elliptical cylinders: Influence of Rayleigh number and Prandtl number". Energy Procedia, Vol. 36, 2013, 788-797.

[17] S. Kiwan, O. Zeitoun, ''Natural convection in a horizontal cylindrical annulus using porous fins''. International Journal of Numerical Methods for Heat & Fluid flow, Vol. 18, 2008, 618-634.

[18] A. Bouras, M. Djezzar, H. Naji, C. Ghernoug. ''Numerical computation of double-diffusive natural convection flow within an elliptic-shape enclosures''. International Communications in Heat and Mass Transfer, Vol. 57, 2014, 183-192.

[19] M. Cianfrini, M. Corcione, A. Quintino, ''Natural convection heat transfer of nanofluids in annular spaces between horizontal concentric cylinders''. Applied Thermal Engineerin, Vol. 31, 2011, 4055-4063.

[20] W. Chmaissem, S. Suh, M. Daguenet, ''Numerical study of the Boussinesq model of natural convection in an annular space: Having a horizontal axis bounded by circular and elliptical isothermal cylinders''. Applied Thermal Engineering, Vol. 22, 2002, 1013-1025.

[21] R. Padilla, G. Demirkaya, D. Goswami, E. Stefankos, ''Heat transfer analysis of parabolic trough solar receiver''. Applied Energy, Vol. 88, 2011, 5079-5110.

[22] W. Al-Kouz, A. Alshare, A. Alkhalidi, S. Kiwan, ''Two dimensional analysis of low pressure flows in the annulus region between two concentric cylinders''. SpringerPlus, 2016, 5-529

[23] D. Lockerby, J. Reese, R. Barber, ''Velocity boundary condition at solid wall in rarefied gas calculations, Physical Review E''. Vol. 70, No. 1, 2004, 017303.

[24] Stéphane Colin, *''Heat Transfer and Fluid Flow in Minichannels and microchannels: Single-phase gas flow in microchannels''.* Elsevier Ltd 2006.

[25] H. Price, E. Lupfert, D. Kearney, E. Zarza, G. Cohen, R. Gee, ''Advances in parabolic trough solar power technology''. J Solar Energy Eng Tran ASME, Vol. 124, No.2, 2002, 109-25.

[26] Thomas JR, "*Heat conduction in partial vacuum''.* Virginia Polytechnic Institute and State University. Blacksburg, Virginia: U.S. Department of energy, EM-78-C-04-5367, 1979.

[27] H. Versteeg, W. Malalasekera, *''An Introduction to Computational Fluid Dynamics: The Finite Volume Method*''. Prentice-Hall, Essex, 1995.

[28] S.V. Patankar, D. B. Spalding, ''A calculation procedure for heat, mass and momentum transfer in three-dimensional parabolic flows''. Int. J. of Heat and Mass Transfer, Vol. 15, No. 10, 1972, 1787-1806.

[29] S. Kiwan, M. Khodeir, ''Natural convection heat transfer in an open- ended inclined channel partially filled with porous media''. J. Heat Transfer Engineering, Vol. 29, 2008, 67-75.

JJMIE

Volume 10 Number 4, December.2016
ISSN 1995-6665
Pages 263-270

Jordan Journal of Mechanical and Industrial Engineering

Investigation of the Flowability and the Thermal Behavior of Sand /Basalt-Mixture in Moving Bed Heat Exchanger (MBHX) as Heat Transfer Medium for Concentrating Solar Tower Plants

Louy Qoaider [a *], Suhil Kiwan [b], Qahtan Thabit [a]

[a] German Jordanian University, School of Natural Resources Engineering and Management, Energy Engineering Department, P.O. Box 35247, Amman 11180 Jordan, Phone: +962 (06) 429 4444
[b] Jordan University of Science and Technology, Mechanical Engineering Department, P.O. Box 3030, Irbid-Jordan

Received August, 27, 2016 Accepted October, 20, 2016

Abstract

The present study investigates experimentally heat recovery from particle-based Thermal Energy Storage (TES) by using different bulk material (Sand, Basalt, and Mixture). A newly developed Moving Bed Heat Exchanger (MBHX) was used for this purpose. The present work focuses on solar thermal power plants applications to find economic and efficient heat transfer and heat storage medium. In the experimental investigations, the performance assessment of a prototype was carried out with a detailed look on the granular flow behavior as well as its overall thermal efficiency. The tested heat transfer mediums are only Sand, only Basalt and a Sand/Basalt mixture. The results showed that the mixture has best thermal performance among other tested materials within the heat exchanger. The effectiveness of the MBHX and the overall heat transfer coefficients of the heat exchanger are measured and documented. The test results showed that the MBHX effectiveness was improved when using the Sand/Basalt mixture by 45.5% and 33.3% than using only Sand and Basalt as heat transfer fluid, respectively. Moreover, the powder flow test results show that the mixture has a better flowability than having only Sand or Basalt.

Keywords: *Thermal Energy Storage (TES), Moving Bed Heat Exchanger (MBHX), Effectiveness.*

Nomenclature

A_s	Surface area	m^2
c	heat capacity ratio	-
c_p	specific heat capacity	J/kg.K
D_i	inner diameter of tube	m
D_o	outer diameter of tube	m
h	convection heat transfer coefficient	$W/m^2.K$
h_i	inner convection heat transfer coefficient	$W/m^2.K$
h_o	outer convection heat transfer coefficient	$W/m^2.K$
K	thermal conductivity	W/m.K
L	length of tube	m
N	number of tube bundles in the MBHX	-
Pr	Prandlt number	-
Q	rate of heat transfer	W
St,h	horizontal distance	mm
St,v	vertical distance	mm
T	Temperature	K
t_c	contact time	S
V	Velocity	m/s
ε	effectiveness of heat exchanger	-

1. Introduction

Concentrating Solar Power technologies (CSP) have a considerable potential for implementation in sunny regions and have relatively good conversion efficiency from solar radiation to electrical energy. CSP technologies generate electricity by concentrating the direct solar radiation on to a small absorber area, where a Heat Transfer Fluid (HTF) is heated up and this energy is ultimately transferred to the steam. Electricity is then generated by an electric generator, which is driven by a steam turbine with the efficiency limited by the Carnot cycle.

The ease of integration Thermal Energy Storage (TES) [1; 2] makes Concentrating Solar Power (CSP) dispatchable and unique among all other renewable energy-generating alternatives. A TES system that offers efficient heat energy storage can be considered an important intermediate step for on-demand electricity generation. Depending on the size of the TES system, it is able to mitigate the short load fluctuations and shift or

* Corresponding author e-mail: louy.qoaider@gju.edu.jo

extend the energy supply. Thermal Energy Storage (TES) is one of the few energy storage technologies that have proven to be an economically feasible large-scale storage solution. Thermal Energy Storage (TES) is a technology that stocks thermal energy by heating or cooling a storage medium so that the stored energy can be used later for heating and cooling applications and power generation.

CSP with TES presents advantages if it supplies electricity at times of greatest need, which generally has the highest electricity tariff [3; 4]. Furthermore, TES is a key technology for solar thermal energy utilization and the improvement of the cycle operation efficiency. Using an energy storage system in a solar thermal power plant has many advantages, such as obtaining higher annual solar contribution, reduction of part-load operation, power management and buffer storage to improve the plant dispatchability [5]. Three fundamental types of thermal energy storage processes are commonly presented in the literature; sensible, latent, and thermochemical. Many different mediums are available within each type. With sensible heat storage, energy is stored by changing the temperature of a material. Most sensible heat systems employ water, rocks earth, or ceramic bricks as the thermal storage material and water, air, or possibly oil as the heat transfer fluid. Sand is among the most promising materials that could be used for sensible energy storage. It has been very attractive recently for its availability and low cost [6; 7].

Thermal Energy Storage (TES) based on a flowable granular material made of ceramics or natural stones allows for a load following operation of a central receiver solar power plant at high process temperatures (> 600°C). In such a system, the granular mass is used both as heat transfer and storage medium in a closed cycle. The particles can be heated either directly (see Fig. 1) in a direct absorption receiver [8] or indirectly by air coming from a volumetric air receiver [9]. Such a system depends on a heat exchanger to generate steam from a solar heated particle stream. The Moving Bed Heat Exchanger (MBHX) is a promising technology option for this component. MBHX offers low parasitic loads, a good part load behavior, a little need for maintenance, a compact design and low financial investment and operation expenses [10]. The purpose of the present paper is to evaluate the performance of moving bed heat exchanger (MBHX) with innovative solid particles of Sand & Basalt mixture where the particles working as a heat transfer medium and a thermal heat storage. Sand, Basalt and their even mixture (Sand/Basalt) are tested as a heat transfer fluids by using an experimental Moving Bed Heat Exchanger (MBHX) that is developed and tested at the Institute for Thermodynamics of the German Aerospace Center (DLR). The aim of the present research paper is to investigate the flowability and the thermal performance of the three potential HTFs. To achieve this goal, several experiments are conducted: (1) measuring the flowability of the materials, (2) measuring the flow interaction between the material and the designed MBHX using PIV technique, (3) measuring thermal properties of the materials and (4) measuring the thermal performance of the MBHX in real flow case using the selected materials.

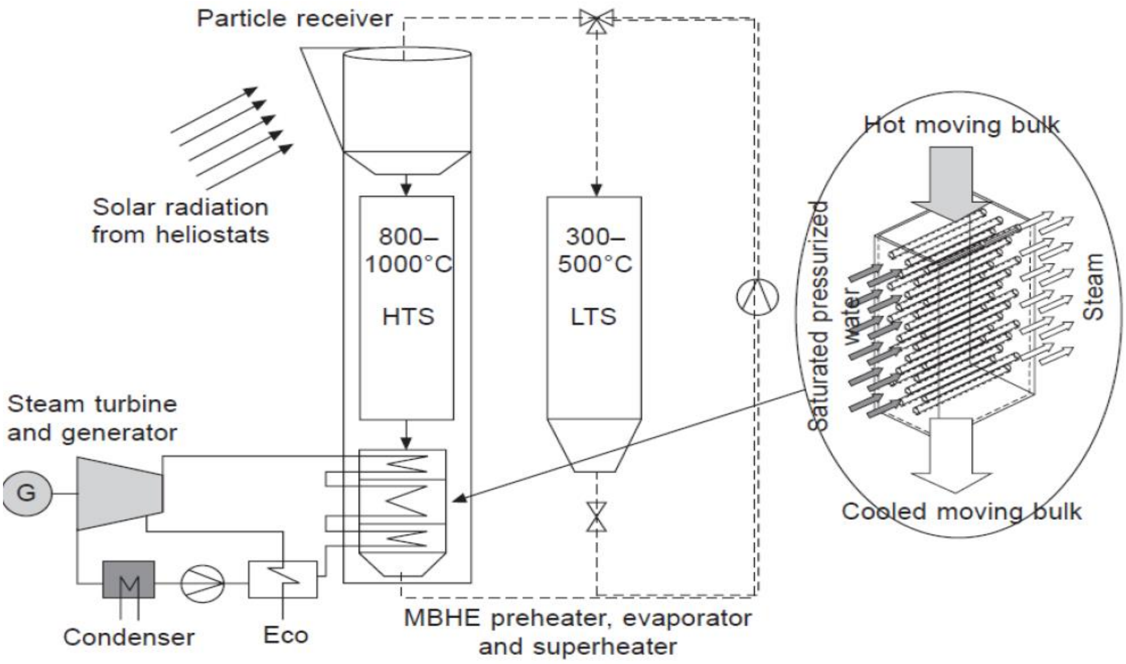

Fig. 1. Central receiver solar power plant with particle storage and integrated moving bed heat exchanger

2. Analysis of Tested Materials and Pre-Experiment

2.1. Rheological Properties

As mentioned earlier, three different material combinations are tested as working fluid in the systems under consideration; only sand, only Basalt and a mixture of 50% Sand and 50% Basalt. At the first stage, the material flow behavior was tested to check its suitability to circulate in the system, in general, and in the heat exchanger in particular. Material with high "flowability" is desired while cohesive material is to be avoided especially when the material flow is driven by gravity, which is the case in the MBHX. The "flowability" of the bulk material inside the MBHX has its direct effect on the heat transfer process between the bulk material and the walls of the tube bundles of the heat exchanger since it controls the speed of the solid material inside the heat exchanger. Thus, it affects the design of the tube bundle distribution in the MBHX.

The rheological properties of bulk material determine its flow behavior. The ring shear cell apparatus, which is known as "Powder Flow Tester", is used to measure both major principal consolidation and unconfined failure stresses to obtain knowledge about the nature of flowability of the materials. The standard classification of powder flowability uses the flow factor index ffc, as shown below:

ffc<1	Non flowing
1<ffc<2	Very cohesive
2<ffc<4	Cohesive
4<ffc<10	Easy flowing
10<ffc	Free flowing

The data obtained are demonstrated in Fig. 2, which classifies the "flowability" of bulk materials. As shown in Fig. 2, Basalt has the lowest "flowability" while Sand and Basalt mixture has the highest "flowability". Furthermore, according to the flowability classification regions in Fig. 2, Basalt suffers from cohesiveness and thus is not favorable in the MBHX. However, it can be noticed that the presence of Basalt in the sand improves the flowability of the sand. Whereas, sand and Mixture flowability lies in a sector where ffc >10, the flowability of Basalt fluctuates between ffc =2 and ffc=4. Accordingly, Basalt has the least flowability.

2.2. Design Concept of the MBHX

The MBHX conceptual design is based on a heat exchanger with a staggered tube bundle arrangement operated in cross-counter flow configuration. A CSP-adapted design requires a specific tube bundle arrangement, which strongly depends on the rheological properties of promising bulk material. The design procedure is described in [10]. For the thermal characterization experiment, a stainless steel MBHX prototype has been constructed in DLR laboratories, integrated with a fully transparent acrylic glass mock-up for flow investigations. The acrylic glass side is chosen so that PIV measurements can be conducted via this transparent side. A prototype with a certain distribution of tubes was used, as shown in Fig. 3. Baumann *et al.* [10 to 12] used two prototypes of different distribution. The geometric data of the test configurations of mock-ups can be found in Table 1.

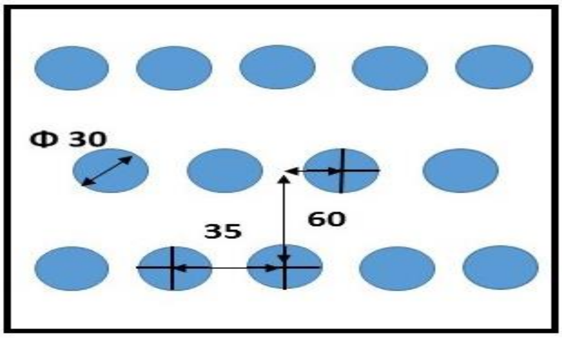

Fig. 3. Configurations of the MBHX tube bundle used in the acrylic glass model for PIV measurements

Table 1. Geometric details of the two designs of MBHX

Experimental purpose (PIV)	Tube bundle
Ro[mm]	30
Number of tubes	45
A [m^2]	-
St,v [mm]	60
St,h [mm]	35

Therein, *A* is the effective heat transfer area and *Ro is* outer radius of the tube, S_v and S_h are the vertical and horizontal tube pitch, respectively [10 to 12].

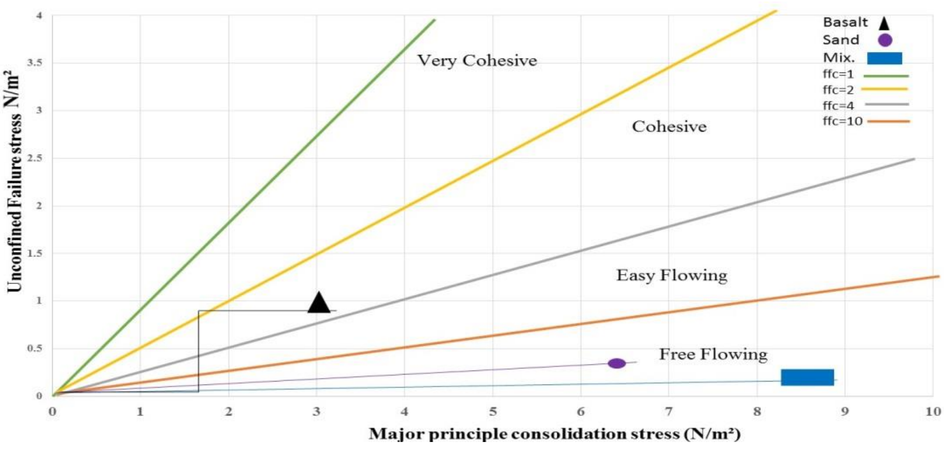

Fig. 2. Powder flow function of Sand, Basalt, and Mixture [12]

To characterize the flow behavior of the granular medium around the acrylic glass tube bundle, Particle Image Velocity (PIV) is applied. This measurement technique has been successfully applied to granular flows before (e.g., in [10 to 12]). The set-up includes a high-speed camera, a halogen bulb lamp for illumination of the plane of interest and an external computer for data processing. The set-up is illustrated in Fig. 4. Details and specifications of equipment used are available in Reference [10 to 12].

The mock up was filled with sand (Table 2) and the velocity measurement inside the mock-up of tube bundle was conducted using the PIV measurements as shown in Fig. 5. The captured pictures were analyzed by using two software packages (Image J and Matlab). The results are shown in Fig. 6. It was found that the velocity of the particles of sand was 4 mm/s. Fig. 5 and Fig. 6 show the formation of a stagnation area and void zones at the top and at the bottom of each tube, respectively. In the stagnant zone, which often has a triangular-like shape, the particles are almost motionless. The stagnant zone is a thermally insulating area in comparison to those regions in which particles are flowing. It should be noted that the same experiment was conducted by Baumann *et al.* [11; 12] before and the same phenomena (stagnation zones and voids) was observed.

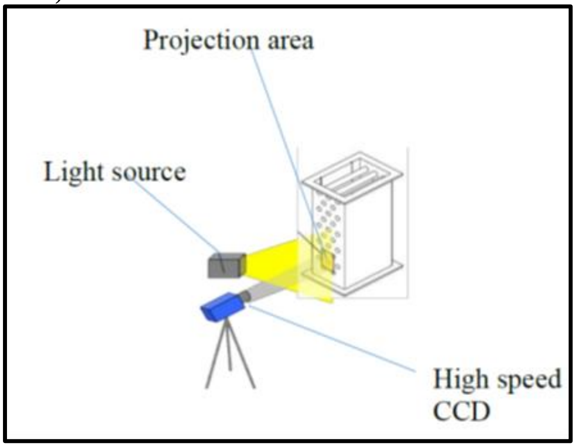

Fig. 4. Simplified representation of the PIV measurement setup

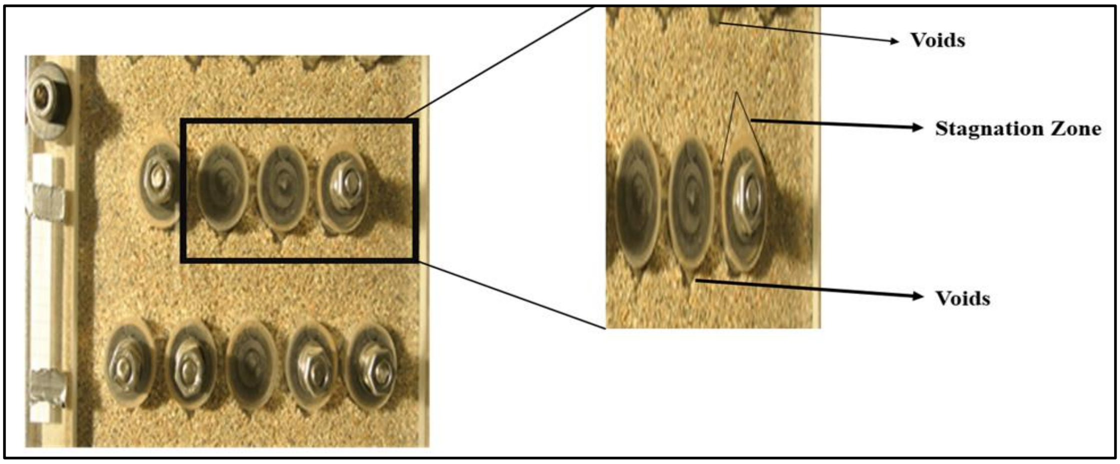

Fig. 5. Stagnation zones and voids at the upper and lower parts of tube

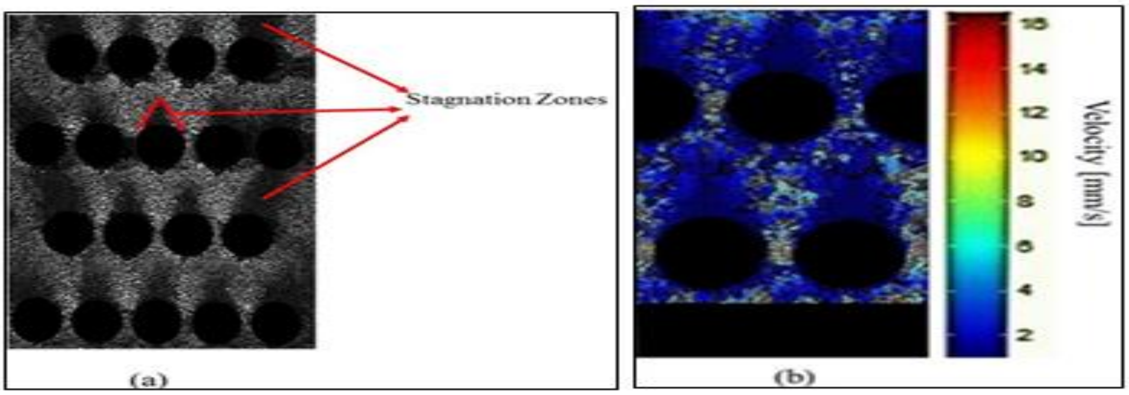

Figure 6. pictures' analysis of the PIV test. (a) Image J analysis. (b) Matlab analysis

The velocity of sand inside the mock-up was measured to be 4mm/s. This reassure the results obtained by Baumann, who investigated the performance of the MBHX by using two different arrangements of the tube bundles. One of these arrangements with S_h = 40 mm and the other one with S_h = 60 mm, with inlet velocities ranging between 0.3 mm/s – 3mm/s [10 to 12] . Baumann found that the MBHX with a narrower horizontal distance has a higher velocity then the heat transfer process increase according to equations (1) and (2) [12 and 17]. Therefore, in this mock-up, the horizontal distance was decreased by 5mm, as shown in Fig. 3, and the inlet velocity increased to 4 mm/s. These observations indicate that the extension of the stagnant zone is affected by the tube bundle arrangement [10 and 12]. The stagnant zone is a thermally insulating area in comparison to those regions in which particles are flowing [13 to 16].

Table 2. Sand properties

Material	Particles Diameter [mm]	Density [Kg/m^3]	Form factor fp
Sand	0.8$\pm$ 0.18	1456.8	1.15

$$h_o = \frac{2\sqrt{(Kcp\rho)so}}{\sqrt{\pi}\sqrt{t_c}} \quad (1)$$

$$t_c = \frac{S_R}{V} \quad (2)$$

where, t_c it is the contact time and (h) is the convection heat transfer coefficient. Accordingly, the relationship between (h) and the reciprocal value of (tc) in the model indicates that, the shorter the contact time the better will be the heat transfer process. Therefore, increasing velocity means that the heat transfer also increases.

3. Thermal performance Experimental Setup

For the thermal performance assessment, a test rig was constructed at the Institute of Technical Thermodynamics at DLR. The test rig consists of a tube chain conveyor, a heated storage bin and a replaceable MBHX test device. Twenty-four heating plates are inserted inside the storage bin. The heating plates inside the storage bin can heat up the bulk up to approximately 500°C depending on the flow rate. The maximum heating power is 38 kW. The centerpiece of the lab is the moving bed heat exchanger. In the MBHX, the hot particles are driven gravitationally through the shell space, while, a cold mineral thermal oil is flowing inside the heat exchanger pipes using a pump, as shown in Fig. 7. The heat is then transferred from the bulk material to the cold fluid. The cooled bed –bulk material- is transported using a conveyor device back into the storage tank where it is heated again.

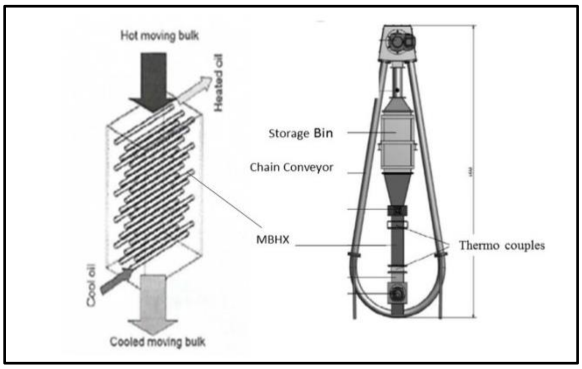

Fig. 7. Components of the Experimental setup and the MBHX [10]

For the thermal characterization experiment, a stainless steel prototype of MBHX has been constructed at the Institute of Technical Thermodynamics at DLR. The geometric properties of the MBHX are listed in Table 3.

Table 3. Geometric properties of the heat exchanger

Parameters	Stainless steel prototype
Outer Diameter [mm]	26.9
Number of Tubes	25
Area [m^2]	0.61
Horizontal distance $S_{,h}$ [mm]	23.3
Vertical distance $S_{,v}$ [mm]	31.1

3.1. Bulk-Side System Components

In the storage container, 24 electric heating panels are arranged in parallel. The heating plates reach a maximum surface temperature of about 500 °C to heat up the bulk material flowing between the plates. The temperatures of these plates are controlled by controlling the electric power supplied to each plate heater. Depending on the flow rate the outlet temperatures of the bulk material reaches up to about 400 °C. There are 25 thermocouples fixed to measure the temperature of the bulk material before and after crossing the heat exchanger, as shown in Fig. 8. A special feedback control system is designed for this purpose using a software installed on a computer that control the heaters temperature to heat the bulk material to the desired value.

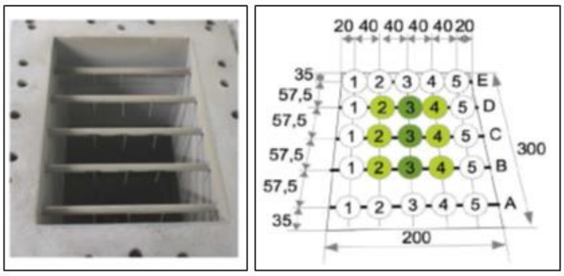

Fig. 8. Grid for thermocouples locations at the inlet and outlet of MBHX shell [10 to 12]

In this experiment, the three different materials of interest are used to evaluate their thermal performance in the MBHX. The physical properties of selected materials used in the experiment are shown in Table 4.

Table 4. Properties of tested materials

Material	Diameter [mm]	Density [kg/m3]	Form Factor (-)	c_p [kJ/Kg K]	K [w/m k]	Melting point [°C]
Quartz Sand	0.8±0.18	1456.8	1.15	0.83	1.79	1700
Basalt	1.77± 0.56	1422	1.21	0.84	2.11	1200
Mix. (Basalt/Sand)	0.6±0.4	1439.4	1.18	0.835	1.95	1450

3.2. Liquid-Side System Components

This side includes all components related to the flowing of the fluid. The working fluid used is the mineral thermal oil "Mobiltherm 603". In unpressurized operation, its operating temperature may reach maximum of 300°C. Compared to water/steam as the working medium, the thermal oil allows single-phase operation and hence easier for energy accounting, simpler for assessment of heat transfer coefficient and the possibility to operate under atmospheric pressure. The thermal oil operates in two cycles: heating by the heat exchanger (by the moving bed), and cooling by an auxiliary external cooler down to 200 °C. At the inlet and outlet of the oil tube, two redundant resistance thermometers are mounted.

4. 4. Results and Analysis

Thermal test was conducted for each of the selected material (Sand, Basalt and Mixture). The rate of heat transfer between the bulk material and oil inside the tubes of the heat exchanger could be found from the equation:

$$\dot{Q} = \dot{m}\, c_p \Delta T \tag{3}$$

The relation above can be applied to both working mediums: oil or solid particles. The outer surface of the heat exchanger is perfectly insulated. Therefore, the thermal losses to the surrounding are negligible (approx. 1%) [10, 12]. Thus, it can be assumed that the rate of heat transfer from hot medium (bulk material) equals to the rate of heat transfer to cold fluid (oil). The thermal properties of the oil are shown in Table 5. Heat exchangers usually operate for long periods with no change in their operating conditions. Therefore, they can be modeled as steady-flow devices. As such, the mass flow rate of oil remains constant, and the properties such as temperature and velocity at any inlet or outlet remain the same. To calculate the performance of the MBHX with each one of the selected materials, the effectiveness–NTU method was used. This method is based on a dimensionless parameter called the heat transfer effectiveness ε:

$$\varepsilon = \frac{\dot{Q}_{actual}}{\dot{Q}_{max}} = \frac{(\dot{m}c_p)_s (T_{si} - T_{so})}{(\dot{m}c_p)_{min}(T_{si} - T_{fi})} \tag{4}$$

For all experiments conducted $(\dot{m}c_p)_{min} = (\dot{m}c_p)_s$, thus, Eqn. 4 becomes:

$$\varepsilon = \frac{(T_{si} - T_{so})}{(T_{si} - T_{fi})} \tag{5}$$

The MBHX is a shell and tube heat exchanger so the NTU is determined by [18]:

$$NTU = \frac{1}{\sqrt{1+c^2}} \ln\left(\frac{2/\varepsilon - 1 - c - \sqrt{1+c^2}}{2/\varepsilon - 1 - c + \sqrt{1+c^2}}\right) \tag{6}$$

Then overall heat transfer coefficient can be found by [18]:

$$NTU = \frac{UA_s}{(\dot{m}c_p)_{min}} = \frac{UA_s}{(\dot{m}c_p)_s} \tag{7}$$

It is important to specify which of the selected materials (Sand, Basalt, and Mixture) have better performance as a heat transfer and storage medium. The heat transfer surface area, A_s , is calculated as follows:

$$A_s = \pi D_o L N \tag{8}$$

Table 5. Thermal oil properties

Property	c_p [kJ/Kg.K]	K [W/m.k]	υ [m²/s]	ρ [kg/m³]	Μ [kg/m.s]	Pr
Value	2.60	0.12	$1*10^{-6}$	738	0.000744	16.12

The values of the overall heat transfer coefficient for the three tested combinations are calculated and plotted in Fig. 9 and Fig. 10. The results show that the Mixture (Sand and Basalt) has the highest value of U. It can be seen in the figures that the sand/Basalt mixture is the best bulk material among the tested materials to be used in the MBHX as heat transfer and storage medium.

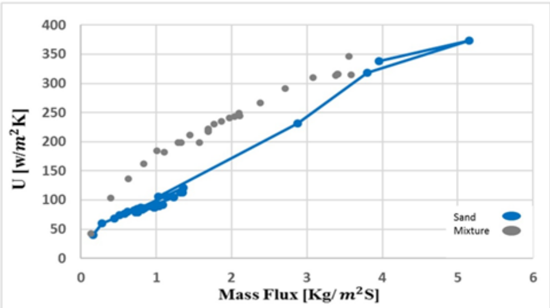

Fig. 9. Overall heat transfer coefficient for Mixture and Sand

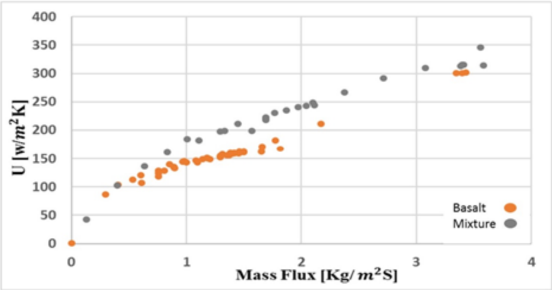

Fig. 10. Overall heat transfer coefficient for Mixture and Basalt

Figures 9 and 10 show clearly that the overall heat transfer coefficient of the mixture is the highest most of the times. For example, Fig. 9 at [2 kg/m^2 S] mass flux the Sand has the highest value of overall heat transfer coefficient. This was 160 [W/m^2 K] for sand and 250 [W/m^2 K] for mixture. The only time that the sand values exceed those of the mixture are observed at value at 5.3 [kg/m^2 S] mass flux where the overall heat transfer coefficient 350, 380 [W/m^2 K] for mixture and sand, respectively, as shown in Fig. 9. This is attributable to the sand inversion phenomenon because the sand is a quartz compound and usually these compounds suffering from inversion at high temperature [12]. This phenomenon was also observed in another research project named "sandstock" in the UAE, where sand was investigated as a storage media "nonflowable" by Diago *et al*. [7]. Multiple tests on different sand samples from the desert of the UAE were conducted. The results show that all the samples are stable up to 1100 ^{o} C [7]. They also noticed some samples experienced color changes after multi-cycling. The color of the sand becomes lighter which may affect the absorptivity of this material.

At [2.3 kg/m^2 S] mass flux in Fig. 10 the overall heat transfer coefficient for mixture was approximately 210 [W/m^2 K] for Basalt and 250 [W/m^2 K] for mixture. In both Figures (9 and 10), the values of the overall heat transfer coefficient increase with the increase in mass flux and this is resulted by the increase of the particles velocity inside heat exchanger. This leads to reduce the contact time of the particles on the wall of the tubes, and thus, increasing the rate of heat transfer process between the wall of the tubes and the bulk material according to equations 1 and 2 mentioned above.

Based on the above test results and observations, it can be concluded that using the Sand/Basal mixture as heat transfer medium shows an improvement in the MBHX effectiveness of 45.5% compared to using only sand and 33.3% compared to using only Basalt.

5. Conclusions

The main objectives of the present study was to investigate the suitability of adding Basalt to the sand to form a bulk material working as a heat transfer and storage medium in Moving Bed Heat Exchanger (MBHX) to be used in CSP Solar Tower plants. PIV measurements are conducted to compare the suitability of using sand as a working fluid in MBHX by measuring the flow behavior around the tube bundles for MBHX. PIV measurements showed that the voids and stagnation zones formed with all materials in the heat exchanger. The rheological properties of Sand, Basalt, and Mixture were tested and documented. The results showed that the Mixture has the best flowability. The thermal performance of the selected material was measured by measuring the effectiveness of the heat exchanger. It is found that using the 50% Basalt and 50% sand mixture in the MBHX results in a higher heat exchanger effectiveness than that when only using Sand or Basalt in MBHX. The improvements were quantified to be 45.5% and 33.3% compared to only sand and only Basalt, respectively.

Acknowledgement

Many thanks are due to the German Aerospace Center (DLR), Institute of Technical Thermodynamics for making the testing and experimental setups available and for conducting the test runs for the present study.

References

[1] Feng-fei Li, Yan-hua Diao, Yao-hua Zhao, Ting-ting Zhu, Jing Liu "Experimental study on the thermal performance of a new type of thermal energy storage based on flat micro-heat pipe array" Energy Conversion and Management Volume 112, 15 March 2016, Pages 395–403.

[2] Saeed Tiari, Songgang Qiu, Mahboobe Mahdavi "Discharging process of a finned heat pipe–assisted thermal energy storage system with high temperature phase change material" Energy Conversion and Management Volume 118, 15 June 2016, Pages 426–437.

[3] Erren Yao, Huanran Wang, igang Wang, Guang Xi ,François Maréchal "Thermo-economic optimization of a combined cooling, heating and power system based on small-scale compressed air energy storage" Energy Conversion and Management Volume 118, 15 June 2016, Pages 377–386.

[4] Stekli J, Irwin L, Pitchumani R. Technical challenges and opportunities for concentrating solar power with thermal energy storage. J Therm Sci Eng Appl 2013;5:021011.

[5] Sattler J., Hoffschmidt B., Günther M., Joemann M: Advanced CSP Teaching Materials. (research report). .(2009)DLR . Germany.

[6] Diago, M., Iniesta, A. C., Delclos, T., Shamim, T., & Calvet, N. Characterization of Desert Sand for its feasible use as Thermal Energy Storage Medium. Energy Procedia, 75, (2015), pages 2113-2118.

[7] Diago, M., Iniesta, A. C., Falcoz, Q., Shamim, T., & Calvet, N. Energy and exergy analysis of a novel gravity-fed solid particle solar receiver. Energy Procedia, 69, (2015). pages 812-821.

[8] Wu W., Gobereit B., Singer Cs., Amsbeck L., Pitz-Paal R.. Direct absorption receivers for high temperatures. Proceedings SolarPACES 2011.

[9] Baumann T., Boura C., Göttsche J., Hoffschmidt B., Schmitz S., Zunft S.. Air-Sand Heat Exchanger: Materials and Flow Properties. Proceedings SolarPACES 2011.

[10] Baumann T., Zunft S. "Experimental Investigation on a Moving Bed Heat Exchanger used for discharge of a particle-based TES for CSP" Eurotherm Seminar #99.

[11] Baumann T., Zunft S. A moving bed heat exchanger for solar thermal power applications: Experimental investigation of granular flow and thermal performance. *Proceedings of 8th World Conference on Experimental heat Transfer, Fluid Mechanics, and Thermodynamics,* 2013.

[12] Baumann T. "hot particle bed for steam generation" doctoral thesis, university of Stuttgart, Stuttgart. (2014).

[13] D. Chehata; R. Zenit; C. R. Wassgren. Dense granular flow around an immersed cylinder. *Physics of Fluids* 15 (6), 2003, pages. 1622-1631.

[14] Takeuchi, H.: Particles Flow Pattern and Local Heat Transfer around Tube in Moving Bed. In: AIChE Journal Vol.42, (1996) pages 1621–1626.

[15] Chehata D. Zenit R., Wassgren C.R. Dense granular flow around an immersed cylinder. Physics of Fluids 15 (6), (2003), pages 1622-1631.

[16] NiegschJ,, Koneke D., Weinspach P.M, "Heat Transfer and flow of bulk solids in a moving bed", *Chemical Engineering and Processing: Process Intensification,* vol. 33, 1994 pages. 73-89.

[17] Baumann T., Zunft S., Tamme R.., "Moving Bed Heat Exchangers for Use with Heat Storage in Concentrating Solar Plants: A Multiphase Model," *Heat Transfer Engineering*, vol. 35, (2013) pages. 224-231.

[18] Cengel Y., Cimbala J.,Turner R.,(2012) "Fundamentals of Thermal-fluid sciences" New York.

JJMIE

Volume 10 Number 4, December.2016
ISSN 1995-6665
Pages 271-277

Jordan Journal of Mechanical and Industrial Engineering

Pad Cratering: Reliability of Assembly Level and Joint Level

Mazin H. Obaidat[a], Osama T. Al Meanazel[a], Mohammad A. Gharaibeh[b] , Hesham A. Almomani[a]

[a] *Industrial Engineering Department, The Hashemite Universit, Zarqa, 13133, Jordan*

[b] *Mechanical Engineering Department, The Hashemite University, Zarqa, 13133, Jordan*

Received July, 24, 2016 *Accepted October, 24, 2016*

Abstract

The emergence of pad cratering has become an increasingly common failure mode for electronics manufacturing due to the transition to lead –free soldering. This phenomenon has become one of the first concerns between manufacturers of electronic equipment devices and other high reliability products who have focused on the failure in testing, handling or transport due to a single overload. Moreover, the number of manufacturers of servers and other electronic products report an early failure by pad cratering in thermal cycling, an occurrence practically unnoticed for SnPb soldered assemblies. There are many factors that affect pad robustness, including but not limited to design (pad size, solder mask, connecting trace, vias), stackup (resin content, glass style), resin material (filler, cure type). Preconditioning also has a significant effect on the long term reliability.

The aim of the present study is to evaluate several laminate materials with respect to pad pull strength, using accepted industry testing methods. Several different design variables, such as resin filler, resin content, fiber glass reinforcement and fabrication process, were studied. Data are presented to show the effects of the above, and to highlight the long term risk associated with latent damage mechanisms.

Keywords:*Epoxy Matrix, Composites, Various Ratios of Particles, TiC*.

1. Introduction

Pad cratering is one of the most problems that occurs in lead-free solder joints, the conversion from using tin-lead solder joint to lead-free soldering has raised many assembly and reliability issues in this field, the most prevalent one is the increased propensity for pad cratering on laminates through lead free soldering process or even right after reflow. The transition to lead free assembly comes to comply with the widely enacted environmental legislation which restricted the use of Hazardous Substances; this directive was adopted by the European Union in 2003 and took effect in 2006.This transition caused high requirement for the use of laminate materials with high glass transition temperature capable of withstanding higher temperature for Printed Wiring Boards (PWBs) and components substrates (Lee, 2006) but the use of these laminate materials are more liable to a mode of failure known as pad cratering (Mattila TT., 2006; Farris A., 2008; Newman, 2008; Vickers N., 2008).

Pad cratering is a crack initiation that occurs during the manufacturing process and propagates during work-service beneath the pad copper connection which occurs within the resin region which consequently leads to ripping off the contact pad from the laminate (the solder ball, the pad and with some ruptured material are lifted together) which is known as cratering (Mukadam M, 2005) as shown in Figure 1. This has been associated with stiffer solder joint and higher flexural modulus and hardness for the laminate included in the lead-free system (Long G, 2007). Furthermore, an increase of laminate hardness may occur in higher processing temperatures (Mukadam M., 2005; Shade F. G., 2006).

Figure 1. Pad cratering Failure mode

The most important characteristic of pad cratering is that cracks occur underneath pad copper and traces. This failure mode is getting an important issue after some stress tests, such as functional test, in-circuit test and mechanical assembly. The separation of the connecting pad from the

* Corresponding author e-mail: mazin@hu.edu.jo.

circuit board leads to electrical failure and other issues that drastically decrease reliability. Therefore, efforts are continuously exerted to study cratering issues for a large number of electronic industries, but the majority of these efforts is completely empirical and based on the explanation of test outcomes and some failure analysis. Researches are still conducting to mitigate pad cratering. Under the conditions of high load-low cycle Jonnalagadda and Qi (Jonnalagadda K, 2005) conducted a study on pad cratering failures while Geng and McAllister (Geng P, 2005) focused on shock loads by one or two drops producing a failure of pad cratering mode. With different laminates the trends and behavior vary strongly, for example, the laminate which used lead-free had lower pad strength than a DICY-crude laminate (Mukadam M, 2005). On the other hand, the effect of temperature on pad strength for some materials was not significant (Ahmad M., 2009; Ahmad M., 2008), while for other materials an increase in temperature has a significant effect on both strengths and fatigue resistance in which both strengths and fatigue resistance decreased significantly (J., 2007; Roggeman B. R. V., 2011; Raghavan, 2010). A study conducted by Yang *et al*. (2010) for pad cratering resistance found that multiple reflows for printed Wiring Boards (PWBs) subjected to different thermal conditions tend to reduce pad strength, also the study had shown the significant impact of peak temperature on the pad strength resistance. Studies for various materials with multiple reflow showed a decrease in pad strength (J., 2007; M. Ahmad J. B., 2009; Roggeman*et al*., 2008; G., 2009). On other hand, a study by Parupalli*et al.* (2008) showed that the effect of multiple reflows did not have a significant effect on pad strength. Other studies showed a significant degradation in fatigue resistance with multiple reflows (J., 2007; Roggeman*et al*., 2008; Godbole G., 2009).

The resin system, filler particles, glass type, pad size and shape are factors make pad cratering a complex problem in which pad cratering is highly dependent on these factors (Roggeman*et al*., 2008; M. Ahmad J. B., 2009)**.** Furthermore, the prediction of pad cratering is much highly difficult due to complex interactions with a multiple degradation mechanismsthat work in conjunction (Roggeman*et al*., 2008). In addition**,** test results showed forstandard FR-4 boards tested for micro-hardness an increasing hardness for the case of as received, post eutectic reflow and post lead free reflow. These results have indicated that an increase in hardness dose not essentially interprets to an increase in the strength but dose inevitably translate to an increase of board brittleness making it more sensitive to pad cratering(Mukadam M, 2005)**.**

Crack initiation occurs for several reasons, these includes that the lead free solder balls are in general more stiffer than tin lead solder balls, so as a result of that they can transfer strain to the Printed Circuit Board (PCB), also the Phenolic-cured PCB materials that in general is used in lead free assemblies are more brittle than the conventional Dicy-cured materials, those two factors coupled together with the high reflow temperature that the lead free assemblies are subjected could lead to higher strain in the assemblies and consequently lead to crack initiation (Ahmad M., 2009.)**.**

The loading condition will also have an impact on the failure mode. Handheld and portable devices are much more likely to experience impact loading from dropping and other handling issues. The high strain rates associated with this type of loading apply more stress onto the connecting pads.

Many test methods have been made to characterize pad cratering and showed that pad performance and position of pads relative to underlying glass bundles are related (Roggeman*et al.*, May 27-30; Roggeman*et al*., 2008; M. Ahmad J. B., 2009; Ahmad M., 2008; D. Xie, May 27-30, 2008).

2. Test Methodology

Testing the resistance to pad cratering can be done as a board level test or joint level test. However, because of some of the inherent differences between two level tests that make correlation of these tests and hence the characterization significantly difficult (Roggeman*et al.*, 2008). In general, engineers rely on joint level testing because they are looking for easier and cheaper way of testing. As described by Roggeman*et al.* (2008), board level tests will give a more complete picture of the reliability of the system in that given scenario, but they are slow, costly and require full assembly and this requires several assemblies to develop good statistics. Some test methods, such as drop, vibration and bend testing, are the most employed methods for board level testing.Table.1 further details the investigation with sample numbers.

Table 1. Materials Characterized (Pad strength benchmarking)

Number	Material	Pad Size	Resin Percentage %	Filled / Unfilled	Process
1	IT 180-1	0.01756 in	0.53	Unfilled	Standard
2	IT 180A-1 B	0.01738 in	0.53	Filled	Advance
3	IT 180-2 B	0.0171 in	0.74	Unfilled	Advance
4	IT 180A-2 B	0.01708 in	0.74	Filled	Advance
5	IT 180-1-	0.01712 in	0.53	Unfilled	Advance
6	IT 180-2	0.01756 in	0.74	Unfilled	Standard
7	IT 180A-1	0.01764 in	0.53	Filled	Standard
8	IT 180A-2	0.01728 in	0.74	Filled	Standard

2.1. Joint Level Test

Joint level test requires only a few pads to gain a good understanding of the strength and fatigue resistance, therefore the number of circuit boards required is very small. In most cases, a single board can be used for several different pad test procedures. Individual solder balls are attached to the pads of interest.A Dagebondtester is used in Hot Bump Pull (HBP) method to pull solder balls attached to Non-Solder Mask Defined (NSMD) pads.At the joint level, a 30° angle fixture using a Hot Bump Pull (HBP) cartridge and a speed of 5 mm/s were used for conducting pad strength as shown in Figure2 below.

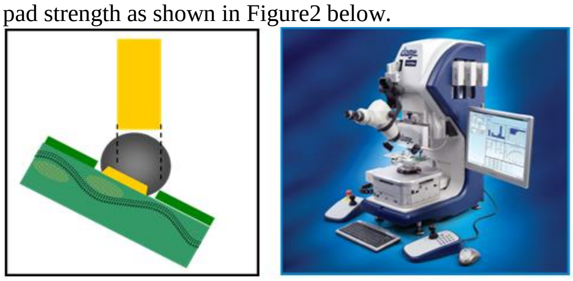

Figure 2. 30° angle at the right and Dage 4000 plus at the left

2.2. Assembly Level Test

An Instron Tensile Tester with a four-point bend fixture was used for assembly testing, the support and load span were 160mm and 76mm, respectively (Figures 3 and 4) . The test is done to determine the inflection strain which represent mechanical failure (pad cratering) for variation in filler which is used to reduce the z-axis expansion, and is predominantly used in multi-layer PCBs in high reliability applications, glass style or resin percentage which determine how thicker the PCBs, thinner glass results in higher resin content and allows easier drill for PTHs and Vias, and finally the lamination process which play a large role in PCB quality and reliability.

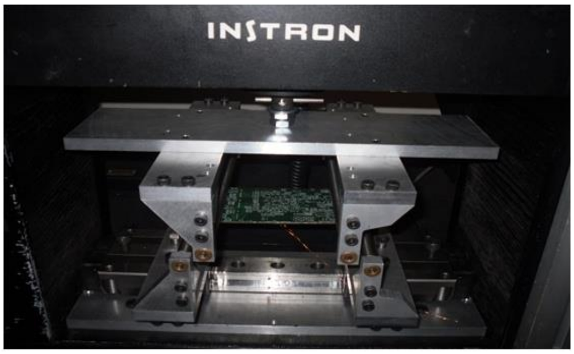

Figure 3.Instron

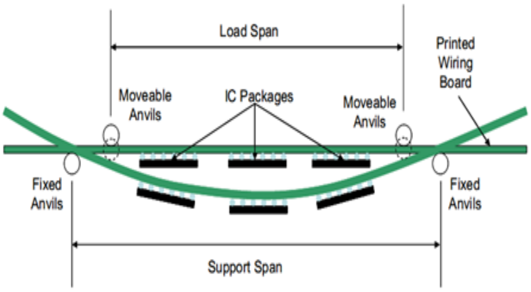

Figure 4. 4-point bending test

A target strain rate of 6000 µ-strain/second was chosen as it is a relatively high rate and is more likely to produce cracks under the pads than a lower rate.

3. Result and Discussion

Performing the test at the joint level yields faster results at cheaper cost; it can offer quantitative data on individual pads. Testing was done on the IT laminates with different design variables using the HBP test method at 30° to the substrate normal. Ten pads were tested under the test methodology for each laminate. Full factorial design has been conducted on the strength with three factors each factor with two levels and ten replicates. From the ANOVA in Table2 at 95% confidence level, it can be seen that the most significant factor is the process then the resin% and the filler is not significant, but the interaction between the filler and the process is the most significant among the main factors and their interaction as normal plot shows the thesameresults as shown in Figure 5.

Table 2. ANOVA

Source	DF	Adj SS	Adj MS	F-Value	P-Value
Model	4	1.570	0.392	25.48	0.00
Resin %	1	0.428	0.143	9.27	0.00
Filler	1	0.068	0.068	4.40	0.04
Process	1	0.271	0.271	17.56	0.00
Filler * Process	1	1.148	1.148	47.11	0.00
Error	35	0.539	0.015		
Total	39	2.109			
R-Square = 74.43%			R-Sqaure (adj) = 71.51%		

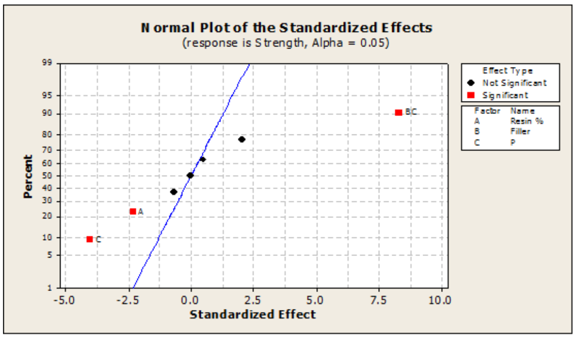

Figure 5…

Figure6 exhibits a comparison between different percentage of resin (53% Versus 74%), then a two sample t-test was conducted, the p-value (P-Value = 0.131) shows that the differences between the strengths obtained from 53% and 74% of resin is not statistically significant, but the trend shows that for 53% of resin is stronger and this is attributed to the thicker fiber glass in the laminate of 53% of resin. Another comparison is done between filled and unfilled laminate as shown in Figure 7. A t-test was conducted, the p-value (P-Value = 0.1390) shows that the differences between the strength from filled and unfilled laminate is not statistically significant, also the trend shows that for filled laminate is stronger than unfilled laminate. The presence of filler particles in laminate materials influences the pad performance. Inert filler particles inhibit the crack propagation resulting in higher fatigue resistance for filled materials as shown by Li (J., 2007) and Roggeman*et al.* (Brian, 2008). Both of them agree with the fact that though the differences in strengths of two materials that were tested are not statistically significant but the fatigue resistances are higher for the filled material.

The last comparison is done between standard and advance process in which the p-value that was resulted from t-test is P-Value = 0.243). From Figure8, it is obvious that the laminate that was manufactured by standard process is stronger than advance process. It can be seen from Figures 8, 9 and 10 that there is an increasing trend in the strength with the design variables of 53% of resin, filled laminate and standard process. However, from the two sample t-test, the p-value shows that the differences between the strength from filled versus unfilled, 53% versus 74% of resin and standard versus advanced process is not statistically significant.

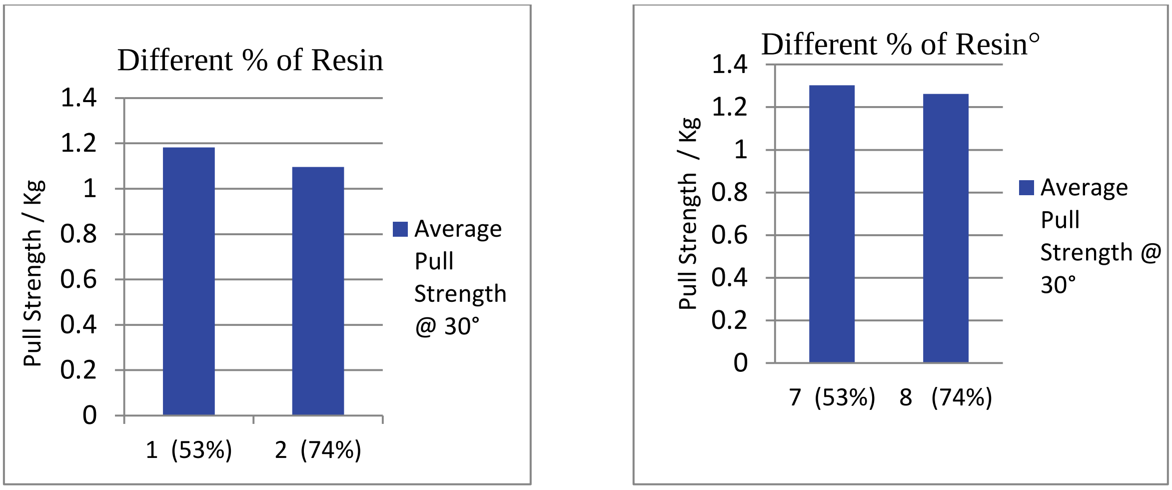

Figure 6. Comparison between different percentage of resin (for 1&2 P-Value = 0.131, for 7& 8 P-Value = 0.555)

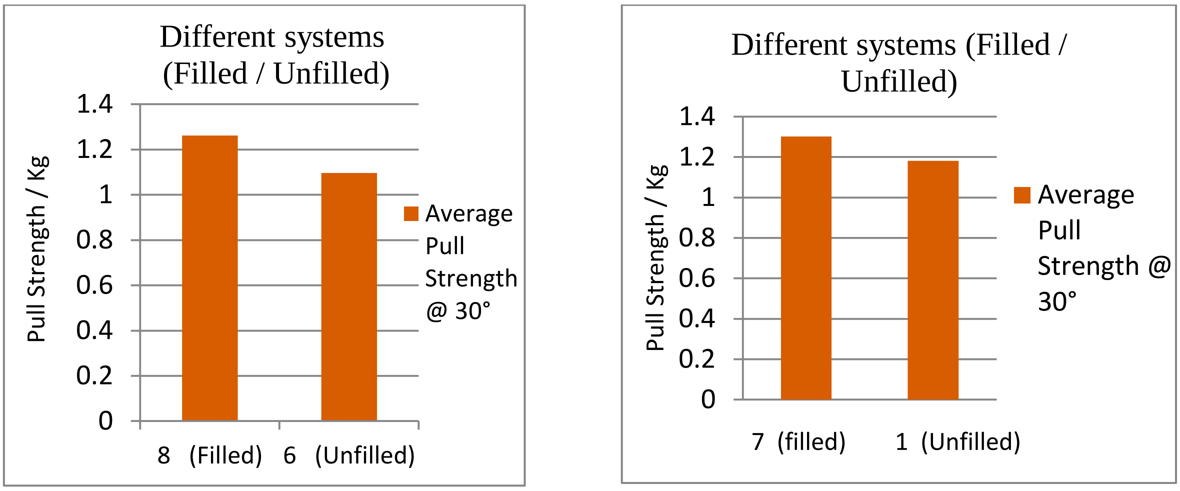

Figure 7. Comparison between different filler (for 7&1 P-Value = 0.139)

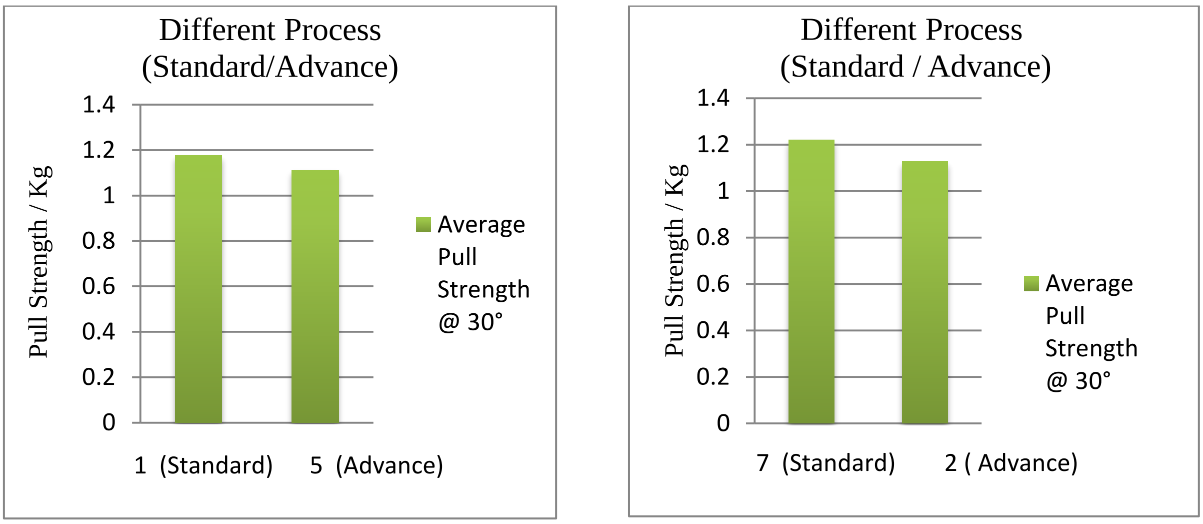

Figure 8. Comparison between different filler (for 1&5 P-Value = 0.243, for 7& 2 P-Value = 0.434)

The failure mode that was observed from the joint level test for the different design variables is a combination of adhesive and cohesive failures, with the cohesive faiure occuring within the resin and the adhesive failure ocurring at the resin-glass interface as it can be seen in Figure 9.

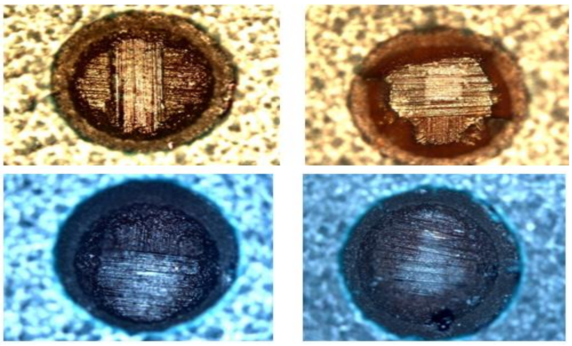

Figure 9. Failur modes top : filled at right ,unfilled at left. Bottom: process at right , advnce at left

Even though joint level testing provides for an easy method for testing, experiments need to be conducted at the assembly level, 4-point beiding test was conducted to creat board flexure using inflection stain approach which measure both PCB and component bending strain at the same time until a point at which the component is separating from the PCB where a mechanical failure will be observed. Figure10 shows the inflection stran mechanism.

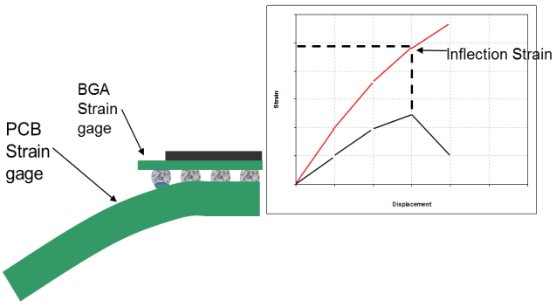

Figure 10.Inflection strain approach

Eight samples were first bent to break. The failed samples were then cross-sectioned and subjected to dye and pry to study the failure mode. The samples showed a good amount of dye penetration under the pads and the cross-sectioned samples showed cracks beneath the interconnecting pad indicating that all failures were by pad cratering. Figure 11 is one of the images that studied.

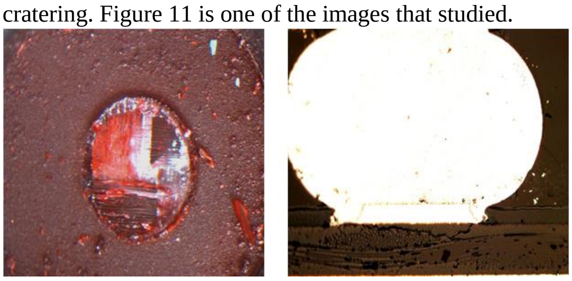

Figure 11.Right dye and pry left cross-sectioned for 1 (Unfilled)

To find the inflection strain which represents a mechanical failure (pad cratering), the data from the Instron and DASwere analyzed. A graph of six curves was drawn; the first two curves (red and blue) indicating the strain for the PCB and the other four curves indicating the strain for the component. A sudden change in the curve with respect to the time would appear as a downward in the graph, the time of occurrence of this gives the strain at which the component separate from PCB and a mechanical failure will occur which is known as pad cratering (Figures 12 and 13).

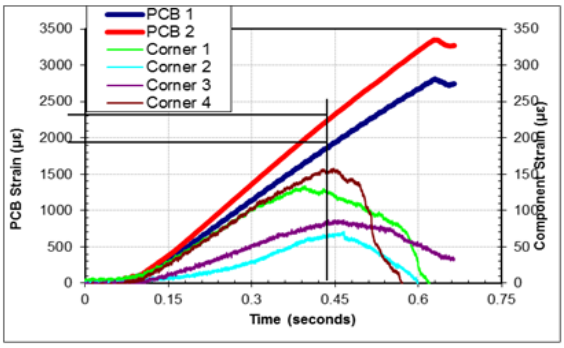

Figure 12.Inflection strain for 1 (unfilled)

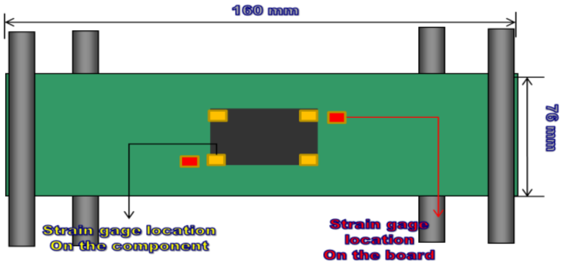

Figure 13.Test setup layout

Figure 14 shows another plot. Please keep in mind that the results for only seven assemblies were available because one of the assemblies had completely not analyzed and this is due to strain gage installation is not done perfectly. The plot shows the inflection strain for each board, it can be seen that for filled laminate and advance process is the strongest one. By comparing laminate 1 and 5 regarding process, it obvious that laminate 1 result in higher inflection strain (strong board) and the differences in the inflection strain is statistically significant at 95% confidence level since p-value=0.007, another comparison is done between laminate7 and 2 regarding the process, laminate 7 result in higher inflection strain but the differences is not statistically significant at the same confidence level since p-value=0.317, it is obvious that the standard process affects the inflection strain but to prove that it requires additional testing. Also a 53% of resin result in higher inflection strain (thicker fiber-glass) than 74% of resin by comparing laminate 7 and laminate 8, the differences between the two laminates is not statically significant since p-value= 0.71. However, by comparing laminate 1 and 6, 74% of resin result in higher inflection strain but the differences is not statistically significant since p-value =0.339. the last comparison is done between laminate 1 and 7 by comparing filled and unfilled laminate, it is clear that laminate 7 result in higher inflection strain, but the differences is not statistically significant since p-value=0.117. However, laminate 6 which is unfilled indicates higher inflection strain by comparing it with laminate 8 which is filled laminate, the differences between the inflection strain is statistically significant since p-value=0.022. So it is obvious that it requires additional testing to determine which design variable affect the inflection strain.

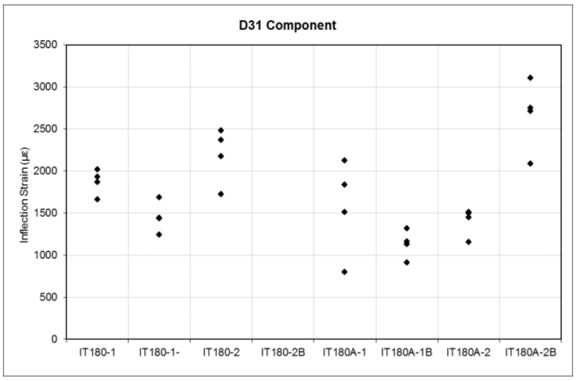

Figure 14.Inflection strain for the samples

4. Summery and Conclusion

Joint level test and assembly level test havebeen investigated here. Several key points of our observations are summarized as follows:

Jointlevel

- The filled resin is consistently stronger than unfilled, not statistically significant at 95% but requires additional testing to prove.
- Lower resin% (thicker glass) results in higher pad strength, not statistically significant at 95% but requires additional testing to prove.
- Standard process result in higher pad Strength, not statistically significant at 95% but requires additional testing to prove.

Assembly level

- Standard process result in higher inflection strain (strong board) but statistically significant at 95% for 1 & 5 but not significant for 7 & 2 requires additional testing to prove.
- Comparing 7 & 8 lower resin% result in higher inflection strain and 2 & 4 higher resin% result in higher inflection strain but requires additional testing to prove.

Failure Mode

- Failure mode for joint level is very similar to assembly level.

References

[1] Ahmad M, D. S. (2008). "Methodology to Characterize Pad Cratering Under BGA Pads in Printed Circuit Boards,". In: Pan Pacific microelectronics symposium, (pp. , Kauai, HI.). Kauai, HI.

[2] Ahmad M., B. J. (2009.). "Validated Test Method to Characterize and Quantify Pad Cratering Under BGA Pads on Printed Circuit Boards". Proc. Of APEX Expo. Las Vegas NY.

[3] Brian., R. (2008). “Pad Cratering, Relating Pad-Level Testing to Board Level Reliability. Binghamton NY : AREA Consortium meeting.

[4] D. Xie, C. C. (May 27-30 2008,). A New Method to Evaluate BGA Pad Cratering in Lead-Free Soldering”. 58th ECTC (pp. pp 893-898). Lake Buena Vista, FL,: 58th ECTC.

[5] Farris A, P. J. (2008). Drop test reliability of lead-free chip scale packages. . In: Electronics components and technology conference; (pp. p. 1173–80). In: Electronics components and technology conference;.

[6] G., G. (2009). Pad Cratering: Characterizing Crack Propagation and the Effects of Humidity and Reflow on Reliability. Binghamton (NY): Master’s thesis. : Binghamton University.

[7] Geng P, M. A. (2005). " 0.8 MM BGA solder joint reliability under flexural load". In: SMTA international conference, (pp. p. 271–8). Rosemont, IL.

[8] Godbole G, R. B. (2009). "On the nature of pad cratering". . In: Electronics components and technology conference (pp. p. 100–8.). Electronics components and technology conference.

[9] J., L. (2007). “Evaluation and Improvement of the Robustness of a PCB Pad in a Lead-Free Environment”. Binghamton City: Master's thesis, Binghamton University, Binghamton NY.

[10] Jonnalagadda K, Q. F. (2005). "Mechanical bend fatigue reliability of lead-free and halogen-free PBGA assemblies". Compon Pack Technol, 2005;28(3), (pp. 430–4.). Compon Pack Technol.

[11] Lee, D. (2006). Printed circuit board consideration for lead free assembly. SMTA International conference (pp. 556-62). Chicago, IL: International Conference.

[12] Long G, E. T. (2007). "Lead free assembly impacts on laminate material properties and pad crater failures". In: Proceedings of APEX February 2007. Los Angeles: APEX .

[13] M. Ahmad, J. B. (2009.). “Comprehensive Methodology to Characterize and Mitigate BGA Pad Cratering in Printed Circuit Boards”. SMTA Journal, Vol.22 Issue 1, 2009. pp.21-28.

[14] M. Mukadam, e. a. (Rosemont, IL, September 26-29, 2005,). Impact of Cracking Beneath Solder Pads in Printed Circuit Boards on the Reliability of BallGrid Array Packages. Proceedings SMTAI 2005, pp. 324-329.

[15]

[16] Mattila TT, M. P. (2006). Reliability of CSP interconnections undermechanical shock loading conditions. IEEE Trans Compon Pack Technol, (pp. 787–95).

[17] Mukadam M, L. G. (2005). “Impact of Cracking Beneath Solder Pads in Printed Circuit Boards on the Reliability of Ball Grid Array Packages”. MTAL, (pp. p. 324-9).

[18] Newman, k. (2008). Board-level solder joint reliability of high performance computers under mechanical loading. In: EuroSimE 2008, international conference on thermal, mechanical and multi-physics simulation and experiments in microelectronics and micro-systems., (pp. p. 1-15). Freiburgim Breisgau 20-23-April 2008.

[19] Parupalli S, N. K. (2008). PCB pad cratering: characterization and techniques. In: ISFTA, November 2–6 2008. Portland, OR: ISFTA.

[20] Raghavan, V. (2010). "Pad Cratering: Development of a test protocol and quantification of the effects of latent damage at the joint level and assembly level". Binghamton NY: Binghamton University.

[21] Roggeman B, R. V. (2011). " Joint level test methods for solder pad cratering investigations" . J Electron Pack , 133(3);031007(8p).

[22] Roggeman, B., Borgesen, P., Li, J., Godbole, G., Tumne, P., Srihari, K. et al. (2008,). “Assessment of PCB pad cratering resistance by joint level testing”,. Proceedings 58th ECTC (pp. pp 884-892). Lake Buena Vista,FL,May 27-30,: ECTC.

[23] Shade FG. (2006). Printed Circuit Board (PCB) pad craters. Santa Clara, CA: Technical report, Intel Corporation.

[24] Vickers N, R. K. (2008). Board level failure analysis of chip scale package drop test assemblies. . In: Proceedings of the 41st international symposium on microelectronics,. Providence, RI, November.

[25] Yang C, S. F. (2010). "Comparative study of PWB pad cratering subject to reflow soldering and thermal impact". In: Electronics components and technology conference, (pp. p. 464–70.).

JJMIE

Volume 10 Number 4, December.2016
ISSN 1995-6665
Pages 279-284

Jordan Journal of Mechanical and Industrial Engineering

Parametric Study for a Reciprocating Screw Blow Injection Molding Process Using Design of Experiments Tools

Khalid Alzoubi *

Yarmouk University, Department of Industrial Engineering,Hijjawi Faculty for Engineering Technology, P.O. Box 566, Irbid 21163, Jordan

Received August, 8, 2016 *Accepted October, 24, 2016*

Abstract

The quality of injection-molded products has been extremely important for customers, because quality is critical to satisfying customers' needs and retaining their loyalty. The factors affecting the quality of parts made by injection molding are numerous. They range from materials used, processes, workers, environment, or a combination of any of these. The injection is a critical operation in the blow injection molding process, therefore, the focus of the present study is to optimize process related factors of the injection operation and understand the effect of some factors and more importantly the interaction between the different factors on the quality of the final product. In the present study, the effect of three core factors was studied. The factors considered were: holding time, holding pressure, and flow. The results showed that the effect of flow and the interaction between flow and holding time were statistically significant and should be carefully considered.

Keywords:...

1. Introduction

Injection molding is the process of forming parts by placing pellets into one side of a cylinder through the Hopper, heating them inside heating chamber and through heating bands located along the screw, and extruding the molten material out to a closed mold in which the material fills and take the shape of a mold cavity as shown in Figure 1.

In the blow injection molding process, the factors affecting the quality of the final product are numerous, which resulted in difficulties in optimizing them. For example, process related variables could be: materials temperature, mold temperature, injection pressure, mold fill rate, clamping force on the mold, shot volume, viscosity of the material, and machine cycle time.

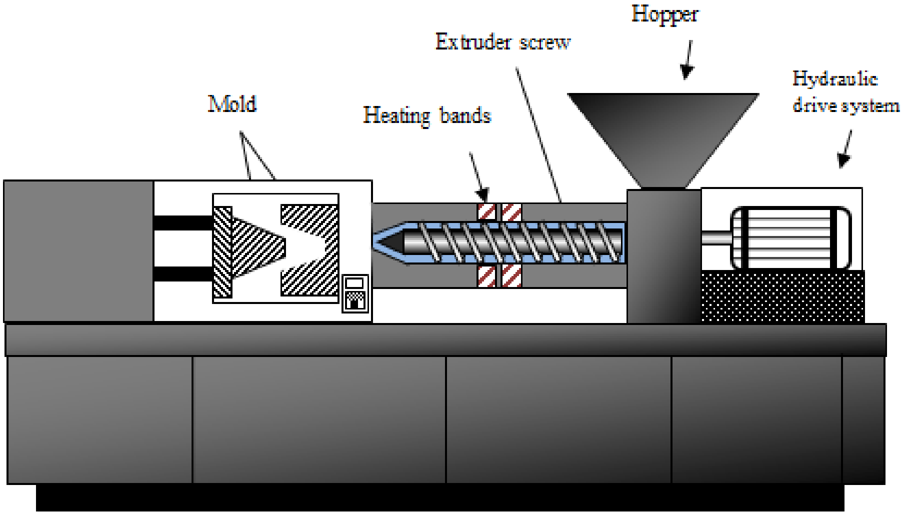

Figure 1. Sketch of the blow injection molding process

Many studies have been done to improve the injection molding process through improvement of materials, improving the process, or even the environmental conditions. For example, Demirel and Daver[1] have

* Corresponding author e-mail: kalzoubi@yu.edu.jo

studied experimentally the perform reheat temperature carried out on a PET bottle produced by a two-stage ISBM machine. Quality of these bottles was measured in terms of top-load strength, burst pressure resistance, Environmental Stress Cracking Resistance (ESCR), and thermal stability. Others have introduced a methodology based on response surface to study the shrinkage and warpage in an injection molded part that has a thin shell element during the injection molding process, Ko-Ta and Fu-Ping[2]. Four factors were considered in their study: mold temperature, packing time, packing pressure, and cooling time. Kramschuster*et al.*[3] have studied the effects of processing conditions on the shrinkage and warpage behavior of a box shaped, polypropylene part using conventional and microcellular injection molding. Six factors were considered in their study: hold time, cooling time, injection speed, hold pressure, max barrel temperature, and chiller temp.

Garbacz and Palutkiewicz[4] have investigated the effect of the type and content of blowing agents in polymeric materials being processed on some physical and mechanical properties of the obtained parts. Salomeia*et al.*[5] have studied the effect of some processing parameters on the quality of the product produced in stretch blow molding process. Záboj, in his work [6], has discussed the effect of melt temperature, injection rate, and holding pressure on the wall thickness of a rectangular plate using polypropylene homopolymer and 40 % talc filled polypropylene material. Tan *et al.*[7] studied the effect of biaxial stretching on the mechanical properties of Polyethylene Terephthalate (PET). They have studied the effect of temperature, strain rates, and stretch ratios on the tensile modulus of the specimens cut from biaxial stretch sheets. Yan and Menary[8] have developed a finite element model to study the sequential stress strain behavior as a function of temperature and strain rate for PET used in stretch blow molding.

Yi-Cheng*et al.*[9] have studied the warpage of plastic fitting, simulation tools were used to study the effect of plastic melting temperature, mold temperature, injection time, packing pressure, packing time, and cooling time on the amount of warpage in the part considered. Artificial neural networks combined with genetic algorithm were used to come up with optimum process parameters that minimize warpage.

Ong *et al.*[10] have proposed a three-dimensional roughness model for filling polymer flow in microinjection molding to study the effect of surface roughness of microcavities on the final quality of the produced part. On the other hand, Zhang *et al.*[11] have also studied the effect of surface roughness on cavity filling in micro injection process for a limited range of injection rate. One the other hand, Menary*et al.*[12] have developed simulation models for the stretch blow molding process based on some experimental studies.

A lot of research has been conducted to evaluate the mechanical properties of either molded parts or the material used. For example, Bociaga and Palutkiewicz[13] have studied certain process parameters (mold temperature and blowing agent percentage) on selected properties of molded parts. The considered properties in their work were weight, mechanical properties, surface state - gloss and color. On the other hand, Manas*et al.*[14] have studied the influence of beta radiation on selected mechanical and thermal properties. Biglione*et al.*[15] have used finite element modeling to study the material behavior in process conditions in a single stage process.

Bordival*et al.*[16] studied the heat transfer problem between the mold and the polymer during the injection molding process. They have developed an experimental method evolution of the thermal contact resistance with time. Amran*et al.*[17] have conducted an optimization study on the size of gate, runner, sprue, in two plate family injection molding process for better quality of molded parts. Al-Refaie*et al.* [18] have used a Data Envelopment Analysis (DEA) method to Measure the Efficiencies of Blowing Machines.

In the present study, the effect of holding time, holding pressure, and flow on the quality of a hollow conical-shaped part was studied. Poypropylene was the material used in the present study; polypropylene has a specific gravity of approximately 0.9. It is capable of withstanding high temperatures. It can be extruded, injection and blow molded[19].

Methodology

For the design of the experiment tools used in the present study, three factors were considered: holding time, holding pressure, and flow. For each of these factors, three levels were considered: low, medium, and high, as shown in Table 1 below.

Table 1. Experiment factors and levels

Level \ Factor	Holding time (sec)	Holding pressure (bar)	Flow (%)
Low	1	30	30
Medium	2	40	40
High	3	50	50

Minitab 17 software was used to build a full factorial design matrix, as shown in Table 2. Twenty seven randomized experimental runs have resulted. Experiments were randomized to minimize biased results which could result if the experiments were conducted in a certain sequence. For each experimental run, three parts were produced and the measurement conducted on each part was averaged. The thicknesses of the resulted parts at specified locations were measured, as shown in Table 2.

Result

A waviness effect could result in the molded parts at locations that are difficult to reach by the molten plastic; an example of such locations is the edges, as shown in Figure 2. Thickness measurements were carefully made at locations of uniform and even surfaces away from the edges of the part

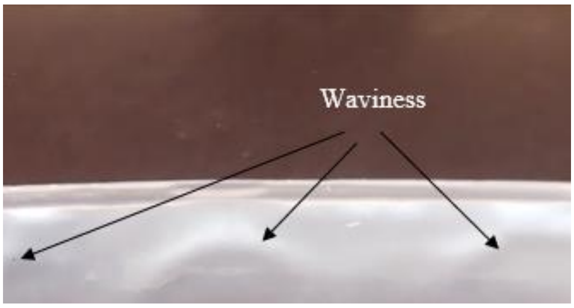

Figure 2. Waviness of plastic

The thicknesses measurements were conducted using dial indicator setup, shown in Figure 3. The setup consisted of a heavy base, connecting rods, and a dial indicator. The resolution of the dial indicator used was 0.01 mm.

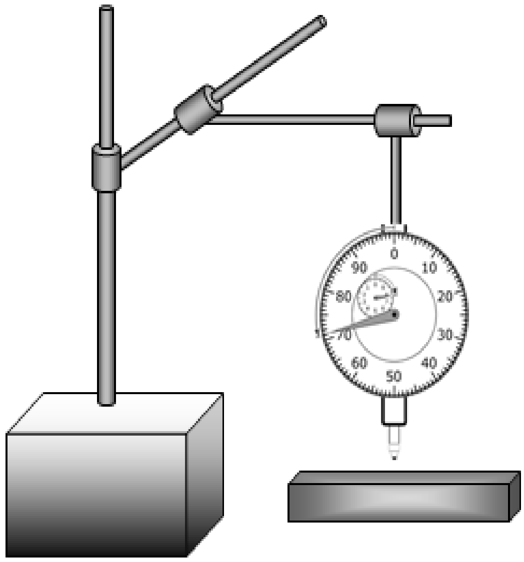

Figure 3. Experimental setup for thickness measurement

Table 2. Full factorial design matrix and thickness measurement

Run #	Time	Pressure (bar)	Flow (%)	Thickness (mm)	Run #	Time (sec)	Pressure (bar)	Flow (%)	Thickness (mm)
1	1	30	50	1.68	15	2	40	50	1.67
2	3	30	40	1.66	16	3	40	30	1.65
3	1	30	30	1.66	17	2	30	40	1.66
4	2	50	50	1.69	18	1	40	40	1.71
5	3	30	50	1.69	19	1	50	40	1.70
6	3	50	40	1.67	20	2	50	30	1.68
7	2	40	40	1.66	21	3	50	30	1.65
8	1	30	40	1.70	22	1	50	50	1.69
9	2	50	40	1.67	23	1	50	30	1.65
10	3	30	30	1.66	24	1	40	50	1.66
11	2	40	30	1.65	25	3	40	40	1.68
12	1	40	30	1.68	26	3	50	50	1.68
13	2	30	50	1.69	27	2	30	30	1.70
14	3	40	50	1.69					

Analysis of variance (ANOVA) [20] is a statistical tool used to detect differences in means (averages) between various levels of a factor. The equations governing the total sum of squares and the sum of squares of the factors and their interactions are listed below:

$$SST = \sum_{i=1}^{a}\sum_{j=1}^{b}\sum_{k=1}^{c}\sum_{l=1}^{n} y_{ijkl}^2 - \frac{y_{....}^2}{abcn}, \quad SS_A = \sum_{i=1}^{a}\frac{y_{i...}^2}{bcn} - \frac{y_{....}^2}{abcn}, \quad SS_B = \sum_{j=1}^{b}\frac{y_{.j..}^2}{acn} - \frac{y_{....}^2}{abcn},$$

$$SS_C = \sum_{k=1}^{c}\frac{y_{..k.}^2}{abn} - \frac{y_{....}^2}{abcn}, \quad SS_{AB} = \sum_{i=1}^{a}\sum_{j=1}^{b}\frac{y_{ij..}^2}{cn} - \frac{y_{....}^2}{abcn} - SS_A - SS_B, SS_{AC} = \sum_{i=1}^{a}\sum_{k=1}^{c}\frac{y_{i.k.}^2}{bn} - \frac{y_{....}^2}{abcn} - SS_A - SS_C, SS_{BC} = \sum_{j=1}^{b}\sum_{k=1}^{c}\frac{y_{.jk.}^2}{an} - \frac{y_{....}^2}{abcn} - SS_B - SS_C$$

It can be noticed that the main effect of flow and the interaction between flow and holding time are significant based on a 95% confidence level with P-values 0.031, and 0.020, respectively, as shown in Table 3. The model has an R-sq value of 85.94%.

A residual plot was constructed as shown in Figure 4; it can be observed from the plot that the ordinary least squares assumptions are being met. For the residual analysis, a normal probability plot for residuals was also constructed, as shown in Figure 5. This plot is used to check if there is any measurement heteroscedasticity, it can be clearly seen that the model assumption of normally distributed errors is satisfied.

Table 3. ANOVA table

Source	DF	Adj SS	Adj MS	F-Value	P-Value
Model	18	0.007111	0.000395	2.72	0.076
Linear	6	0.002311	0.000385	2.65	0.102
Time	2	0.000563	0.000281	1.94	0.206
Pressure	2	0.000141	0.000070	0.48	0.633
Flow	2	0.001607	0.000804	5.53	0.031
2-Way Interactions	12	0.004800	0.000400	2.75	0.079
Time*Pressure	4	0.000904	0.000226	1.55	0.276
Time*Flow	4	0.003170	0.000793	5.45	0.020
Pressure*Flow	4	0.000726	0.000181	1.25	0.365
Error	8	0.001163	0.000145		
Total	26	0.008274			

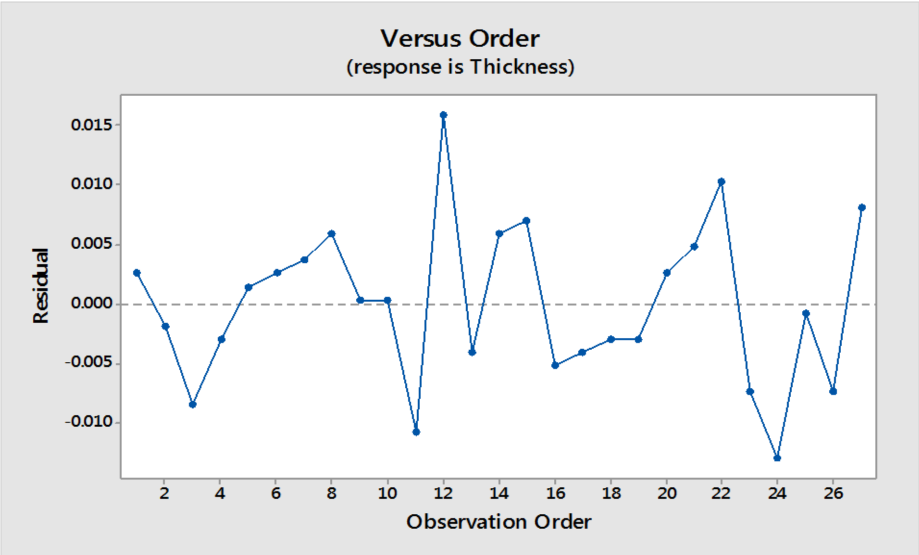

Figure 4. Residual plot

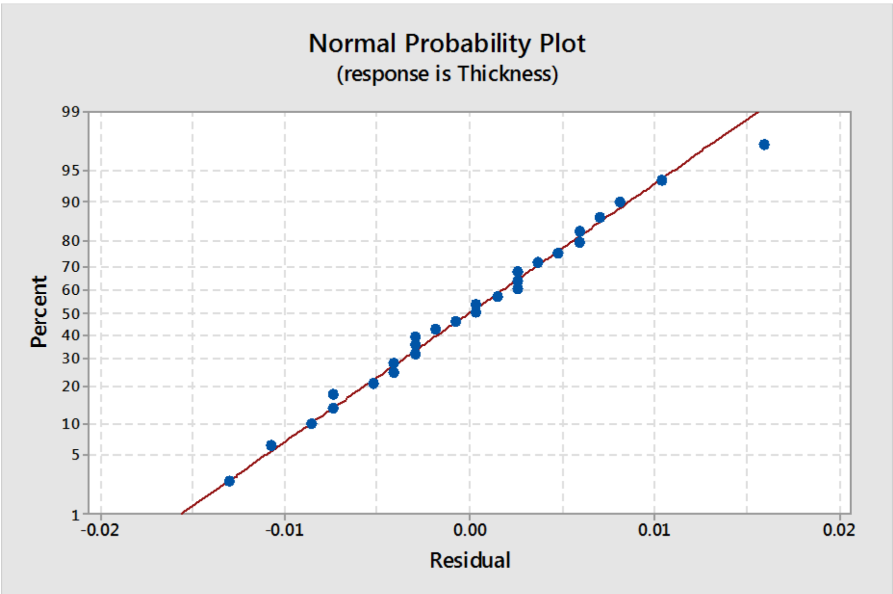

Figure 5. Normal Probability Plot

The ANOVA table shows that the main effect of flow is significant based on a 95% confidence level. Therefore, a main effect plot of the flow factor is shown in Figure 6. It can be clearly seen that the mean of the response is not the same across all factor levels, which means, different levels of the flow factor affect the response differently. It can also be noticed that the steeper the slope of the line, the greater the magnitude of the main effect.

Interaction plots were also constructed to test whether the relationship between one categorical factor and a continuous response depends on the value of the second categorical factor. When two factors interact, that means that changes in the response variable cannot be interpreted by independent effects of the two factors. Rather, the explanation will be more complicated in such a way that the effect of one factor depends on what has happened to the other factor.

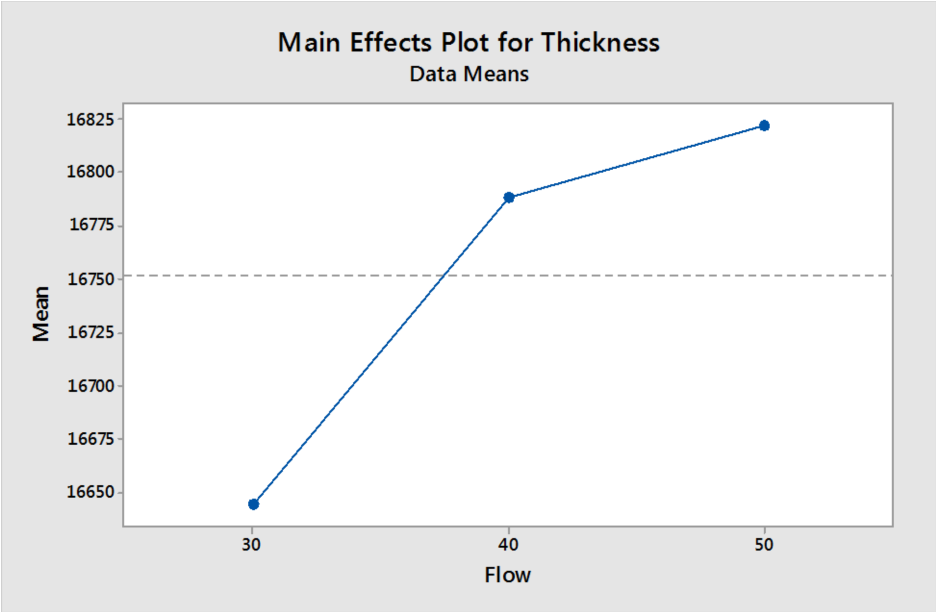

Figure 6. Main effect plot

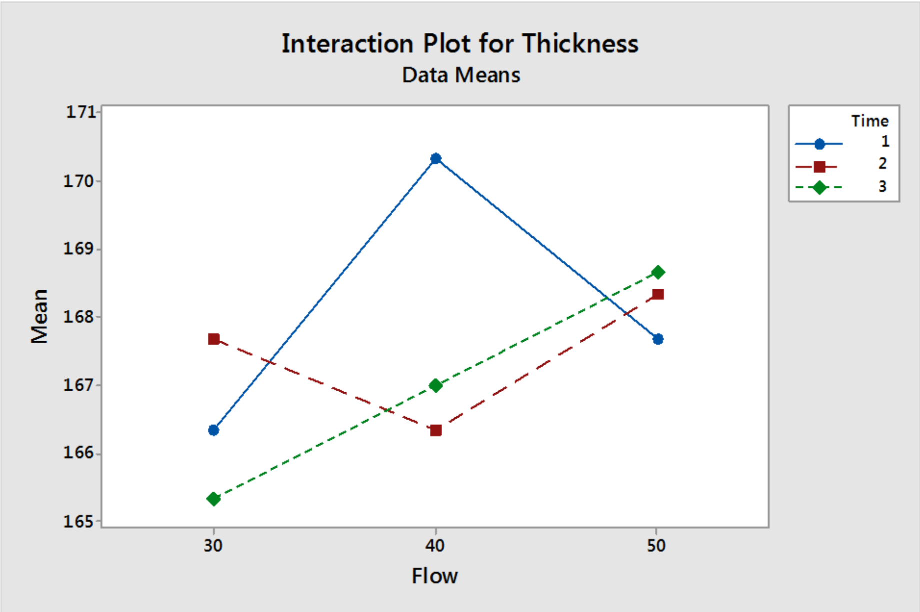

Figure 7. Interaction plot

This interaction effect indicates that the relationship between flow and mean thickness depends on the value of the holding time, as shown in Figure 7. Higher thickness value has resulted when the holding time is 1 second and the flow is 40% compared with the other cases when the holding time is 2 or 3 seconds. This means that the effect of flow is coupled with the state of the holding time.

Conclusion

In the present study, a design of experiment tools was used to study the effect of three factors on the quality of the final hollow conical-shaped parts made using reciprocating screw blow injection molding process. Three factors in the injection process were considered: holding time, holding pressure, and flow. Full factorial design was built and the wall thickness of the resulted part was measured. The ANOVA results have shown that the main effect of flow and the interaction between flow and holding time were significant at a 95% confidence level. For the main effect of flow, the results have shown that greater flows have produced higher thickness means of the molded part. It was also found that the effect of the holding time on the thickness significantly depends on the level of flow. Therefore, they need to be controlled simultaneously during the stages of improvement.

References

[1] B. Demirel and F. Daver, "Experimental study of preform reheat temperature in two- stage injection stretch blow molding" . Polymer Engineering & Science, Vol. 53, 2013, 868-873.

[2] C. Ko-Ta and C. Fu-Ping, "Analysis of shrinkage and warpage in an injection-molded part with a thin shell feature using the response surface methodology". International Journal of Advanced Manufacturing Technology, Vol. 35, 2007, 468-479.

[3] A. Kramschuster, R. Cavitt, D. Ermer, Z. B. Chen, and L. S. Turng, "Effect of processing conditions on shrinkage and warpage and morphology of injection moulded parts using microcellular injection moulding". Plastics, Rubber & Composites, Vol. 35, 2006, 198-209.

[4] T. Garbacz and P. Palutkiewicz, "Effectiveness of blowing agents in the cellular injection molding process". Cellular Polymers, Vol. 34, 2015, 189-214.

[5] Y. Salomeia, G. Menary, and C. G. Armstrong, "Experimental investigation of process conditions in injection stretch blow moulding". AIP Conference Proceedings, Vol. 907, 2007, 896-901.

[6] R. ZÁBoj, "Influence of process conditions on the local shrinkage and on the pressure evolution inside the mold cavity of the injection molded polypropylene in two modifications - PP homopolymer; 40 % Talc Filled PP". Key Engineering Materials, Vol. 669, 2016, 11-18.

[7] C.W. Tan, G.H. Menary, E.M.A. Harkin-Jones, C.G. Armstrong, and P.J. Martin, "Effect of biaxial stretching at temperatures and strain histories comparable to injection stretch blow moulding on tensile modulus for polyethylene terephthalate (PET)". AIP Conference Proceedings, Vol. 907, 2007, 835-840.

[8] S. Y. Yan and G. Menary, "Modeling the constitutive behaviour of PET for stretch blow moulding," AIP Conference Proceedings, Vol. 1353, 2011, 838-843.

[9] C. Yi-Cheng, W. Shu-Lung, and W. Yueh-Hua, "Ram injection molding mold flow analysis and process parameter optimization". International Journal of Organizational Innovation, Vol. 7, 2015. 165-183.

[10] N.S. Ong, H.L. Zhang, and Y.C. Lam, "Three-dimensional modeling of roughness effects on microthickness filling in injection mold cavity". International Journal of Advanced Manufacturing Technology, Vol. 45, 2009, 481-489.

[11] H.L. Zhang, N.S. Ong, and Y.C. Lam, "Mold surface roughness effects on cavity filling of polymer melt in micro injection molding". International Journal of Advanced Manufacturing Technology, Vol. 37, 2008, 1105-1112.

[12] G.H. Menary, C.W. Tan, M. Picard, N. Billon, C.G. Armstrong, and E.M.A. Harkin-Jones, "Numerical simulation of injection stretch blow moulding: comparison with experimental free blow trials". AIP Conference Proceedings, Vol. 907, 2007, 939-944.

[13] E. Bociaga and P. Palutkiewicz, "The impact of mould temperature and blowing agent content on structure and properties of injection moulded parts". Cellular Polymers, Vol. 32, 2013, 257-277.

[14] D. Manas, M. Manas, M. Ovsik, M. Stanek, P. Stoklasek, T. Fiala, "Evaluation of mechanical properties of surface layer injection molded polypropylene by nanoindentation test". Key Engineering Materials, Vol. 699, 2016, 86-90.

[15] J. Biglione, Y. Bereaux, J.-Y. Charmeau, R. G. Rinaldi, J. Balcaen, and S. Chhay, "Injection blow moulding single stage process - approach of the material behaviour in process conditions and Numerical Simulation," Key Engineering Materials, Vols. 651-653, 2015, pp. 805-811.

[16] M. Bordival, F.M. Schmidt, Y. Le Maoult, and E. Coment, "Measurement Of thermal contact resistance between the mold and the polymer for the stretch-blow molding process". AIP Conference Proceedings, Vol. 907, 2007, 1245-1250.

[17] M.A. Amran, M. Hadzley, S. Amri, R. Izamshah, A. Hassan, S. Samsi, "Optimization of gate, runner and sprue in two-plate family plastic injection mould". AIP Conference Proceedings, Vol. 1217, 2010, 309.

[18] Abbas Al-Refaie, Ruba Najdawib , Erin Syc, " Using DEA window analysis to measure the efficiencies of blowing machines in plastics industry". Jordan Journal of Mechanical and Industrial Engineering, Vol. 10, No. 1, 2016, 27-38.

[19] Niebel BW, Draper AB, and Wysk RA. Modern manufacturing process engineering. Mcgraw-Hill College; 1989.

[20] Montgomery DC, Applied statistics and probability for engineers. 6th Edition, John Wiley & Sons; 2013.

JJMIE

Volume 10 Number 4, December. 2016
ISSN 1995-6665
Pages 285 -297

Jordan Journal of Mechanical and Industrial Engineering

Radiative Boundary Layer Flow and Heat Transfer of Nanofluid over a Nonlinear Stretching Sheet with Slip Conditions and Suction

T. Vijaya Laxmi [a, b, *], Bandari Shankar [a]

[a] Department of Mathematics, Osmania University, Hyderabad-500007, Telangana, India.

[b] Department of Mathematics, M.V.S. Govt. Arts & Science College, Mahabubnagar-509001, Telangana, India

Received Jan, 30 2016 Accepted April, 23, 2016

Abstract

The magneto hydrodynamics (MHD) boundary layer flow and heat transfer of a nanofluid with boundary slip condition for velocity second order, thermal slip, solutal slip, and suction, thermal radiation have been investigated numerically over a nonlinear stretching sheet with viscous dissipation. The profiles for the velocity, temperature and nanoparticle concentration depends on parameters viz. thermal radiation parameter R, suction parameter s, velocity first and second order slip parameters A and B, respectively, thermal slip parameter C, concentration slip parameter D, power-law parameter N, Prandtl number Pr, Lewis number Le, Brownian motion parameter Nb, thermophoresis parameter Nt, Eckert number Ec, and magnetic parameter M. Similarity transformation is used to convert the governing non-linear boundary-layer equations into coupled higher order non-linear ordinary differential equations. These equations are numerically solved by using an implicit finite difference method known as Keller-Box method. An analysis has been carried out to reveal the effects of governing parameters corresponding to various physical conditions. Numerical results and Graphical representation are obtained for distributions of velocity, temperature and concentration, as well as, for the skin friction, local Nusselt number and local Sherwood number for several values of governing parameters. The result reveals that velocity decreases with increase of first and second order velocity slip, suction and increases with increase of power-law parameter. Temperature decreases with the increase of thermal slip, suction, concentration slip but increases with thermal radiation, second order velocity slip. Nanoprticle concentration decreases with increase of concentration slip, suction, thermal radiation, thermal slip but increase with increase of second order velocity slip. A comparison with previous results available in the literature has been done and we found a good conformity with it. The numerical values of skin friction, Nusselt number and Sherwood number are presented in tables.

Keywords: Thermal radiation, nanofluid, non-linear stretching sheet, slip conditions, suction, MHD.

1. Introduction

Boundary layer flow over a stretching surface with velocity slip, temperature-jump and solutal slip boundary conditions is an important type of flow and heat transfer occurring in several engineering applications. In these types of transport phenomena, the equations corresponding to continuum equations of momentum and energy are still governed by the Navier-Stokes equations, but the effects of the walls are taken into account by using appropriate boundary conditions. No-slip condition is inadequate for most non-Newtonian liquids, as some polymer melt often shows microscopic wall slip and that has a controlling influence by a nonlinear and monotone relation between the slip velocity and the traction. It is known that, a viscous fluid normally sticks to boundary and there is no slip of the fluid relative to the boundary. However, in some situations there may be a partial slip between the fluid and the boundary. For such fluid, the motion is still governed by the Navier Stokes equations, but the usual no-slip condition at the boundary is replaced by the slip condition. Partial velocity slip may occur on the stretching boundary when the fluid is particulate, such as emulsions, suspensions, foams and polymer solutions. In various industrial processes, slip effects can arise at the boundary of the pipes, walls, curved surfaces etc. A boundary layer slip flow problem arises in polishing of artificial heart valves and internal cavities. Recently many authors obtained analytical and numerical solutions for boundary layer flow and heat transfer due to a stretching sheet with slip boundary conditions.

Some of the authors have considered second order slip boundary conditions to study the flow, heat and mass transfer by employing boundary layer approximations and seeking similarity solutions [1-5]. Khader [6] obtained

* Corresponding author. e-mail: vijaya9966998024@rediffmail.com, bandarishankar@gmail.co.in.

numerical solution by Laguerre collocation method to study the effect of viscous dissipation on the steady flow with heat transfer of Newtonian fluid towards a permeable stretching surface embedded in a porous medium with second order slip effect. Abdul Hakeem *et al.* [7] performed both numerical and analytical solution to study the effect of magnetic field on a steady two dimensional laminar radiative flow of an incompressible viscous water based nanofluid over a stretching/shrinking sheet with second order slip boundary condition. Very recently, Mabood and Mastroberardinob [8] considered the second order slip boundary conditions to investigate the effects of viscous dissipation and melting on MHD boundary layer flow of an incompressible, electrically conducting water-based nanofluid over a stretching sheet. Hayat *et al.* [9] studied a steady three-dimensional boundary layer flow of water based nanofluid with copper as nanoparticle over a permeable stretching surface with second order velocity slip and homogeneous–heterogeneous reactions. Zhu *et al.* [10] investigated the effects of the second-order velocity slip and temperature jump boundary conditions on the magnetohydrodynamic (MHD) flow and heat transfer of water-based nanofluids containing Cu and Al_2O_3 in the presence of thermal radiation. Megahed [11] obtained numerical solution to study the boundary layer flow and heat transfer for an electrically conducting Casson fluid over a permeable stretching surface with second-order slip velocity model and thermal slip conditions in the presence of internal heat generation/absorption and thermal radiation.

Heat transfer, influenced by thermal radiation has applications in many technological processes, including nuclear power plants, gas turbines and various propulsion devices for aircraft, missiles, satellites and space vehicles. Various engineering processes, involve high temperature and essential to the study of radiation heat transfer in designing and manufacturing of equipments. Suspension of nano-solid particles in classical fluids has a known method for the improvement of thermal conductivity of heat transfer fluids. 'Nanofluid', introduced by Choi *et al.* [12], gives the fluid contains of nano-sized particles (diameter of 1 to 100 nm) that are suspended in a base fluid, like water, ethylene glycol, propylene glycol, etc. Addition of high thermally conductive metallic nanoparticles, like silver, copper, aluminium, silicon, improves thermal conductivity of such mixtures, thereby enhancing the overall energy transport capability. It has been found that nanofluids have a potential to increase the thermal conductivity as well as convective heat transfer performance of the base fluid. One of the possible mechanisms for anomalous increase in the thermal conductivity of nanofluids is the Brownian motion of the nanoparticles within the base fluids. This attractive characteristic of nanofluids creates an impressive for wide application [13], [14]. Nanofluids became the next-generation heat transfer fluids and their superior heat transfer features are better than that of any other ordinary fluids. Khan and Pop [15] studied the phenomenon of nanofluid over a stretching sheet for laminar boundary layer flow. The nanofluid flow over an exponentially stretching sheet was introduced by Nadeem and Lee [16]. The laminar boundary layer flow of a nanofluid over a nonlinear stretching sheet is extended by Rana and Bhargava [17]. Rahman and Eltayeb [18] extend the radiative heat transfer in a hydromagnetic nanofluid over a nonlinear stretching surface. Cortell *et al.* [19] explained the boundary layer flow and heat transfer of fluid under the consideration of thermal radiation and viscous dissipation over a nonlinear stretched sheet. The boundary layer flow over a permeable moving flat plate under the effect of viscous dissipation and thermal radiation by considering of few nanofluids is studied by Motsumi and Makinde [20]. Heat transfer over nonlinear stretching and shrinking sheets under the influence of magnetic field, thermal radiation and viscous dissipation by considering copper, alumina, and titanium oxide nanoparticles was examined by Pal *et al.* [21]. Later, Nandy and Pop [22] extended the study of MHD boundary layer stagnation flow and heat transfer over a shrinking sheet incorporating the two component model under the effect of radiation. Rashidi *et al.* [23] have also investigated the combined effect of magnetic field and thermal radiation over a vertical stretching sheet for two dimensional water based nanofluid flow. Mustafa *et al.* Studied [24] the boundary layer flow of a nanofluid over an exponentially stretching sheet to the case of a permeable shrinking sheet with the second order velocity slip in the presence of zero normal flux of the nanoparticles at the boundary. Several authors have studied the flow and heat transfer of a viscous (regular) fluid over an exponentially stretching surface ([25]; [26]; [27]; and [28]).

Based on the observations from the above cited work, the purpose of the present paper is to analyze the effect of second order velocity slip, temperature slip and solutal slip in the presence of thermal radiation with suction of a steady two-dimensional flow of a nanofluid over a nonlinear stretching sheet. Governing nonlinear ordinary differential equations obtained after the application of similarity transformations are solved numerically by means of Keller-Box method. The effects of different flow parameters on flow fields are elucidated through graphs and tables.

2. Flow Analysis and Mathetatical Formulation

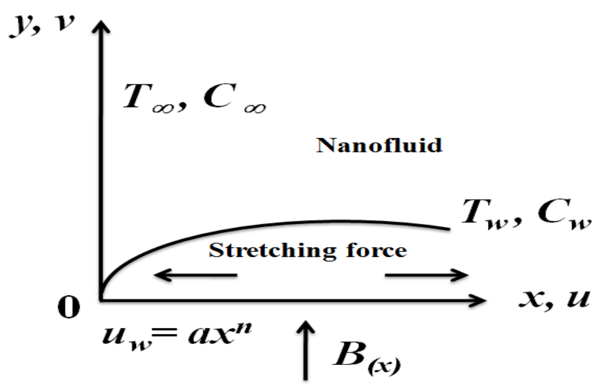

Figure 1. Flow organization with coordinate system

Consider a two dimensional, steady and incompressible viscous flow of a nanofluid past over a nonlinear stretching surface. The sheet is extended with velocity

$u_w(x) = ax^n$ with fixed origin location, where "n" is a nonlinear stretching parameter, ''a'' is a dimensional constant known as stretching rate and x is the coordinate measured along the stretching surface. The nanofluid flows at y = 0, where y is the coordinate normal to the surface. The fluid is electrically conducted due to an applied magnetic field B(x) normal to the stretching sheet. The magnetic Reynolds number is assumed small and so, the induced magnetic field can be considered to be negligible. The wall temperature T_w and the nanoparticle fraction C_w are assumed constant at the stretching surface. When y tends to infinity, the ambient values of temperature and nanoparticle fraction are denoted by $T\infty$ and $C\infty$, respectively. The constant temperature and nanoparticle fraction of the stretching surface T_w and C_w are assumed to be greater than the ambient temperature and nanoparticle fraction T_∞ ,C_∞, respectively. T is the temperature and C is the rescaled nanoparticle volume fraction in the boundary layer. The coordinate system and the flow model are shown in Figure 1. The governing equations of continuity, momentum, thermal energy and nanoparticles equations can be written as:

$$\frac{\partial u}{\partial x} + \frac{\partial v}{\partial y} = 0 \quad (1)$$

$$u\frac{\partial u}{\partial x} + v\frac{\partial u}{\partial y} = \upsilon\frac{\partial^2 u}{\partial y^2} - \frac{\sigma B^2(x)}{\rho_f}u \quad (2)$$

$$u\frac{\partial T}{\partial x} + v\frac{\partial T}{\partial y} = \alpha\frac{\partial^2 T}{\partial y^2} + \tau\left\{D_B\frac{\partial C}{\partial y}\frac{\partial T}{\partial y} + \frac{D_T}{T_\infty}\left(\frac{\partial T}{\partial y}\right)^2\right\} + \frac{\upsilon}{c_p}\left(\frac{\partial u}{\partial y}\right)^2 - \frac{1}{(\rho c)_p}\left(\frac{\partial q_r}{\partial y}\right) \quad (3)$$

$$u\frac{\partial C}{\partial x} + v\frac{\partial C}{\partial y} = D_B\frac{\partial^2 C}{\partial y^2} + \left(\frac{D_T}{T_\infty}\right)\frac{\partial^2 T}{\partial y^2} \quad (4)$$

The boundary conditions for the velocity, temperature and nanoparticle fraction are defined as:

$$u(x) = u_w + u_{slip},\quad v = v_w(x),\quad T = T_w + T_{slip},\ C = C_w + C_{slip}\quad at\quad y = 0 \quad (5)$$

$$u = 0,\quad v = 0,\quad T = T_\infty,\ C = C_\infty\quad at\quad y = \infty \quad (6)$$

Here, u and v are the velocity components along the x and y-axes, respectively.

$\alpha = \frac{k}{(\rho c)_f}$ is the thermal diffusivity, σ is electrical conductivity, ν is the kinematic viscosity, ρ_f is the density of the base fluid, D_B is the Brownian diffusion coefficient and D_T is the thermophoresis diffusion coefficient. $\tau = \frac{(\rho c)_p}{(\rho c)_f}$ is the ratio between the effective heat capacity of the nanoparticle material and heat capacity of the fluid, c is the volumetric volume coefficient, ρ_p is the density of the particles, and C is rescaled nanoparticle volume fraction. We assume that the variable magnetic field B(x) is of the form $B(x) = B_0 x^{\frac{(n-1)}{2}}$. U_{slip} is the slip velocity at the surface and it is negative due to stretching. Wu's [29] slip velocity model used in this paper and is valid for arbitrary Knudsen numbers and is given as follows:

$$T_{slip} = k_1\frac{\partial T}{\partial y} \qquad C_{slip} = k_2\frac{\partial C}{\partial y}$$

where k_n is the Knudsen number, l = min (1/K_n, 1), σ is the momentum accommodation coefficient with 0 ≤ σ ≤ 1 and γ is the molecular mean free path. Based on the definition of l, it is seen that for any given value of K_n, we have 0 ≤ l ≤ l. Since the molecular mean free path γ is always positive it results that B is a negative number. A′, B′ are first and second order velocity slip factors, respectively, k1 is the thermal slip factor, k2 is the concentration slip factor.

Using the Rosseland [30] approximation as in Cortell [19], the radiative heat flux is simplified as:

$$q_r = -\frac{4\sigma^*}{3k^*}\frac{\partial T^4}{\partial y} \ldots\ldots\ldots\ldots\ldots\ldots (7)$$

We assume that the temperature differences within the flow region, namely, the term T^4 can be expressed as a linear function of temperature. The best linear approximation of T^4 is obtained by expanding it in a Taylor series about $T\infty$ and neglecting higher order terms. That is:

$$T^4 \cong 4T_\infty^3 T - 3T_\infty^4 \ldots\ldots\ldots\ldots\ldots\ldots (8)$$

Using equation (8) into equation (7) the modified equation of (3) is:

$$q_r = \frac{-4\sigma^*}{3k^*}\frac{\partial}{\partial y}\left(4T_\infty{}^3 - 3T_\infty{}^4\right) = \frac{-16\sigma^* T_\infty{}^3}{3k^*}\frac{\partial T}{\partial y}$$
$$and\quad \frac{\partial q_r}{\partial y} = \frac{-16\sigma^* T_\infty^3}{3k^*}\frac{\partial^2 T}{\partial y^2} \quad (9)$$

$$u\frac{\partial T}{\partial x} + v\frac{\partial T}{\partial y} = \alpha\left(1 + \frac{4}{3}R\right)\frac{\partial^2 T}{\partial y^2} + \tau\left\{D_B\frac{\partial C}{\partial y}\frac{\partial T}{\partial y} + \frac{D_T}{T_\infty}\left(\frac{\partial T}{\partial y}\right)^2\right\} + \frac{\upsilon}{c_p}\left(\frac{\partial u}{\partial y}\right)^2 \quad (10)$$

Using the following transformations:

$$\eta = y\sqrt{\frac{a(n+1)}{2\upsilon}}x^{\frac{(n-1)}{2}},\quad u = ax^n f'(\eta),$$
$$v = -\sqrt{\frac{a\upsilon(n+1)}{2}}x^{\frac{(n-1)}{2}}\left(f(\eta) + \frac{n-1}{n+1}\eta f'(\eta)\right) \quad (11)$$
$$G(\eta) = \frac{(T - T_\infty)}{(T_w - T_\infty)},\quad H(\eta) = \frac{(C - C_\infty)}{(C_w - C_\infty)}$$

where ψ represent the stream function and is defined as:

$$u = \frac{\partial \psi}{\partial y} \quad and \quad v = -\frac{\partial \psi}{\partial x}$$

so that Eq.(1) is satisfied identically.

The governing equations (2), (10) and (4) are reduced by using equation (11) as follows:

$$f''' + ff'' - Nf'^2 - Mf' = 0 \tag{12}$$

$$\left(1 + \frac{4}{3}R\right)G'' + \Pr fG' + \Pr NbG'H' + \Pr NtG'^2 + \Pr Ecf''^2 = 0 \tag{13}$$

$$H'' + LefH' + \frac{Nt}{Nb}G'' = 0 \tag{14}$$

The transformed boundary conditions are:

$$\begin{aligned} &f'(0) = 1 + Af''(0) + Bf'''(0), \\ &f(0) = s,\ G(0) = 1 + EG'(0), \\ &H(0) = 1 + DH'(0) \\ &f'(\infty) = 0,\ G(\infty) = 0,\ H(\infty) = 0 \end{aligned} \tag{15}$$

where the prime denote differentiation with respect to η. The involved physical parameters are defined as follows:

$$\begin{aligned} &N = \frac{2n}{n+1},\ \Pr = \frac{\upsilon}{\alpha},\ R = \frac{4\sigma^* T_\infty^3}{k^* \alpha (\rho C)_p}, \\ &Nb = \frac{\tau D_B (C_w - C_\infty)}{\upsilon},\ Nt = \frac{\tau D_T (T_w - T_\infty)}{T_\infty \upsilon}, \\ &Ec = \frac{u_w^2}{C_p (T_w - T_\infty)} \qquad M = \frac{2\sigma B_0^2}{a\rho_f (n+1)}, \\ &Le = \frac{\upsilon}{D_B},\quad s = \frac{-v_w}{x^{\frac{n-1}{2}} \sqrt{\frac{a\upsilon (n+1)}{2}}}, \\ &A = A' \sqrt{\frac{a(n+1)}{2}} x^{\frac{n-1}{2}} = \frac{2}{3}\left(\frac{3-\alpha l^3}{\alpha} - \frac{3}{2}\frac{1-\alpha^2}{k_n}\right)\gamma \sqrt{\frac{a(n+1)}{2}} x^{\frac{n-1}{2}}, \\ &B = B' \frac{a(n+1)}{2} x^{n-1} = -\frac{1}{4}\left(l^4 + \frac{2}{k_n^2}(1-l^2)\right)\gamma^2 \frac{a(n+1)}{2} x^{n-1}, \\ &E = k_1 \sqrt{\frac{a(n+1)}{2}} x^{\frac{n-1}{2}},\quad D = k_2 \sqrt{\frac{a(n+1)}{2}} x^{\frac{n-1}{2}} \end{aligned} \tag{16}$$

Here N is the Power-law parameter, Pr is the Prandtl number, R is Thermal radiation, Nb is Brownian motion parameter, Nt is Thermophoresis parameter, Ec is Eckert number, M is Magnetic parameter, Le is Lewis number, s is mass transfer parameter, i.e., suction for ($v_w < 0$), injection for ($v_w > 0$), A is First order velocity slip parameter, B is second order velocity slip parameter, E is Thermal slip parameter, D is Concentration slip parameter.

Now equations (12) to (14) together with the boundary conditions (15) to have similarity solutions, the quantities A, B, E and D must be constant and not a function of 'x' as in equation (16). This condition can be realized if the mean free path of the nanoparticles γ is proportional to:

$$\gamma = cx^{\frac{-(n-1)}{2}}$$

We therefore assume:

$$\begin{aligned} &\gamma = cx^{\frac{-(n-1)}{2}},\ also\ assume\ thermal\ slip\ factor\quad k_1 = e_1 x^{\frac{-(n-1)}{2}}, \\ &concentration\ slip\ factor\ k_2 = e_2 x^{\frac{-(n-1)}{2}} \end{aligned} \tag{17}$$

C, k1, k2 are proportionality constants. With the introduction of (17) into equation (16) of velocity, thermal, concentration slip parameters, we have:

$$\begin{aligned} &A = \frac{2}{3}\left(\frac{3-\alpha l^3}{\alpha} - \frac{3}{2}\frac{1-l^2}{k_n}\right)\sqrt{\frac{a(n+1)}{2}}c > 0, \\ &B = \frac{-1}{8}\left(l^4 + \frac{2}{k_n^2}(1-l^2)\right)a(n+1)c^2 < 0 \\ &E = \sqrt{\frac{a(n+1)}{2}}e_1 > 0,\quad D = \sqrt{\frac{a(n+1)}{2}}e_2 > 0 \end{aligned} \tag{18}$$

With A, B, E and D defined by equation (18), the solutions of equations (12) to (14) yield the similarity solutions. However, with A, B, E and D defined by relations (17), the solutions generated are the local similarity solutions. The quantities of practical interest, in the present study, are the local skin friction Cf_x, Nusselt number Nux and the Sherwood number Shx which are defined as:

$$C_f = \frac{\tau_w}{\rho u_w^2},\quad Nu_x = \frac{xq_w}{k(T_w - T_\infty)},\quad Sh_x = \frac{xq_m}{D_B(C_w - C_\infty)} \tag{19}$$

where τ_w is shear stress at wall, q_w is the heat flux and q_m is the mass flux at the surface which are given below:

$$\tau_w = \mu\left(\frac{\partial u}{\partial y}\right)_{y=0},\quad q_w = -\left(k + \frac{16\sigma^* T_\infty^3}{3k^*}\right)\left(\frac{\partial T}{\partial y}\right)_{y=0},\quad q_m = -D_B\left(\frac{\partial C}{\partial y}\right)_{y=0} \tag{20}$$

Substituting equation (10) into equations (19), (20), we obtain:

$$\begin{aligned} &C_f \mathrm{Re}^{\frac{1}{2}} = f''(0),\ Nu_x \mathrm{Re}^{\frac{-1}{2}} = -\left(1 + \frac{4}{3}R\right)G'(0),\ Sh_x \mathrm{Re}^{\frac{-1}{2}} = -H'(0) \\ &where\ \mathrm{Re} = \frac{a(n+1)}{2\upsilon}x^{n+1}\quad Local\ \mathrm{Re}ynods\ number \end{aligned} \tag{21}$$

3. Numerical Methods

The ordinary differential equations (12), (13), (14) with the boundary conditions of equation (15) are solved numerically by using of Keller-Box method, as revealed by [31], the following few steps are involved to achieve Numerical solutions:

- Reduce the above mentioned higher order ordinary differential equations into a system of first order ordinary differential equations;
- Write the finite differences for the first order equations;
- Linearize the algebraic equations by Newton's method, and write them in matrix–vector form; and
- Solve the linear system by the block tri-diagonal elimination technique.

- To get the accuracy of this method the appropriate initial guesses have been chosen. The following initial guesses are chosen:

$$f_0(\eta)=s+\frac{1}{1+A-B}\left(1-e^{x}\right),\; G_0(\eta)=\left(\frac{1}{1+E}\right)e^{-x},\; H_0(\eta)=\left(\frac{1}{1+D}\right)e^{-x}$$

The choices of the above initial guesses depend on the convergence criteria and the transformed boundary conditions of equation (15). The step size 0.01 is used to obtain the numerical solution with four decimal place accuracy as the criterion of convergence.

4. Results and Discussion

The magneto hydrodynamics (MHD) boundary layer flow [32] and heat transfer [33] of a nanofluid with velocity second order slip, temperature jump, solutal boundary slip condition, suction and thermal radiation has been investigated numerically over a nonlinear stretching sheet with viscous dissipation. The numerical solutions are obtained for velocity, temperature and concentration profiles for different values of governing parameters. The obtained results are displayed through Figures 2 to 20 for velocity, temperature and concentration profiles, respectively. In the simulation the default values of the parameters are considered as M=1, Nb=Nt=0.5, Le=5, Pr=6.8, s=0.5, Ec=0.2, A=1, B=-1, E=1, D=1, R=0.1, N=1.5, unless otherwise specified.

5. Velocity Profiles

The velocity profile f ′(0) for different values of the magnetic field parameter M, mass suction parameter s, power-law parameter N and velocity first and second order slip parameter A, B are shown in Figures 2 to 6, respectively.

Figure 2 reveals the influences of magnetic field on the flow field. The presence of transverse magnetic field, the fluid induces Lorentz force, which opposes the flow. This resistive force tends to slow down the flow, which results in the decreasing of velocity field. As The values of magnetic parameter M increase, the retarding force increases and consequently the velocity decreases. The graph also reveals that the boundary layer thickness reduces as magnetic parameter M increases.

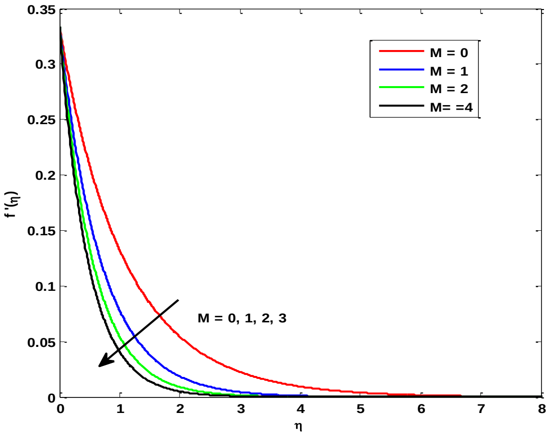

Figure 2. Velocity graph for different values of magnetic parameter M

The effect of suction/injection parameter ‘s’ on the velocity profile for a nonlinear stretching surface is presented in Figure 3 in presence of surface slip. It is observed from the figure that velocity distribution across the boundary layer decreases with an increase in suction parameter s. Thus, the suction reduces the thickness of hydrodynamic boundary layer; the effect is reverse in the case of injection.

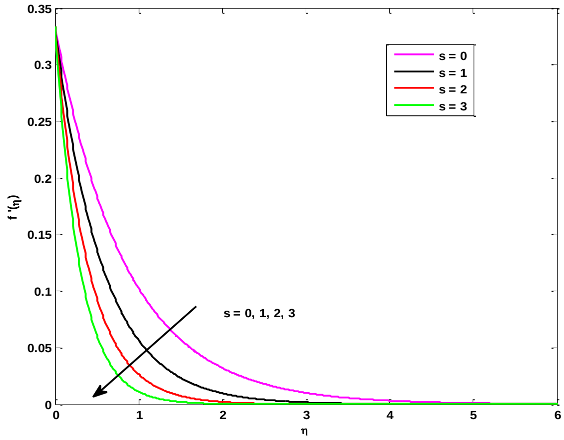

Figure 3. Velocity graph for different values of Suction parameter s.

On observing from Figure 4, as the power-law parameter increases, the velocity profile decreases. Figure 5 illustrates the variation of the dimensionless velocity component f ′(η) for various values of the first order slip parameter A. From the figure, it is clear that the velocity of the fluid near the boundary layer region decreases by increasing slip parameter. If the slip parameter increases, the slip at the surface wall is also increases. As a result it reaches to a smaller amount of diffusion due to the stretching surface into the fluid. In the case of no slip condition, the value of A approaches to zero so the velocity slip at the wall is equal to zero, i.e., u_s = 0, consequently the fluid velocity adjacent to the wall is equal to the velocity of the stretching surface u_w, then f ′ (0) = 1. Figure 6 shows that the dimensionless velocity component f ′ (η) decreases with the decreasing values of second order velocity slip parameter B.

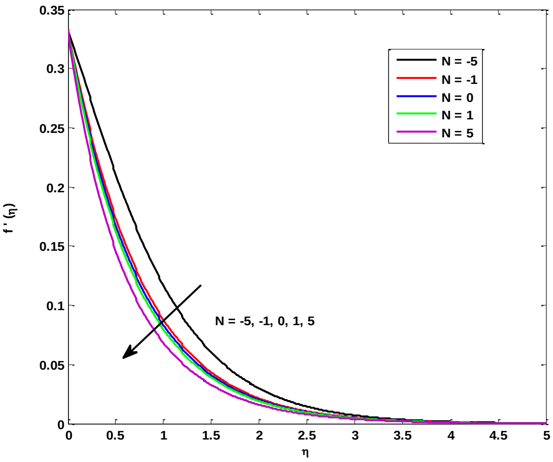

Figure 4. Velocity graph for different values of Power-law parameter N

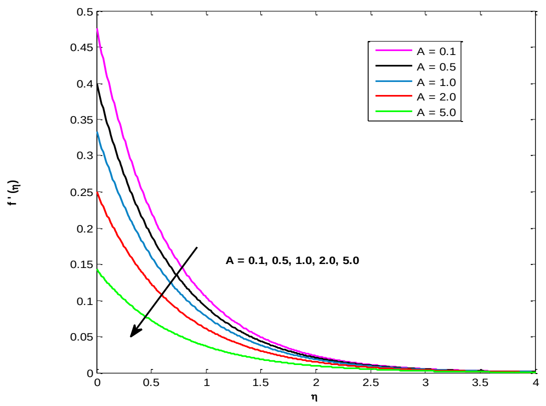

Figure 5. Velocity graph for different values of first order velocity slip parameter A

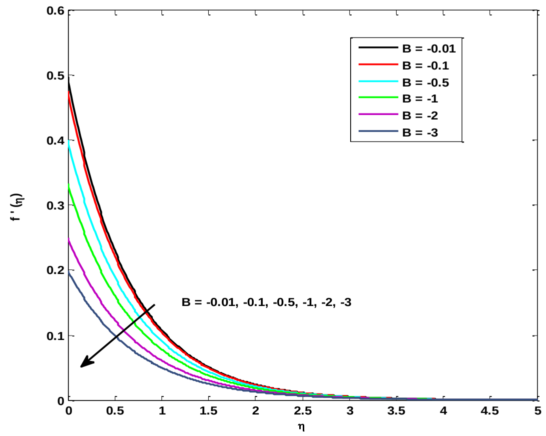

Figure 6. Velocity graph for different values of second order velocity slip parameter

6. Temperature Profiles

Figures 7 to 14 present the variation of temperature with respect to the governing parameters, viz. Prandtl number Pr, thermal slip parameter E, radiation parameter R, Eckert number Ec, suction parameter s, thermophoresis parameter Nt, Brownian motion parameter Nb and magnetic parameter M, respectively.

The effect of Prandtl number Pr on the heat transfer process is shown by the Figure 7. The Prandtl number is a material property, it varies from fluid to fluid. The Figure 7 reveals that as an increase in Prandtl number Pr, the temperature field decreases. An increase in the values of Pr reduces the thermal diffusivity, because Prandtl number is a dimensionless number which is defined as the ratio of momentum diffusivity to thermal diffusivity, that is Pr = υ/α . Increasing the values of Pr implies that momentum diffusivity is higher than thermal diffusivity. Therefore thermal boundary layer thickness is a decreasing function of Pr. In general the Prandtl number is used in heat transfer problems to reduce the relative thickening of the momentum and the thermal boundary layers.

The influence of thermal slip on the temperature profiles is shown in Figure 8 which describes that the fluid temperature decreases on increasing thermal slip parameter E in the boundary layer region and, as a consequence, thickness of the thermal boundary layer decreases.

Figure 9 demonstrates the variation of temperature with respect to radiation parameter *R*. When the Rosseland radiative absorptivity k^* decreases, the divergence of the radiative heat flux $\partial qr\ /\ \partial y$ increases, which leads to increases the rate of radiative heat transfer to the fluid at the surface, i.e., it provides more heat to the fluid which causes the fluid temperature to increase. Hence, the temperature profile as well as thermal boundary layer thickness increases as the value of thermal radiation increases.

Figure 10 illustrates the power of Eckert number Ec on temperature in the boundary layer. On observing the temperature graph, the wall temperature of the sheet increases as the values of Ec increase. As the irreversible process by means of which the work done by a fluid on adjacent layers due to the action of shear forces is transformed into heat influenced by viscous dissipation. It is also noticed that the reversal flow happened because of the temperature enhancement occurs as heat energy is stored in the fluid due to frictional heating. Also, due to the fact that, decrease of rate of heat transfer at the surface, the thermal boundary layer thickness increases, when the values of Ec increases.

In Figure 11 the influence of the suction/injection parameter ‘s’ on the temperature profiles is depicted. It can, easily, be seen from the figure that the temperature distribution across the boundary layer decreases with increasing the values of s > 0 in the presence of thermal slip and hence the thickness of the thermal boundary layer decreases whereas opposite effect occurs for s < 0.

Figures 12 and 13 show the influence of the change of Brownian motion parameter Nb and thermophoresis parameter Nt on temperature profile. It is noticed that as thermophoesis parameter and Brownian motion parameter Increases the temperature increases in the boundary layer. As the thermophoretic effect increases, nanoparticles are migrated from the hot surface to cold ambient fluid, as a result the temperature will enhances in the boundary layer. This will help in the thickening of the thermal boundary layer. Figure 14 shows the influence of magnetic field parameter M on the thermal field. Transverse magnetic field has increased the thermal boundary layer thickness, so it causes the temperature increment in the boundary layer when it increases.

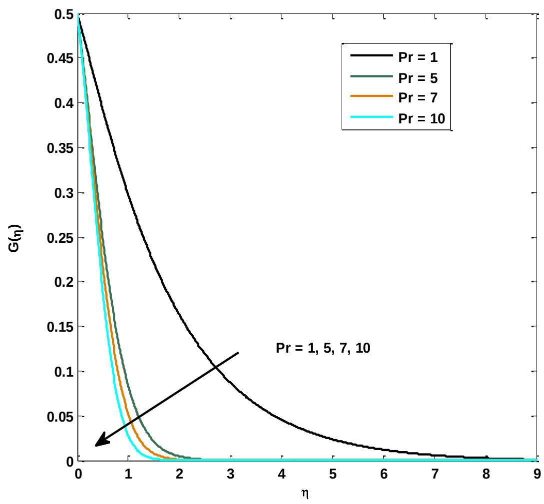

Figure 7. Temperature graph for different values Prandtl number Pr

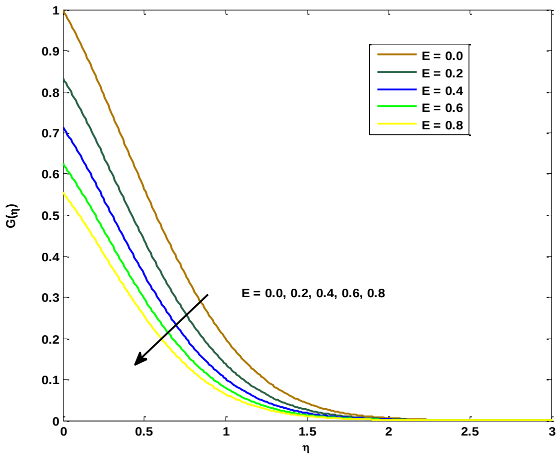

Figure 8. Temperature graph for different values Thermal slip parameter E

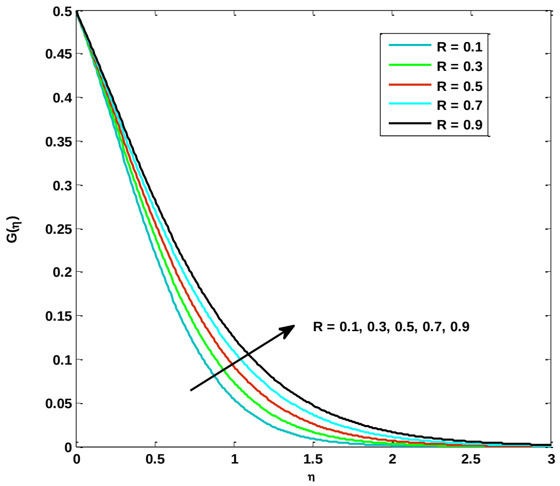

Figure 9. Temperature graph for different values Thermal radiation R

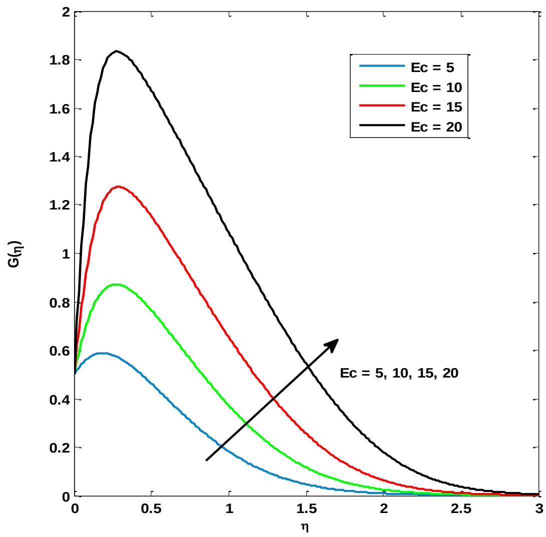

Figure 10. Temperature graph for different values Eckert number Ec

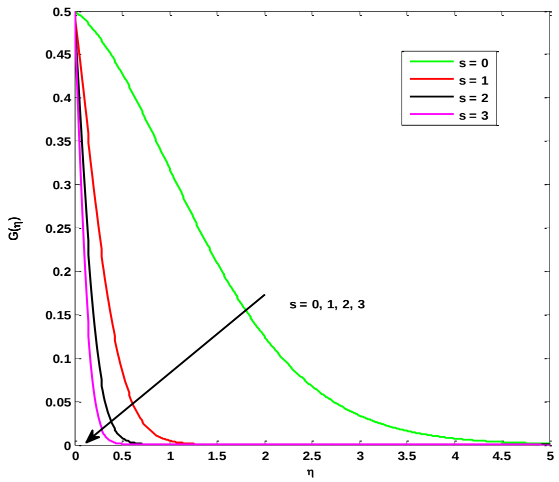

Figure 11. Temperature graph for different values suction parameter s

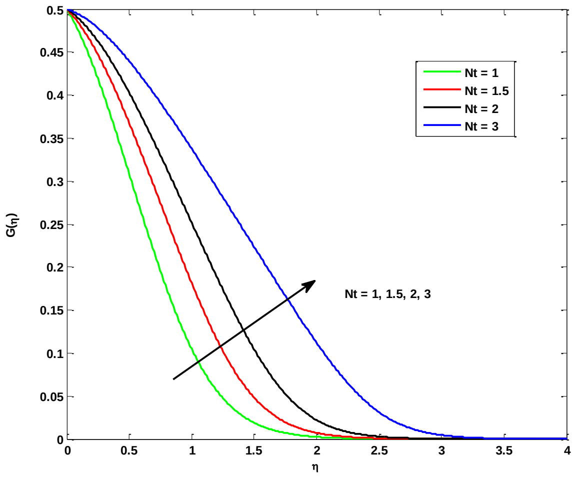

Figure 12. Temperature graph for different values thermophoresis parameter Nt

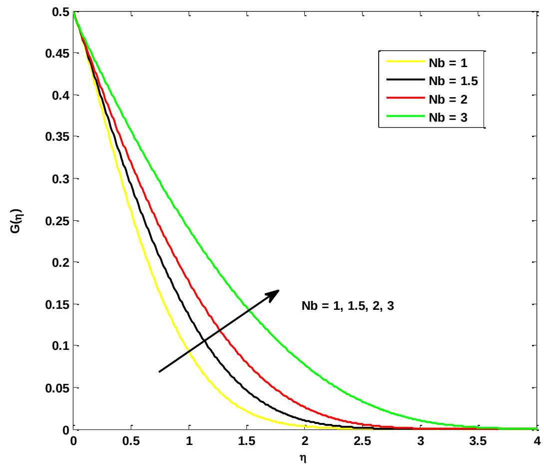

Figure 13. Temperature graph for different values Brownian motion parameter Nb

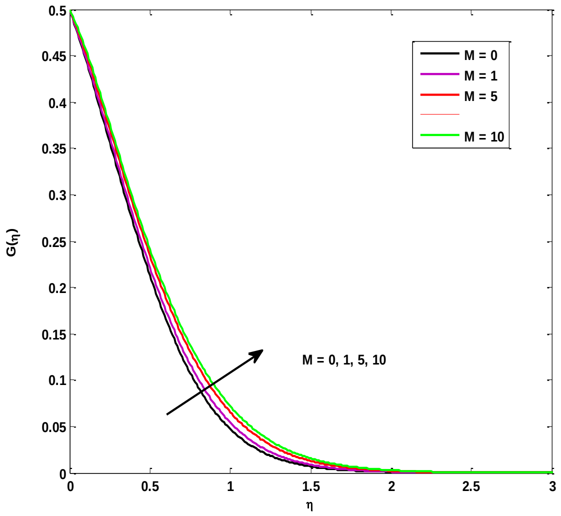

Figure 14. Temperature graph for different values magnetic parameter M

7. Nanoparticle Concentration Profiles

Figures 15 to 20 demonstrate the variation of nanoparticle concentration with respect to the change in governing parameters, viz. Lewis number Le, Brownian motion parameter Nb, thermophoresis parameter Nt, concentration slip parameter D, suction s and radiation parameter R.

Figure 15 shows the impact of Lewis number Le on concentration profile. Actually, a higher value of Lewis number Le $=\alpha/D_B$ represents a lower nanoparticle diffusivity (Brownian motion) and a higher thermal diffusivity. If Le > 1 the thermal diffusion rate exceeds the Brownian diffusion rate. Lower Brownian diffusion leads to less mass transfer rate, as a result, the nanoparticle volume fraction (concentration) graph and the concentration boundary layer thickness decreases. Figure16 reveals the variation of concentration profile. As the larger thermophoresis parameter Nt values gives the larger temperature gradient. The concentration field is motivated by the temperature gradient. As the temperature is an increasing function of Nt, an increase in Nt parameter increases the concentration and its boundary layer thickness. The nanoparticle concentration and concentration boundary layer thickness will increases as increase in Nt. We can see from the Figure 17 that the concentration profile is decreasing function of Nb. This may be due to the fact that as Brownian motion parameter decreases the mass transfer of a nanofluid.

From Figure 18 we can observe the variation of concentration with respect to solutal slip parameter D. As it can be seen from the graph, increasing in the concentration slip parameter D, the concentration profile is decreasing. The suction parameter ‘s’ has a strong influence on the concentration profile as it is shown in Figure 19. As the values of suction parameter s increase, concentration graph decreases and the concentration boundary layer thickness decreases. Figure 20 reflects the variation of radiation on concentration graph. The influences of radiation parameter on concentration is not this much significant. As the values of radiation parameter R increase, the concentration boundary layer thickness is not changing much, almost it is constant.

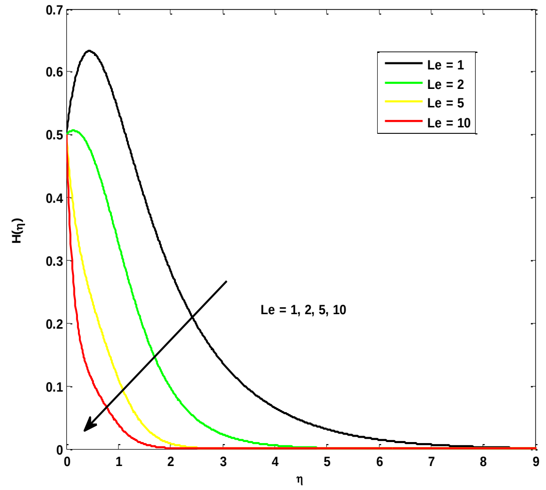

Figure 15. Temperature graph for different values Lewis number Le

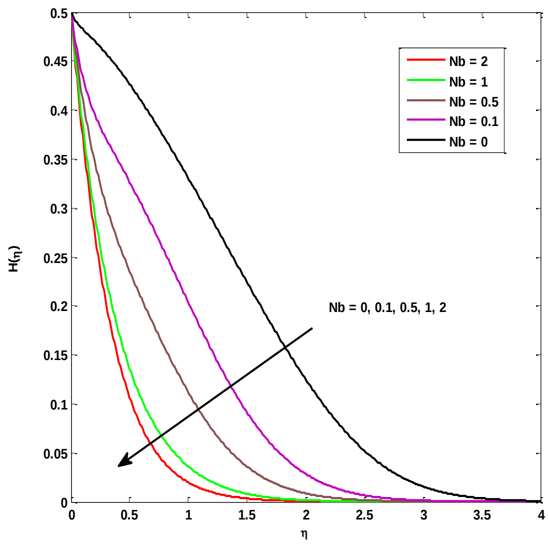

Figure 16. Temperature graph for different values Brownian motion parameter Nb

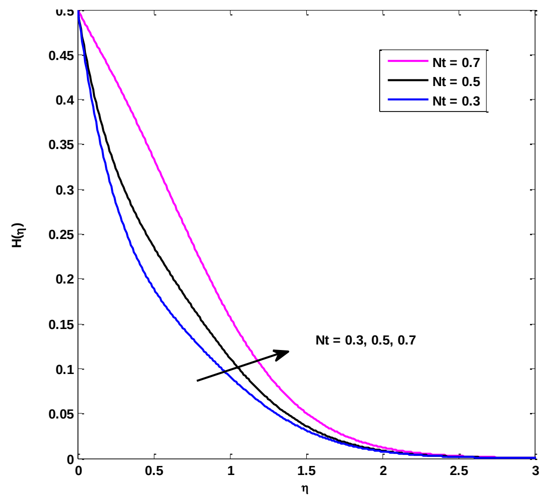

Figure 17. Temperature graph for different values thermophoresis parameter Nt

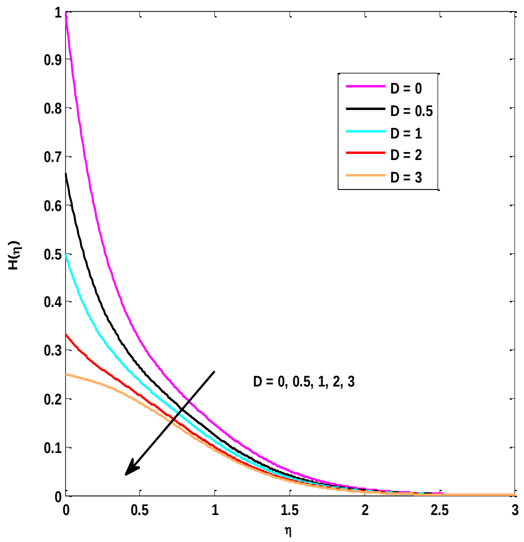

Figure 18. Temperature graph for different values concentration slip parameter D

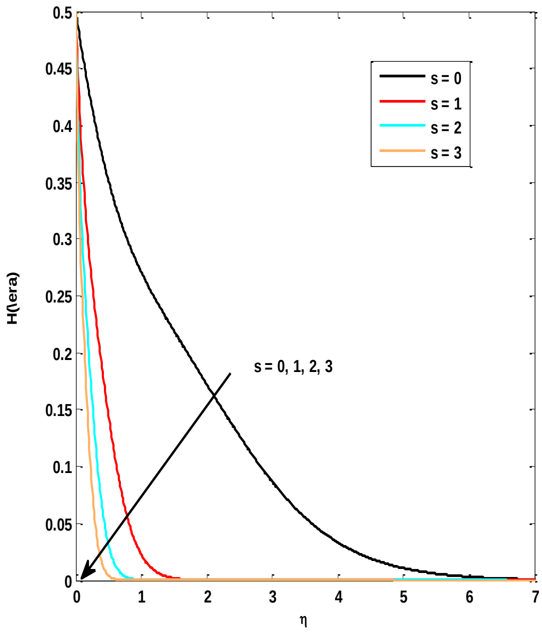

Figure 19. Temperature graph for different values suction parameter s

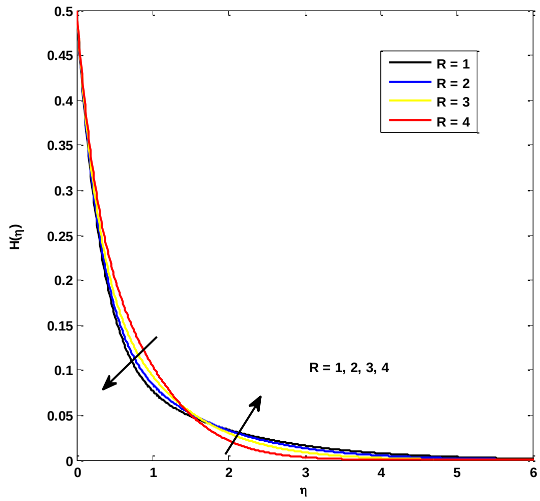

Figure 20. Temperature graph for different values thermal radiation R

Finally, a comparison is done with previous results as it is shown in Table 1, for the numerical values of the skin friction coefficient $-f''(0)$, local Nusselt number $-G'(0)$ and Sherwood number $-H'(0)$ when slip parameters A, B, E, D radiation parameter R and suction parameter s are absent. And it is in excellent agreement with the result published in F. Mabood *et al.* 2015. Table 2 presents the variation of the skin friction coefficient in relation to magnetic field M, suction s, power-law parameter N and velocity first and second order slip parameters A, B. On observing this table, as the values of magnetic field, suction and power-law parameters increase, the values of skin friction coefficient increase. However, the skin friction coefficient decreases as both the values of velocity slip parameters A and B increase. Table 3 shows the local Nusselt number $-G'(0)$ and Sherwood number $-H'(0)$ for different values of Prandtl number Pr, thermal radiation R, Eckert number Ec, thermal slip parameter E and concentration parameter D. It is possible to see that as the values of Prandtl number increase, the heat transfer rate (local Nusselt number) is increased, but when other values as indicated in Table 3 increases, the local Nusselt number decreases. Also we can observe the variation of the mass transfer rate i.e., Sherwood number from this Table. Table 4 represents the variation of both the heat transfer rate $-G'(0)$ and mass transfer rate $-H'(0)$ for different values of the parameters M, s, Nt, Nb and Le when other parameters are fixed.

Table 1. Comparison of Skin friction coefficient, Nusselt and Sherwood numbers when A = B = E = D = R = s = 0

Ec	M	- f ′′ (0) (F.Mabood et al, 2015)	- f ′′ (0) (Present)	- G ′ (0) (F.Mabood et al, 2015)	- G ′ (0) (Present)	- H ′ (0) (F.Mabood et al, 2015)	- H ′ (0) (Present)
0	0	1.10102	1.1010	1.06719	1.0672	1.07719	1.0772
0.1				0.88199	0.8892	1.22345	1.2234
0.2				0.70998	0.7100	1.37078	1.3708
0.3				0.52953	0.5295	1.51919	1.5192
0.5				0.16484	0.1648	1.81933	1.8194
0	0.5	1.3098	1.3099	1.04365	1.0473	1.01090	1.0109
0.1				0.81055	0.8106	1.20605	1.2060
0.2				0.57564	0.5757	1.40279	1.4028
0.3				0.33889	0.3389	1.60115	1.6012
0.5				0.14022	0.1402	2.00282	2.0028
0	1	1.48912	1.4891	1.02337	1.0234	0.95495	0.9549
0.1				0.74058	0.7406	1.19496	1.1950
0.2				0.45543	0.4554	1.43706	1.4371
0.3				0.16789	0.1679	1.68128	1.6813
0.5				0.41451	0.4145	2.17623	2.1763

Table 2. Calculation of skin friction coefficient for various values of M, s, A, B, N.

M	S	A	B	N	-f ′ ′(0)
0	0.5	1	-1	1,5	0.3170
0.5					0.4161
1.0					0.4914
1.5					0.5547
2.0					0.6105
1.0	0				0.4005
	0.2				0.4348
	0.7				0.5325
	1.0				0.5988
	0.5	1			0.4914
		1.2			0.4572
		1.3			0.4418
		1	-1		0.4914
			-2		0.3572
			-3		0.2801
			-1	-0.5	0.4314
				0.5	0.4624
				1.5	0.4914

Table 3. Calculation of Nussult and Sherwood numbers for various values of Pr, R, Ec, E, D.

Pr	R	Ec	E	D	- G ′(0)	- H ′(0)
1	0.1	0.2	1	1	0.2086	1.2676
5					0.4451	1.0703
7					0.4712	1.0505
10					0.4764	1.0508
6.8	0.5				0.4367	1.0771
	0.7				0.4188	1.0918
	1.0				0.3931	1.1131
	0.1	1			0.2470	1.2656
		2			0.0424	1.5440
		3			0.3457	1.8356
		0.2	0		0.6850	0.8984
			1		0.4677	1.0515
			2		0.3411	1.1538
			3		0.2610	1.2195
			1	0	0.1623	-2.7794
				1	0.4697	-1.0515
				2	0.6383	-0.4101
				3	0.7382	0.0740

Table 4. Calculation of Nussult and Sherwood numbers for various values of M, s, Le, Nb, Nt.

M	S	Le	Nb	Nt	-G ′ (0)	-H ′ (0)
0.1	0.5	5	0.5	0.5	0.4927	1.0677
0.2					0.4897	1.0648
0.3					0.4869	1.0623
0.4					0.4842	1.0601
1.0	-0.3				0.0378	0.0639
	-0.2				0.0180	0.1433
	-0.1				-0.0238	0.2541
	0.1				-0.1461	0.5105
	0.2				-0.2205	0.6428
	0.3				-0.3002	0.7771
	0.5	5			0.4697	1.0515
		10			0.3349	2.4995
		15			0.2861	3.8315
		20			0.2610	5.1277
		5	0.1		0.7194	1.3103
			0.2		0.6351	1.2183
			0.3		0.5676	1.1489
			0.4		0.5133	1.0951
			0.5	0.1	2.7662	11.8889
				0.2	1.1371	1.1609
				0.3	0.7582	-0.3290
				0.4	0.5792	-0.8239

8. Conclusions

A numerical study was investigated for the radiative boundary layer flow and heat transfer of nanofluids over a nonlinear stretching sheet with slip conditions, suction with the help of an implicit finite difference method known as Keller-Box method. A parametric study is performed to explore the effects of various governing parameters on the fluid flow and heat transfer characteristic.

The following conclusions give a brief account of the results of the present study:

1. Both first and second order velocity slip parameter A and B reduces the thickness of momentum boundary layer and hence decrease the velocity. N decreases the velocity profile.
2. Velocity profile decrease with increase in suction parameter s, magnetic parameter M.
3. Prandtl number Pr, thermal slip parameter E, suction parameter s reduces the temperature profile.
4. The temperature increases with an increase in radiation parameter R, magnetic parameter M, thermophorosis parameter Nt, Brownian motion parameter Nb, Eckert number Ec.
5. Concentration profile decreases with an increase in Lewis number Le, Brownian motion parameter Nb, concentration slip parameter D, suction s and radiation R but increases with an increase in thermophorosis parameter Nt.

Acknowledgements

The author T. Vijayalaxmi grateful to University Grants Commission (UGC), India for awarding Faculty Development Programme (FDP) and also thankful to CCE, Govt. of Telangana State and Principal, M.V.S. Govt. Arts & Science College, Mahabubnagar, Telangana State.

References

[1] T. Fang, S. Yao, J. Zhang, A. Aziz, "Viscous flow over a shrinking sheet with a second order slip flow model". Comm. Nonlinear Sci. Num. Simul, Vol. 15 (2010), 1831–1842.

[2] T. Fang, A. Aziz, "Viscous flow with second-order slip velocity over a stretching sheet". Natur forsch. A – Phys. Sci. Vol. 65a (2010), 1087–1092.

[3] Mahantesh, M. Nandeppanavar, K. Vajravelu, M. Subhas Abel, M.N. Siddalingappa, "Second order slip flow and heat transfer over a stretching sheet with non-linear Navier boundary condition". Int. J. of Ther. Sci., Vol. 58 (2012), 143-150.

[4] Rosca, C. Natalia, Ioan Pop, "Mixed convection stagnation point flow past a vertical flat plate with a second order slip: Heat flux case". Int. J. of Heat and Mass Transfer, Vol. 65 (2013), 102–109.

[5] Rosca, V. Alin, Ioan Pop, "Flow and heat transfer over a vertical permeable stretching/shrinking sheet with a second order slip". Int. J. of Heat and Mass Transfer, Vol. 60 (2013), 355–364.

[6] M. M. Khader, "Laguerre collocation method for the flow and heat transfer due to a permeable stretching surface embedded in a porous medium with a second order slip and viscous dissipation". Appl. Math and Comp., Vol. 243 (2014), 503–513.

[7] A. K. Abdul Hakeem, N. Vishnu Ganesh, B. Ganga, "Magnetic field effects on second order slip flow of nanofluid over a stretching/shrinking sheet with thermal radiation effect". J. Mag. and Mag. Mat., Vol. 381 (2015), 243–257.

[8] F. Mabood, A. berardino, "Melting heat transfer on MHD convective flow of a nanofluid over a stretching sheet with viscous dissipation and second order slip". J. Taiwan Inst. Chem. Eng. Vol. 374 (2015), 1–7.

[9] T. Hayat, T. Muhammad, A. Alsaedi, M.S. Alhuthali, "Magnetohydrodynamic three-dimensional flow of viscoelastic nanofluid in the presence of nonlinear thermal radiation". J. Mag. and Mag. Mat.,Vol. 385 (2015), 222–229.

[10] J. Zhu, L. Zheng, L. Zheng and X. Zhang, "Second-order slip MHD flow and heat transfer of nanofluids with thermal radiation and chemical reaction". Appl. Math. and Mech., Vol. 36 (2015) No. 9, 1131-1146.

[11] A. M. Megahed, "MHD viscous Casson fluid flow and heat transfer with second-order slip velocity and thermal slip over a permeable stretching sheet in the presence of internal heat generation/absorption and thermal radiation". The Eur.Phy. J. Plus, Vol. 130 (2015), 81.

[12] S. U. S. Choi, "Enhancing thermal conductivity of fluids with nanoparticles". Dev. Appl Non-Newton Flows, Vol. 66 (1995), 99–105.

[13] J. Buongiorno, L. W. Hu, "Nanofluid coolants for advanced nuclear power plants". Proceedings of ICAPP 2005, Seoul, Paper no. 5705 (2005), 15–19.

[14] K. N. Shukla, A, B. Solomon, B.C. Pillai, "Thermal performance of cylindrical heat pipe using nanofluids" J. Ther. Heat Transfer, Vol. 24 (2010), 796–802.

[15] W. A. Khan, I. Pop, "Boundary layer flow of a nanofluid past a stretching sheet". Int. J. Heat Mass Trans, Vol. 53 (2010), 2477–2483.

[16] S. Nadeem, C. Lee, "Boundary layer flow of a nanofluid over an exponentially stretching surface". Nanoscale Res Lett., Vol. 7 (2012), 94.

[17] P. Rana, R. Bhargava, "Flow and heat transfer of a nanofluid over a nonlinear stretching sheet: A numerical study". Commun Nonlin Sci Numer Simul, Vol. 17 (2012), 212–226.

[18] M. M. Rahmann, I.A. Eltayeb, "Radiative heat transfer in a hydromagnetic nanofluid past a nonlinear stretching surface with convective boundary condition". Meccanica, Vol. 48 (2013), 601–615.

[19] R. Cortell, "Effect of viscous dissipation and radiation on the thermal boundary layer over a non-linearly stretching sheet". Phys Lett A, Vol. 372 (2008), 631–636.

[20] T. G. Motsumi, O.D. Makinde, "Effects of thermal radiation and viscous dissipation on boundary layer flow of nanofluids over a permeable moving flat plate". Phys Script, Vol. 86 (2012), 045003.

[21] [21] D. Pal, G. Mandal, K. Vajravelu, "MHD convection–dissipation heat transfer over a non-linear stretching and shrinking sheets in nanofluids with thermal radiation". Int. J. Heat Mass Trans., Vol. 65 (2013), 481–90.

[22] S. K. Nandy, I. Pop, "Effects of magnetic field and thermal radiation on stagnation flow and heat transfer of nanofluid over a shrinking surface". Int. Comm. Heat Mass Trans., Vol. 53 (2014), 50–55.

[23] M. M. Rashidi, N. V. Ganesh, A.K.A. Hakeem, B. Ganga, "Buoyancy effect on MHD flow of nanofluid over a stretching sheet in the presence of thermal radiation". J Mol. Liq., Vol. 198 (2014), 234–238.

[24] M. Mustafa, T. Hayat, S. Obaidat, "Boundary layer flow of a nanofluid over an exponentially stretching sheet with convective boundary conditions". Int. J. Num. Met. Heat Fluid Flow, Vol. 23 (2013), 945–959.

[25] S. Nadeem, T. Hayat, M.Y. Malik, S.A. Rajput, "Thermal radiations effects on the flow by an exponentially stretching surface: a series solution", Natur forsch. Vol. 65A (2010), 1–9.

[26] S. Nadeem, C. Lee, "Boundary layer flow of nanofluid over an exponentially stretching surface". Nanoscale Res. Lett. Vol. 7 (2012), 94-100.

[27] K. Bhattacharyya, "Boundary layer flow and heat transfer over an exponentially shrinking sheet". Chin. Phys. Lett. Vol. 28 (2011), 074701.

[28] K. Bhattacharyya, K. Vajravelu, "Stagnation-point flow and heat transfer over an exponentially shrinking sheet", Comm. Nonlinear Sci. Numer. Simul., Vol. 17 (2012), 2728–2734.

[29] L. Wu, "A slip model for rarefied gas flows at arbitrary Knudsen number". Appl. Phys. Lett., Vol. 93 (2008), 253-103.

[30] Rosseland S, Astrophysik und atom-theoretische Grundlagen, Berlin: Springer; 1931.

[31] Cebeci T, Bradshaw P., Physical and Computational Aspects of Convective Heat Transfer, Berlin: Springer; 1988.

[32] Z. Uddin, M. Kumar, "MHD Heat and Mass Transfer Free Convection Flow near The Lower Stagnation Point of an Isothermal Cylinder Imbedded in Porous Domain with the Presence of Radiation". Jordan Journal of Mechanical and Industrial Engineering, Vol. 5 (2011) No. 2, 133-138.

[33] I. Zahmatkesh, "Heatline Visualization of Buoyancy-Driven Flow inside a Nanofluid-Saturated Porous Enclosure". Jordan Journal of Mechanical and Industrial Engineering, Vol. 9 (2015) No.2, 149-157.

المملكة الأردنية الهاشمية

الجامعة الهاشمية

المجلة الأردنية
للهندسة الميكانيكية والصناعية

JJMIE

مجلة علمية عالمية محكمة

تصدر بدعم من صندوق البحث العلمي

http://jjmie.hu.edu.jo/

ISSN 1995-6665

المجلة الأردنية للهندسة الميكانيكية والصناعية

مجلة علمية عالمية محكمة

المجلة الأردنية للهندسة الميكانيكية والصناعية: مجلة علمية عالمية محكمة تصدر عن الجامعة الهاشمية بالتعاون مع صندوق دعم البحث العلمي في الأردن

ترسل البحوث إلى العنوان التالي

رئيس تحرير المجلة الأردنية للهندسة الميكانيكية و الصناعية

الجامعة الهاشمية

كلية الهندسة

قسم الهندسة الميكانيكية

الزرقاء - الأردن

هاتف : 00962 5 3903333 فرعي 4537

Email: jjmie@hu.edu.jo

Website: www.jjmie.hu.edu.jo